Optical Studies of Ultra-thin WSe_2

Aaron Mitchell Jones

A dissertation
submitted in partial fulfillment of the
requirements for the degree of

Doctor of Philosophy

University of Washington

2015

Reading Committee:

Xiaodong Xu, Chair

David Cobden

Andreas Karch

Program Authorized to Offer Degree:
Physics

University of Washington

Abstract

Optical Studies of Ultra-thin WSe_2

Aaron Mitchell Jones

Chair of the Supervisory Committee:
Assistant Professor Xiaodong Xu
Physics and Materials Science & Engineering

Truly two-dimensional systems allow for examination of quasiparticle physics in the presence of strong Coulomb interactions resulting from reduced dielectric screening and under conditions of energy level quantization due to high carrier confinement. Here, we employ optical techniques to study such a system: ultra-thin WSe_2 crystals. Due to the overpowering oscillator strength of excitonic transitions, our studies explore the unique behavior of neutral and charged excitons which stem from correlations between spin, crystallographic momentum, and layer occupation. The energy and polarization of the incident and detected optical fields provide insight into these correlations, while application of electric fields allows for tuning of excitonic species as well as spin-pseudospin correlations.

Perhaps the most salient result from this work lies in the first demonstration of a superposition state of excitons located in opposite corners of the 1st Brillouin zone. However, other firsts include efficient photon up-conversion in a monolayer semiconductor and spectrally separating intralayer and interlayer excitonic states. Beyond these results, we also find these ultra-thin semiconducting sheets exhibit behaviors such as non-linearity in optically-driven membrane oscillations, electrically tunable excitonic species, and an all-electrical spin Zeeman splitting. Such widespread characteristics and capabilities underscore the importance of continued optoelectronic studies within this class of 2D materials.

TABLE OF CONTENTS

LIST OF FIGURES

GLOSSARY

AOM: Acousto-Optic Modulator

CCD: Charge Coupled Device

CVD: Chemical Vapor Deposition

CW: Continuous Wave

FET: Field-Effect Transistor

FWHM: Full Width at Half Maximum

PL: Photoluminescence

PLE: Photoluminescence Excitation

PVD: Physical Vapor Deposition

Q: Quality Factor

RT: Room Temperature

SHG: Second-Harmonic Generation

TMD: Transition Metal Dichalcogenide

V_G: Gate Voltage

VNA: Vector Network Analyzer

ACKNOWLEDGEMENTS

I must begin by first thanking my advisor, Xiaodong Xu, for fostering the ideal environment for learning and exploration. Beyond his continual availability to answer questions, helpful feedback, and ability to foster problem-solving, he has devoted significant effort and personal time to benefit the personal lives and post-PhD careers of those he works with.

Thank you to Professor David Cobden, for consistently taking a sincere and active interest in this work, and encouraging critical thinking of the problems at hand, while providing much-needed humor. Many thanks to the amazing collaborators who have put so much effort into the work presented here: Wang Yao, Hongyi Yu, and Di Xiao for their adept work on the theoretical underpinnings; Jiaqiang Yan and David Mandrus for creating the excellent crystals we get to study.

This work has had many contributors, and the success of these studies comes in large part from the highly collaborative and symbiotic atmosphere cultured in the lab. I want to thank those whom I was fortunate enough to work with formerly in the lab: Dong Sun, Ricky Roy, Nate Gillgren, Daniel McInally, Sam Totorica, David Feldman, Chunming Huang, Gilbert Arias, Philip Klement, Helin Cao.

Among those currently examining 2D materials in the lab, thanks to Grant Aivazian, who was there from day one. Building up the lab from scratch and battling countless challenges together has certainly been made more bearable with the rock-climbing, humor, and constantly changing facial hair. Thanks to Jason Ross, Sanfeng Wu, Pasqual Rivera, Kyle Seyler, Marie Scott, Genevieve Clark, Ding Zhong, and John Schaibley for taking more than their fair share of sass and sarcasm, and doling it back out. Without them, I never would have had as many opportunities to realign our optical systems.

I also wish to express sincere appreciation for all of the other amazing graduate students,

post-docs, and scientists I've had the pleasure to interact with outside of the lab, who have helped make this PhD such an enjoyable journey.

I must also thank my family. My parents, Alan and Melanie Jones, have never ceased to support me and provide encouragement. Though it wasn't within his line of work, my father has always shared my interest in science. Also, thanks to my grandfather, Bart Czirr, for helping me to recognize early on that physics was my career path, and entertaining questions related to flashlights traveling the speed of light. I would also be remiss if I didn't thank my in-laws, Dave and Karen Phillips, for their continued support.

Finally, thanks to my wife. Attempting to enumerate the heroic efforts and sacrifices she has put forth during this long path would be entirely futile, and while this in no way compensates for them, they are recognized and whole-heartedly appreciated.

DEDICATION

To my amazing wife, Megan, for her never-ending support, encouragement, and hard work; my daughter, Aubrie, for helping me laugh through it all; and my son, Kaden, for letting me finish this before being born.

Chapter 1

INTRODUCTION

The lessons learned as we try to build ever-more sophisticated nanomachines will almost certainly inform our understanding of the origins of life.

– Paul McEuen

This work outlines the novel physics afforded by semiconductors at the truly two-dimensional limit, obtained through the lens of optical spectroscopies of the transition metal dichalcogenide (TMD) WSe_2. Due to a hexagonal crystal structure reminiscent of monolayer graphene, low-energy carriers are indexed by novel quantum indices associated with carrier layer occupation and crystallographic momentum [1–5]. As optical fields of opposite polarization helicity selectively couple to each of these indices, we employ polarization-resolved photoluminescence throughout [6]. Due to the dominance of excitonic transitions in this few atom-thick semiconductor, we study the correlations between the spin, valley pseudospin, and layer pseudospin indices through photo-generated excitons. Patterning our crystals into field-effect transistors (FETs) offers the additional handle of applied electric fields. Within this framework, we examine topics including optically addressing the valley pseudospin index, creating superposition states of valley-separated excitons, electrostatic manipulation of coupled spin and layer pseudospin indices, efficient and valley-specific photon up-conversion, and non-linearity in optically driven membrane oscillations. While the predominant tool of choice is photoluminescence (PL) spectroscopy, application of electrostatic voltages combined with variations on this technique such as photoluminescence excitation (PLE), reverse-PLE, and resonant fluorescence spectroscopy provide additional depth to the measurements.

Interest in two-dimensional TMD semiconductors such as WSe_2 stems from their combination of a highly compact structure, stability in ambient conditions [7], strongly bound excitonic states with visible or NIR wavelength emission [3, 4], electrically tunable emission [8, 9], and possession

of novel quantum indices [5, 10–12]. Such properties lend these materials to applications in solar cells [13], LEDs [14–18], and valley index-based information processing [19–24].

We begin in Chapter 2 with a brief introduction to ultra-thin TMDs and an overview of the basic theory underlying their optical and quantum properties which emerge at the monolayer limit. This includes an outline of the symmetries of the underlying hexagonal lattice and the coupling of polarized optical fields to individual valleys.

Following this, Chapter 3 establishes the optoelectronic properties of monolayer WSe_2 from room to cryogenic temperatures, as well as the effect of electrostatic doping on excitonic emission. This chapter serves to demonstrate the dominance of excitonic species in the optical response of these monolayer semiconductors along with the ease with which electrostatic fields can tune between various excitonic species.

In Chapter 4 we delve into an exploration of the valley pseudospin index, with the optical excitation and detection of valley-polarized excitons. After establishing the robustness of the valley index, we introduce the theory for, and experiments behind, the creation of the first superposition state of momentum-space separated excitons. The contrast between neutral and charged excitonic states is also covered.

Continuing in the theme of correlated spin and pseudospin indices, we turn to bilayer WSe_2 and the introduction of the layer pseudospin in Chapter 5. We begin with the theory of spin-layer pseudospin coupling and the effects of applied electric fields. The direct coupling of this pseudospin with electric fields allows us to examine behaviors such as spectral separation of intra- and interlayer excitonic emission, an all-electrical spin Zeeman effect, and the first demonstration of *charged* exciton intervalley coherence.

We then begin Chapter 6 by proposing a model of hybridized exciton/trion-polaron states in monolayer WSe_2. The supporting data shows efficient, valley-maintaining photon up-conversion by an energy of $> 10\ k_BT$, demonstrating the correlation between low-energy excitation of trions and emission at the neutral exciton energy. Numerous gate- and temperature-dependent studies likewise support the proposed model. Finally, we present evidence supporting the assignment of the $X^{-\prime}$peak, related to the fine structure of the negatively charged exciton of Chapter 3, to a multi-valley charged exciton configuration.

This work concludes in Chapter 7 with preliminary results on optically driven nanodrums. Here,

resonant driving of suspended TMD membranes by optical fields modulated at rf frequencies causes nm-scale mechanical oscillations. By increasing the driving force, the oscillation amplitude moves into a strongly nonlinear regime, characteristic of non-linear Duffing oscillators. Avenues to overcome the technical limitations faced here are then proposed for future studies.

Chapter 2

CRYSTAL STRUCTURE AND OPTICAL INTERACTIONS IN MONOLAYER TRANSITION METAL DICHALCOGENIDES

Through this chapter we briefly introduce the basic theory relevant to our optical studies of ultrathin TMDs, in light of their crystallographic structure and interactions with optical fields. For a more thorough treatment of TMD band structures, spin splittings and polarization, as well as optical transitions across a broad frequency range, we refer the reader to References [6, 25, 26] and related reviews [27, 28].

2.1 Lattice Structure of Monolayer TMDs

The discovery of monolayer transition metal dichalcogenides (TMDs) came a decade ago, alongside the announcement of successful isolation of monolayer graphene [2]. While monolayer TMDs possess a hexagonal crystal structure similar to graphene, their 3-atom thickness offers significant differences in their electronic and optical characteristics. Throughout this work, we only consider ultrathin TMDs obtained from bulk crystals of the polytype 2H, though polytype 3R is also quite common [29]. Figure 2.1a presents the unit cell of monolayer TMDs while Figure 2.1b offers a top-down (or out-of-plane) view of the crystal. As shown by the unit cell, two layers of chalcogen atoms sandwich the layer of transition metal atoms, with a trigonal prismatic coordination. In bulk form, 2H TMDs belong to the inversion-symmetric, D_6h symmetry group. As is apparent in Figure 2.1a, monolayer TMDs have a broken inversion symmetry and pertain to the D_{3h} group [30]. An important consequence of inversion symmetry breaking, relevant to our optical studies, is the emergence of a direct bandgap [31] which produces the highest photoluminescent yield in the thinnest crystals [3, 4].

In addition to the emergence of a direct bandgap, thinning of TMDs down to monolayer form induces strong quasiparticle confinement and an anisotropic, reduced dielectric screening [32–34], which provide increased electron-hole overlap and enhanced Coulomb interactions, respectively.

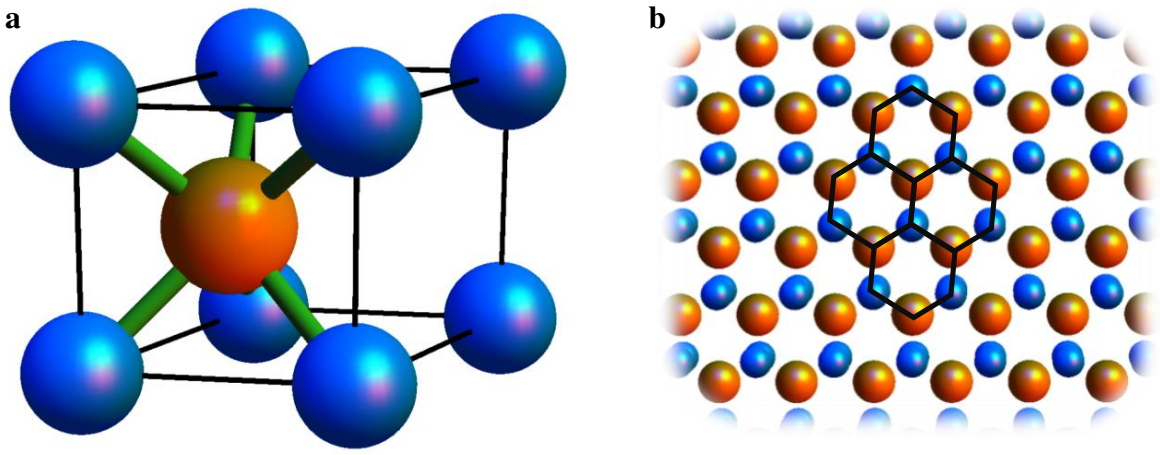

Figure 2.1: **a,** Schematic of monolayer TMD unit cell with the transition metal atom (orange sphere) covalently bonded (green rods) to the three chalcogen atoms (blue spheres). The black lines are simply to aide with spatial perception. **b,** Top-down view of a monolayer TMD lattice. Black line overlays outline the hexagonal crystal structure.

The combination of these effects leads to the dominance of the exciton optical oscillator strength [30, 35] and large binding energies [36–40], along with the formation of tightly bound trions [8, 34, 41, 42]. In light of this, consideration of the excitonic (vs. single-particle) bands may be advantageous or even necessary [43, 44].

Beyond their optical properties, atomically-thin TMDs also carry significant implications for ultrathin FETs due to their reduced dielectric screening and, in contrast to graphene, a band gap of ≈ 2 eV which provides a high on-off current contrast ratio [45]. Though such FETs have historically suffered from high contact resistances and mobilities below theoretical predictions, advances in sample quality and fabrication of electrical contacts have significantly improved device functionality in recent years [46–48]. Additionally, schemes such as chemical doping and ion gel gating which exploit the large surface-to-volume ratios of 2D materials have shown strong electrostatic doping [49, 50], and even the transition to a superconducting state at high carrier densities [51].

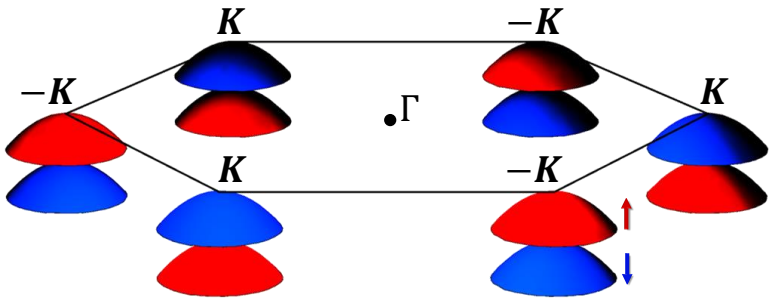

Figure 2.2: Depiction of the uppermost valence bands in monolayer TMDs near the corners of the first Brillouin zone. We denote the large spin-orbit coupling-induced spin splitting by the band color. With an energy separation of $O(10^2)$ meV, low-energy carriers within a given valley only possess one spin orientation (i.e. spin and valley indices are intimately coupled).

2.2 Coupling of Optical Fields to Spin and Valley

Another vital aspect of monolayer TMDs stems from their large spin-orbit coupling, largely contributed from the heavy transition metal atoms [12]. At the high-symmetry corners of the 1st Brillioun zone, the low-energy electronic bands predominantly come from the transition metal d-orbitals. With the combination of time reversal symmetry ($f(\mathbf{k}) = -f(\text{-}\mathbf{k})$) and broken inversion symmetry ($f(\mathbf{k}) \neq f(\text{-}\mathbf{k})$), the spin-orbit coupling component of the Hamiltonian becomes valley-dependent. This dictates a valley dependent spin splitting, which in the valence bands of commonly studied TMDs yields an energy separation of 100's of meV (460 meV in monolayer WSe_2) near the K points [12], as depicted in Figure 2.2. As the figure shows, a reversal of spin orientation occurs upon switching from valley +K to -K. This large magnitude of the splitting then produces low-energy carriers which possess strongly coupled valley and spin indices [6]. With the additional property of a valley-contrasting Berry curvature, this correlation between spin and valley indices gives rise to unique phenomena such as combined spin and valley Hall effects under application of an in-plane electric field [6, 21, 52].

Indirect measures of this valence band splitting have found values consistent with calculations [8, 53, 54]. Additionally, in both monolayer and bulk TMDs, the magnitude of the band splitting, as well as the contrasting spin orientation, has been directly verified via photo-emission spectroscopy

measurements with values likewise in good agreement with theoretical predictions [55–59]. While large band splitting strongly couples the valley and spin indices in the valence band, the conduction band spin splittings are an order-of-magnitude weaker [25,26,44,60,61]. Importantly, the sign of the conduction band splitting varies with transition metal species, where W (Mo) TMDs yield a positive (negative) energy splitting between the dipole transition-allowed and -forbidden bands [25]. This directly affects whether optical transitions populate the lowest-energy conduction band.

A crucial aspect of this work and another effect of inversion symmetry breaking is the emergence of valley-dependent optical selection rules for interband transitions away from the zero-momentum (Γ) point of the 1st Brillouin zone [22]. This coupling between optical fields and valley index stems from the finite magnetic moment (with an associated Berry curvature) that occurs at each valley due to inversion symmetry breaking. By taking the orbital magnetic moment as calculated within a $\mathbf{k}\cdot\mathbf{p}$ analysis and projecting it along the light propagation direction, one arrives at the $\mathbf{k}$-space dependent degree of circular polarization [22]

$$\eta(\mathbf{k}) \equiv \frac{|P_+(\mathbf{k})|^2 - |P_-(\mathbf{k})|^2}{|P_+(\mathbf{k})|^2 + |P_-(\mathbf{k})|^2} \tag{2.1}$$

where $P_\pm(\mathbf{k})$ denotes the $\mathbf{k}$-dependent oscillator strength for $\sigma_\pm$ circularly polarized optical fields. Since the lowest-energy bands of monolayer TMDs form direct bandgaps at the Brillouin zone corners (K points), derivation of $P_\pm(\mathbf{k})$ near $\mathbf{k} = \pm\mathbf{K}$ offers insight into the optical selectivity of momentum-separated bands. In the work of Xiao *et al.*, they find an oscillator strength [6]

$$|P_\pm(\mathbf{k})|^2 \propto \left(1 \pm \tau\frac{\Delta - \tau s_z \lambda}{\sqrt{(\Delta - \tau s_z \lambda)^2 + (2atk)^2}}\right)^2 \tag{2.2}$$

which intimately depends on the +K or -K valley index, τ, as well as the spin index, s_z. Note that k here now denotes the wave vector separation from the $\pm$K points. Equation 2.2 shows selective excitation of carriers at the $\pm$K corners of the Brillouin zone (i.e. $k = 0$) to be exact for $\sigma\pm$ polarized optical fields. This endows TMDs with the unique capability of facile excitation of carriers with coupled spin and valley indices. For finite k, the degree of variation from perfect valley selectivity then depends on the comparative magnitudes of the energy splitting from the bandgap, Δ, spin-orbit coupling, λ, lattice constant a, and the valley-mixing hopping integral, t. Importantly, even for significant deviations from the valley centers, $atk \ll \Delta \pm \lambda$, implying a large 'neighborhood' around the K points for which these valley-specific optical selection rules remain robust, and offering the

opportunity to optically prepare valley-polarized carriers both resonantly and non-resonantly [6,62].

With a valley-dependent spin orientation for the low-energy electronic bands, we see that scattering of e.g. a hole state from K to -K requires a simultaneous transfer of crystal momentum and spin flip. We thus expect the valley polarization of such carriers to be quite robust. However, the optical response of ultrathin TMDs is dominated by excitonic, and not single-particle, states [35]. Since photoexcited carriers rapidly bind to form neutral and charged excitons, scattering mechanisms relevant to excitonic states must be examined. While such processes eliminate expectations of 100% valley-polarized emission, the exciton's hole state always originates from highly spin- and valley-polarized bands, offering an anchor for the creation of valley-polarized excitons. Indeed, initial measurements of optically-prepared excitons in TMDs found significant valley polarization in monolayer MoS_2 [53, 62, 63] and WSe_2 [9]. Still, the absence of valley polarization in intrinsic monolayer $MoSe_2$ [64] and time-resolved studies which show an ultra-fast decay of such polarization [65–69] indicate the presence of efficient intervalley scattering mechanisms [44, 70–72].

We defer further discussion of valley depolarization mechanisms to Chapter 4 and now move onto our experiments in monolayer WSe_2. Additional theoretical background relevant to the work here will be presented in later chapters, nearer to the applicable experiments.

Chapter 3

OPTICAL INTERACTION IN MONOLAYER WSe_2

In this chapter, we briefly outline the method used for obtaining and identifying monolayer TMD flakes. We then present the (unpolarized) optical absorption and emission properties of monolayer WSe_2 FETs, including the effects of temperature and electrostatic gate voltages. Unless otherwise specified, photoluminescence measurements throughout this work maintain the sample in vacuum ($< 10^{-5}$ Torr) with 10 – 40 μW of 660 nm cw excitation focused to a spot size of $\approx 1\mu$m on the sample.

3.1 Monolayer TMD Identification

To obtain WSe_2 monolayers, we utilize the same technique employed in the discovery of graphene - the 'Scotch Tape' method [73]. Though not a scalable manufacturing technique, this method has proven to consistently provide higher quality monolayers than other methods, such as those grown by CVD and PVD [74]. After exfoliation onto a highly doped silicon wafer covered with 285 nm of SiO_2, monolayers are reliably identified under a microscope by their optical contrast [75]. Figure 3.1a shows an optical image of an exfoliated WSe_2 monolayer, as well as nearby bulk WSe_2 for comparison.

Following initial identification using optical contrast, rapid confirmation of monolayer thickness can be readily accomplished by PL measurements in ambient conditions. A typical spectrum (see Fig. 3.1b) peaks at $\approx$ 750 nm, while variations in peak position larger than ± 5nm from 750 nm often indicate degraded optical quality, determined by significant defect contributions and reduced exciton emission at low temperatures. Figure 3.1b also presents a WSe_2 bilayer spectrum for comparison, which displays a significant red-shift and lower emission intensity relative to monolayer WSe_2 under the same experimental conditions. An additional method for optical confirmation of layer thickness lies in second-harmonic generation (SHG) measurements. The absence of inversion symmetry in crystals with an odd number of layers permits SHG, while inversion-symmetric crystals with even

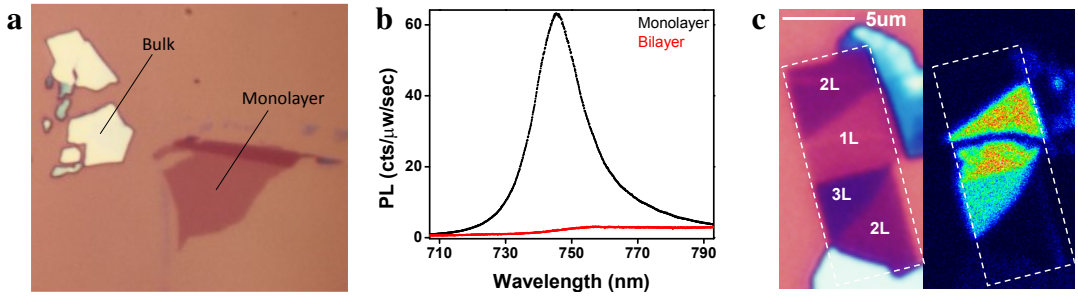

Figure 3.1: **a,** Optical microscope image of exfoliated monolayer and bulk WSe_2 on an SiO_2/Si wafer. **b,** Room temperature photoluminescence spectra of monolayer and bilayer WSe_2, showing increased intensity and blueshift of emission at the monolayer limit. **c,** Microscope image of WSe_2 ranging from 1-3 layer thickness with the corresponding two-dimensional SHG intensity map.

layer number show no signal [76–78]. A two-dimensional spatial map of SHG signal from WSe_2 crystals of varying layer number is shown in the right panel of Fig. 3.1c alongside its corresponding optical microscope image. Comparing the number of layers identified by optical contrast and AFM measurements (not shown) with the SHG intensity shows the strong correlation between the absence of inversion symmetry and strong SHG.

3.2 Optoelectronic Response of Excitons in WSe_2

In this section, we explore the basic optical properties of monolayer WSe_2 devices at low temperature, which are strongly dominated by the tightly bound excitons characteristic of monolayer TMDs [35]. We show this through measurements of differential reflectance and PL emission directly taken from exfoliated flakes.

3.2.1 As-Prepared Optical Characteristics

When cooling monolayer WSe_2 to 30K, we find that the strong emission found at room temperature (Fig. 3.1a) simultaneously narrows and blue-shifts by approximately 35 meV and 80 meV, respectively [79]. This energy shift and spectral narrowing can be seen in the temperature-dependent PL data of Fig. 3.2b. As gate-dependent studies in the next section verify, the dominant emission of

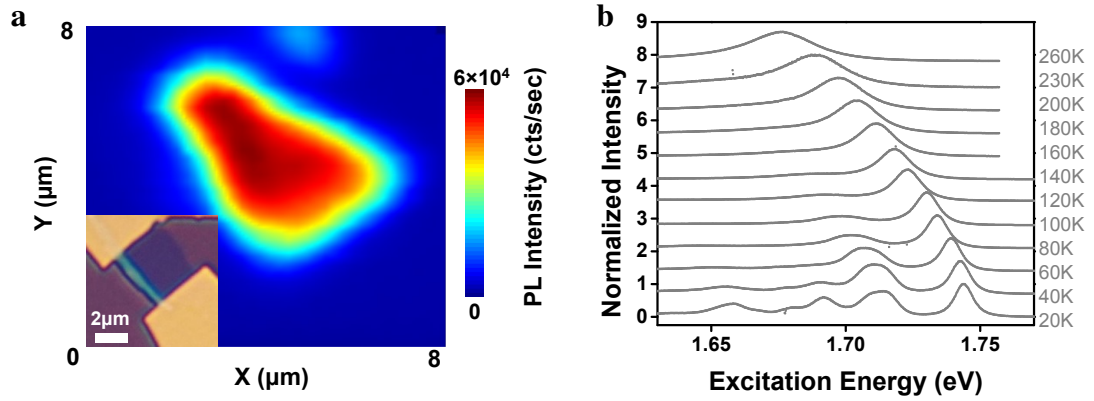

Figure 3.2: **a,** Two dimensional scanning PL map showing integrated exciton emission intensity of the WSe_2 device shown in the microscope image (inset). **b,** Normalized temperature-dependent PL spectra of monolayer WSe_2.

intrinsic WSe_2 at both cryogenic temperatures and ambient conditions stems from the dominant oscillator strength of neutral exciton states [9, 35]. Spatial mapping of the excitonic offers insight into the overall optical quality of our crystals. Figure 3.2a presents the emission intensity of the neutral exciton over the two-dimensional range shown in the optical image (inset). The emission indicates a homogeneous response across our monolayer samples, free of point-like defects found in some PVD-grown crystals [80], pointing to the high quality of the crystals examined here.

Measurements of the white light differential reflectivity ($\Delta R/R$) spectrum also show the strong excitonic transitions in WSe_2, and offer a probe analogous to absorption measurements. The broadband $\Delta R/R$ spectrum of WSe_2 at 30 K is shown in Fig 3.3a. Here the sharp derivative features near 1.7 eV and 2.2 eV stem from the excitonic A and B states derived from the spin-split valence bands [54, 81], and are superimposed on a much broader feature arising from interference caused by the supporting SiO_2/Si layered substrate. Figure 3.3b displays a zoomed-in portion of the $\Delta R/R$ curve (black) with its corresponding PL spectrum (red), showing the alignment of the highest-energy PL peak with the sharp $\Delta R/R$ derivative feature. This highest-energy PL peak at ≈ 1.75 eV, and the sharp dR/R feature, we assign to the neutral A exciton, X^o. Due to the absence of a surrounding dielectric environment, strong Coulomb interactions lead to large binding energies for the neutral

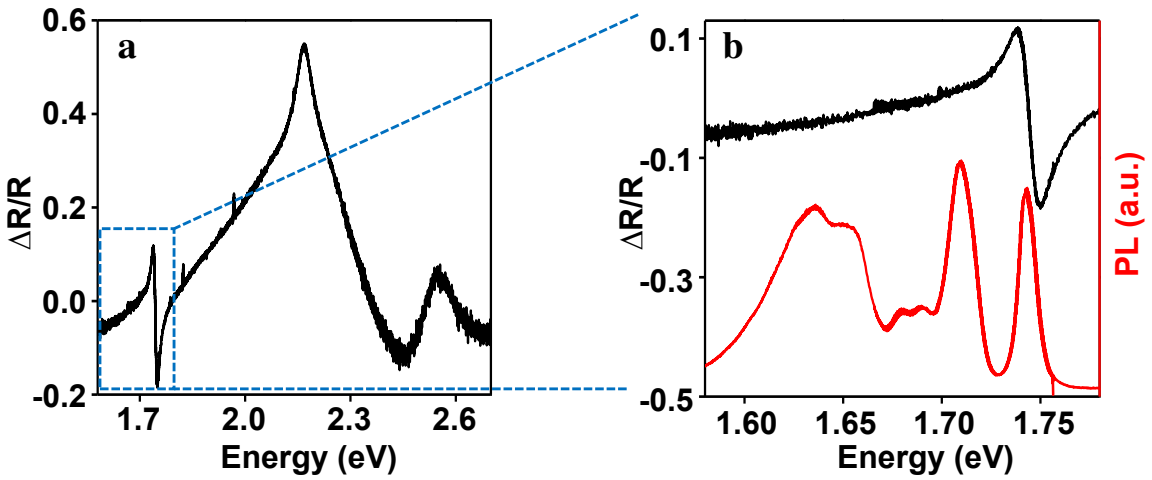

Figure 3.3: **a,** Broadband differential reflectance spectrum of monolayer WSe_2 at 30 K. The sharp derivative features arise from excitonic transitions. **b,** Zoom-in comparison of differential reflectivity and PL response show that the dominant spectral features in both arise from neutral excitons.

exciton, where values of 370 meV [39] and >790 meV [82] have been determined, while scanning tunneling spectroscopy measurements find a band gap of 2.21 eV [83], indicating an ≈ 500 meV binding energy. The lower energy PL peaks of Figure 3.3b stem from defect-bound states ≈100 meV below X^o [84] and charged excitons ≈30 meV below X^o, which are discussed in the next section.

3.2.2 Electrostatic Gating of Excitonic States

In this section, we pattern WSe_2 monolayers into field-effect transistor (FET) devices to allow for electrical control of the excitonic emission. Electrode patterns are written using standard microfabrication techniques followed by electron-beam evaporation of 5/50 nm of V/Au, resulting in a two-terminal monolayer device (see inset of Fig. 3.2a). For doping-dependent PL measurements, the device electrodes are held at ground while application of a gate voltage, V_g, to the highly-doped silicon backgate drives excess carriers into the sample. Thus, positive (negative) gate voltages correspond to excess electron (hole) doping within the WSe_2 layer.

The gate-dependent PL measurements of monolayer WSe_2 shown in Fig. 3.4 reveal highly

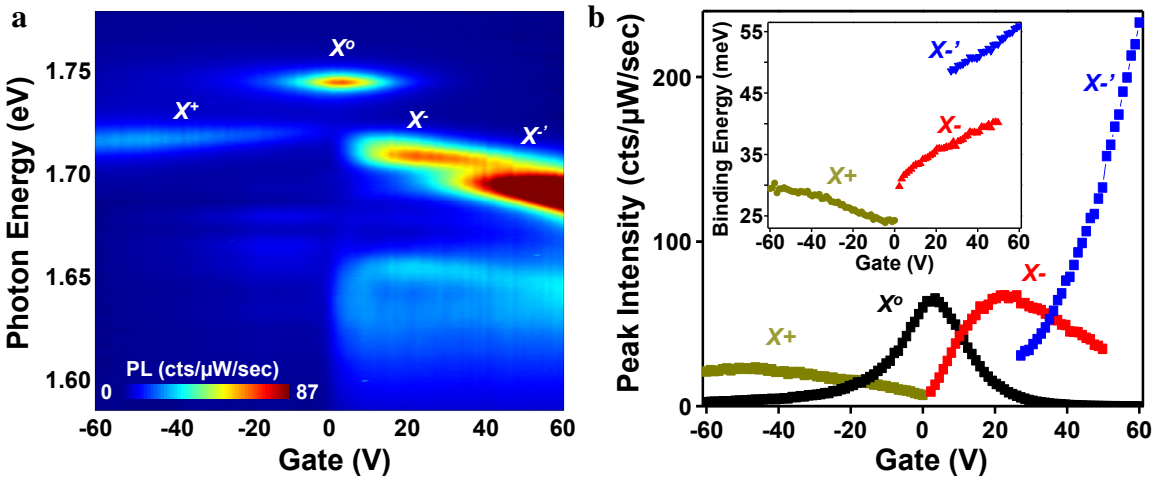

Figure 3.4: **a,** Photoluminescence intensity as a function of emission energy and applied electrostatic gate voltage. **b,** Extracted PL peak intensity for X^o, X^+, X^-, and $X^{-\prime}$. Inset: Trion charging energy determined by subtracting the peak emission energy of the trion from that of the neutral exciton.

tunable excitonic states and emission energies, as with similar measurements of monolayer $MoSe_2$ [8,9]. Near zero gate voltage, neutral exciton emission, X^o, dominates the spectrum (highest energy emission in Fig. 3.4a, black dots in Fig. 3.4b). The data show no energy shift of the X^o emission with increasing doping, but only a monotonic decrease in intensity. With the excess doping, we also see the formation of positively (X^+) or negatively (X^-) charged excitons (trions) which emit near 1.72 eV. Additionally, we also find the emergence of a feature near 1.69 eV at high electron doping levels, which we label as $X^{-\prime}$. A detailed examination of this state specifically will be addressed in Chapter 6, and for now we attribute it to the fine structure of X^-. The broader features seen at energies below 1.67 eV likely stem from impurity-bound states and/or phonon replicas [66, 84].

Intuitively, increasing electrostatic doping causes the trion intensity to increase concomitantly with the decrease of X^o emission (see Fig. 3.4b). We note that while the intensities of X^o, X^-, X^+ are all of a similar magnitude, $X^{-\prime}$ grows at a much quicker rate and to much larger amplitudes. In the inset to Fig. 3.4b we plot the extracted trion charging energy as a function of applied gate voltage. We find that near their onset, the charging energies of the trion states are $\approx$ 25 meV, 30 meV, and 50 meV for X^+, X^-, and $X^{-\prime}$, respectively, but quickly grow with doping by 5 meV, 9 meV, and 7 meV for the voltage range explored here. These large trion dissociation energies make room temperature

studies and applications feasible, especially given the additional advantage of greater trion stability than even the more red-shifted defect states [85].

3.3 Conclusion

The optical characteristics of monolayer WSe_2 shown at both cryogenic and ambient temperatures are strongly dominated by the excitonic response, which makes monolayer TMDs likely candidates for optoelectronic applications and technologies. Our measurements demonstrate the widely tunable optical properties of TMDs available due to their ultrathin form and strongly interacting carriers, and set the stage for an investigation of the unique valley-physics which arise from their crystal structure.

Chapter 4

OPTICAL MANIPULATION OF VALLEY PSEUDOSPIN

With the basic optical properties of monolayer WSe_2 now established, this chapter focuses on the novel valley physics afforded by the intrinsic coupling of light fields to the momentum-separated direct bandgaps found in monolayer TMDs. Following the basic theory of valley-specific, optically prepared excitonic states outlined in Chapter 2, this chapter first examines the optical preparation and readout of valley polarized exciton and trion states. We then turn to the theory and experiments which demonstrate the first observation of a coherent superposition of valley excitons [9]. The chapter concludes by explaining the observed lack of valley coherence in charged excitonic states. For a more extensive review of the spin and pseudospin physics in monolayer TMDs, including WSe_2, we point the reader to Reference [86].

4.1 Valley Polarization in Monolayer WSe_2

Following the valley-dependent optical selection rules developed in Ref. [6], as well as observations of valley polarized excitonic states in monolayer MoS_2 [53,62,63], we pursue measurements of valley polarized states in monolayer WSe_2 via polarization-resolved PL measurements. After excitation by a circularly polarized beam at 1.88 eV, we monitor the emission for both co- and cross-polarized detection, the difference of which then reveals the remnant degree of valley polarization, η, after electron-hole recombination (see Equations 2.1-2.2). We perform these measurements as a function of the applied electrostatic gate voltage, allowing us to resolve the degree of valley polarization for all excitonic states.

Figure 4.1a shows spectra obtained at selected gate voltages under σ^+excitation and σ^+(black data) and σ^-(red data) polarized detection. For the complete set of polarization-resolved PL spectra, see Appendix A. Our measurements elucidate a strong valley polarization for $X^{-\prime}(V_g = +60$ V), $X^-(V_g = +10$ V), $X^o(V_g =$ -5 V), and $X^+(V_g =$ -60 V) [9]. Robust valley polarization for all excitonic species indicates that photoexcited carriers remain within their respective valleys throughout the

duration of the excitonic lifetimes, irrespective of the excitonic state they form. This establishes the valley index as a robust quantum index in monolayer WSe_2. Though a suppression of intervalley scattering is expected due to the strong spin-valley coupling of the uppermost WSe_2 valence bands [6], the large valley polarization observed is more a result of ultrafast exciton (few ps) and trion (10's of ps) lifetimes than of exceptionally long (>1 ns) valley scattering times [66].

We also investigate the excitation energy-dependent response of valley polarized excitons. The valley-dependent optical selection rules presented in Chapter 2 are exact at the ±K valleys, but increasing excitation energies lead to carrier excitation progressively further from these high symmetry points where the polarization-specific selection rules become mixed [6]. Thus, measuring valley polarization while varying excitation energy offers insight into the size of k-space neighborhood in which valley optical selection rules remain robust [62]. Figure 4.1c displays the PL spectra obtained for excitation energies ranging from nearly resonant (1.79 eV) up to 580 meV above the emission (2.33 eV). By varying the electrostatic gate voltage for each excitation wavelength, we can extract the degree of valley polarization for each excitonic state, the results of which are plotted in Figure 4.1d. The gradual decrease in valley polarization with increasing detuning stands in contrast to measurements in monolayer MoS_2 [53, 63], but coincides with similar measurements performed recently in WSe_2 [87]. This indicates that the neighborhood within which a given optical polarization helicity couples to a single valley is significantly larger in WSe_2 than in its sister material MoS_2.

Next, we examine the power-dependent evolution of valley polarization. Figure 4.2a presents two representative spectra at high and low excitation power (1.88 eV excitation), which show the constant degree of X^o valley polarization seen over the power range explored here. The summarized excitation energy and power-dependent valley polarization is shown in Fig. 4.2b. We find that a slight upward slope with increasing power can be attributed to a small unpolarized contribution within each spectrum which stems from the broad defect state emission. Since defect states become saturated with increasing optical powers (c.f. emission at 1.65 eV for low and high powers), their emission intensity relative to the excitonic states diminishes [88], resulting in a small, artificial increase in polarization values. We thus conclude that X^o valley polarization is insensitive to excitation power up through 25 μW. Note that reliable extraction of valley polarization values for X^- across this range of excitation powers is inhibited by the dominance of defect emission at low intensities.

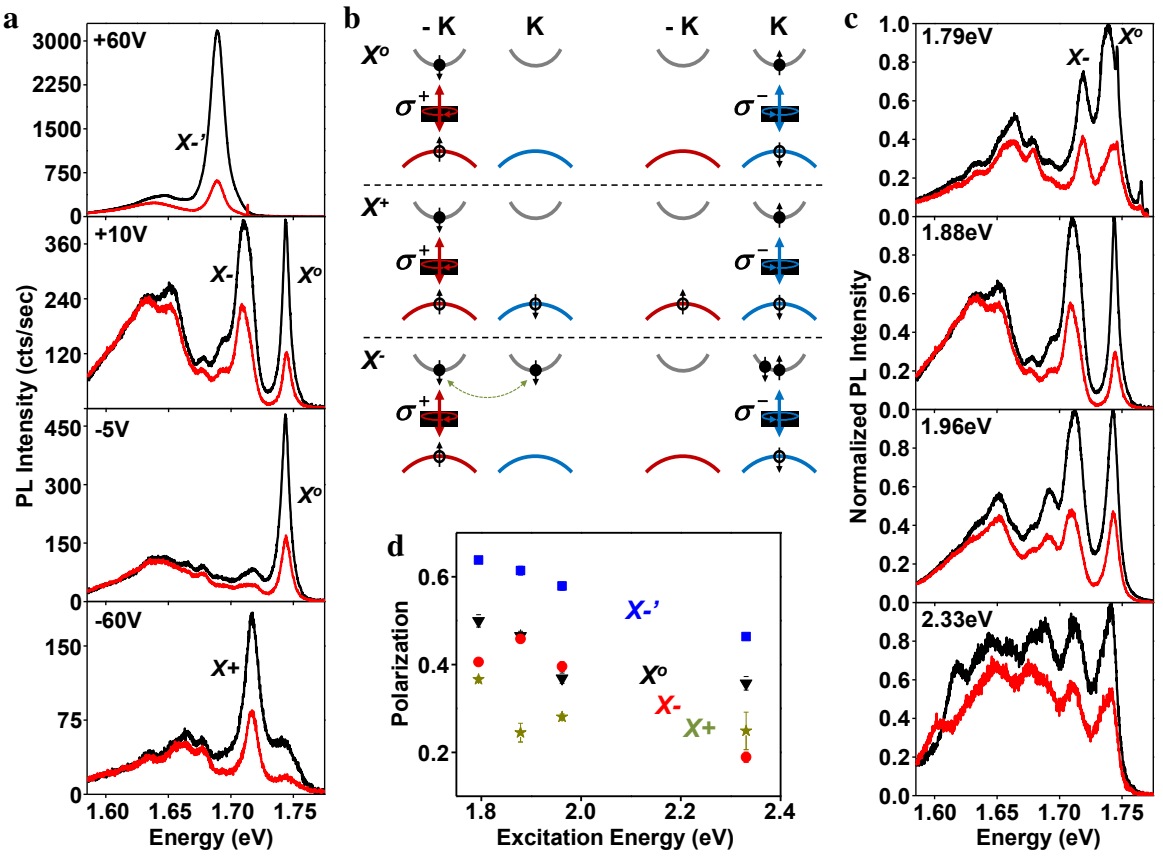

Figure 4.1: **a,** Polarization-resolved PL spectra of monolayer WSe_2 at select gate voltages, revealing significant significant circular (i.e. valley) polarization for the labeled excitonic species. The upper left corner indicates the value of the applied gate voltage. **b,** Schematic representations of possible ±K valley excitonic configurations for X^o(upper), X^+(middle), and X^-(lower), with corresponding optical selection rules. Green dashed arrow indicates electron-electron exchange interaction. **c,** Normalized polarization-resolved PL spectra for varying excitation energies (indicated in upper left corner) at intrinsic doping levels. **d,** Degree of valley polarization extracted for each excitonic species as a function of excitation energy.

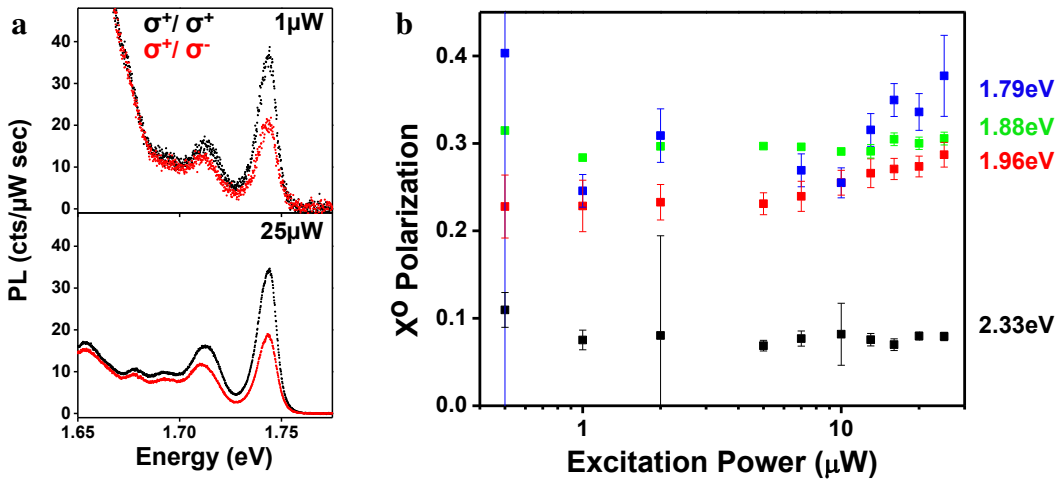

Figure 4.2: **a,** Polarization-resolved PL spectra of monolayer WSe_2 at high and low power. **b,** Valley polarization of X^o extracted for each excitation energy for a range of laser powers. Error bars show polarization standard deviation of 15 peak points.

4.2 Coherent Superposition of Valley States

With the valley-dependent excitation and emission properties of WSe_2 established, we now turn our attention to our measurements which comprise the first demonstration of a coherent superposition of valley excitonic states [9]. We will first establish the theory behind the creation of coherent inter-valley excitonic states, then present our observations, and conclude by describing excitonic configurations prohibited from displaying inter-valley coherence.

4.2.1 Theory of Valley Exciton Superposition States

The drive to create a coherent superposition state of valley-separated carriers stems from similar motivations in the exploration of electron spin and photon superposition states - namely the ability to encode information in a binary quantum index [89]. Notably, the ease with which the valley pseudospin can be selectively addressed and read with polarized light makes it especially appealing to research and technology alike. By examining the valley-specific optical selection rules (see Fig. 4.1b), one immediately notices that equal intensities of $\sigma^+$and σ^-excitation will lead to equal pro-

portions of +K and -K valley carriers. In this configuration the relative phase between individual excited carriers in opposing valleys is created at random, no superposition states form, and the resulting emmission is unpolarized. However, if each absorbed photon is prepared in a superposition of $\sigma^+$and σ^-polarizations, which is linear polarization, then photoexcitation of carriers will occur at both +K and -K valleys, with a given phase between the two components. Since excitons dominate the spectral response in monolayer TMDs, we express this linear superposition of valley excitons as [9]

$$\sum_{\mathbf{q}} a(\mathbf{q}) \left(e^{-i\theta} \hat{e}^{+}_{-\mathbf{K}+\frac{\mathbf{q}}{2},\downarrow} h^{+}_{\mathbf{K}-\frac{\mathbf{q}}{2},\Uparrow} \; + \; e^{i\theta} e^{+}_{\mathbf{K}+\frac{\mathbf{q}}{2},\uparrow} h^{+}_{-\mathbf{K}-\frac{\mathbf{q}}{2},\Downarrow} \right) |\Phi\rangle \tag{4.1}$$

Here, $a(\mathbf{q})$ is the superposition coefficient which depends on the relative wave vector, $\mathbf{q}$, measured from the ± K points, $|\Phi\rangle$ is the vacuum state, and $\hat{e}^{+}_{\mathbf{k},\uparrow}$ ($\hat{h}^{+}_{\mathbf{k},\Uparrow}$) creates a spin up electron (hole) with momentum $\mathbf{k}$ in the conduction (valence) band. The orientation of the absorbed linearly polarized photon dictates the initial relative phase between valley components, θ. Only if equivalent quantum trajectories exist for both $|\mathbf{K}+\mathbf{q}\rangle$ and $|-\mathbf{K}+\mathbf{q}\rangle$ states in exciton formation will the relative phase be preserved and allow for the observation of inter-valley coherence.

4.2.2 Valley Depolarization and Decoherence Mechanisms

Since the degree of inter-valley coherence remaining after creation of a superposition state depends on the relative rates of inter-valley decoherence processes and electron-hole recombination, we now examine the relevant mechanisms. To do so, we separate the Coulomb interaction into intra- and inter-valley components of the electron-electron interaction, which are [9]

$$V_{intra} \equiv \sum_{\boldsymbol{\alpha}_1,\boldsymbol{\alpha}_2} \sum_{\Delta\boldsymbol{q},\boldsymbol{q}_1,\boldsymbol{q}_2} v(\Delta\mathbf{q}) \hat{e}^{+}_{\boldsymbol{\alpha}_1+\boldsymbol{q}_1-\Delta\boldsymbol{q}} \hat{e}^{+}_{\boldsymbol{\alpha}_2+\boldsymbol{q}_2+\Delta\boldsymbol{q}} \hat{e}_{\boldsymbol{\alpha}_2+\boldsymbol{q}_2} \hat{e}_{\boldsymbol{\alpha}_1+\boldsymbol{q}_1} \tag{4.2}$$

$$V_{inter} \equiv v(\mathbf{K}) \sum_{\Delta\boldsymbol{q},\boldsymbol{q}_1,\boldsymbol{q}_2} \hat{e}^{+}_{\boldsymbol{K}+\boldsymbol{q}_1-\Delta\boldsymbol{q}} \hat{e}^{+}_{-\boldsymbol{K}+\boldsymbol{q}_2+\Delta\boldsymbol{q}} \hat{e}_{\boldsymbol{K}+\boldsymbol{q}_2} \hat{e}_{-\boldsymbol{K}+\boldsymbol{q}_1} + h.c. \tag{4.3}$$

where alpha is the valley index and v($\mathbf{q}$) is the Fourier transform of the Coulomb potential. Since $\Delta\mathbf{q} \ll \mathbf{K}$, $v(\Delta\mathbf{q}) \gg v(\mathbf{K})$ and exciton formation will be dominated by V_{intra} rather than V_{inter}. However, none of the interaction terms in V_{intra} depend on valley index, and thus do not affect valley polarization and valley coherence, assuming identical dispersion in $\pm\mathbf{K}$.

We thus turn to the effects of V_{inter}, which do include valley depolarization and/or valley dephasing. For instance, fields such as $\langle \hat{e}^{+}_{-\boldsymbol{K}+\boldsymbol{q}_2+\Delta\boldsymbol{q}} \hat{e}_{\boldsymbol{K}+\boldsymbol{q}_2} \rangle$ scatter carriers between valleys and lead to valley depolarization. And while $\langle \hat{e}^{+}_{\pm\boldsymbol{K}+\boldsymbol{q}+\Delta\boldsymbol{q}} \hat{e}_{\pm\boldsymbol{K}+\boldsymbol{q}} \rangle$ only scatters within the ±K valley, any difference between valleys (i.e. $\hat{e}^{+}_{\boldsymbol{K}+\boldsymbol{q}+\Delta\boldsymbol{q}} \hat{e}_{\boldsymbol{K}+\boldsymbol{q}} - \hat{e}^{+}_{-\boldsymbol{K}+\boldsymbol{q}+\Delta\boldsymbol{q}} \hat{e}_{-\boldsymbol{K}+\boldsymbol{q}}$) will lead to oscillations of the relative phase, θ. An oscillation of the phase will leave the exciton in a superposition state, with resultant linearly polarized emission, but time averaged measurements of many such photons show un-polarized emission (i.e. a loss of coherence).

Other mechanisms for exciton binding include long and short wavelength phonon scattering. The former scatters within valleys, independent of the valley index, leaving valley polarization and coherence unaffected, while the latter affects both through inter-valley scattering. This same analysis holds for scattering by smooth vs. atomically-sharp impurity potentials within the lattice.

An important means for relaxation of inter-valley superpositions comes from exchange interactions between constituents of the excitonic state [90]. This interaction leads to a stark contrast between the response of superposition states of excitons and trions, with significant bearing on the results we present on bilayer WSe_2 in Chapter 5. The long-range part of the exchange interaction known as the longitudinal-transverse splitting, $\Omega(\mathbf{k}_\perp)$, can lead to valley depolarization. However the D_{3h} symmetry of monolayer WSe_2 dictates that $\Omega(\mathbf{k}_\perp) \propto \mathbf{k}_\perp$ which vanishes at $k_\perp = 0$. Still, finite $\mathbf{k}_\perp$ contributions to the PL signal arise from e.g. phonon-assisted emission, and reduce the total valley polarization and coherence. From the short-range component of exchange, two bright excitons may transition to two dark excitons [90]. However, the large energy splitting ($\approx$ 30 meV) between the spin-split conduction bands in WSe_2 should render this process largely irrelevant.

We expect the most significant effects of carrier exchange in comparisons of coherent superpositions of valley states for neutral and negatively charged excitons [9]. The difference between the two stems from the additional exchange interaction afforded by the trion's extra electron. We ignore the positive trion due to the following. When considering optically-active, lowest-energy states, a coherent superposition state of neutral excitons necessarily consists of the two X^o configurations shown in the upper panel of Fig. 4.1b. Similarly, the 100's meV energy splitting of TMD valence bands and Pauli exclusion only provide two configurations of positively charged excitons as shown in the central panel of Figure 4.1b). It is immediately apparent that a superposition of these two X^+ states cannot form since, upon electron-hole recombination and photon emission, the remaining

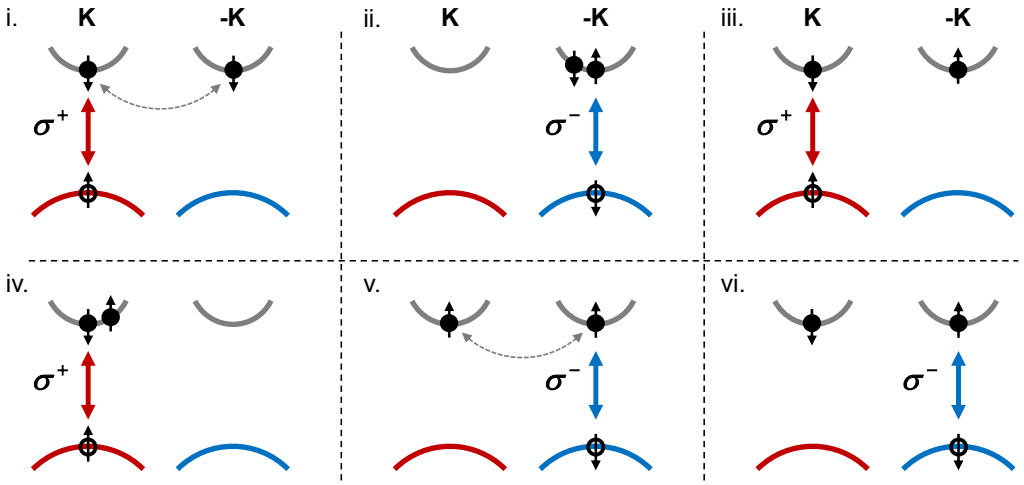

Figure 4.3: Schematic depiction of the allowed negative trion configurations. Filled (empty) circles denote electrons (holes) while blue/red marks spin-polarized bands of opposite orientation. The dashed lines in **i** and **v** indicate the electron-electron exchange interaction.

hole state must either lie spin up in valley -K or spin down in valley +K. Such specificity provides the 'which-path' information necessary to prohibit the formation of an X^+inter-valley superposition state.

For the negative trion, the argument is more involved as the number of possible X^-configurations jumps to 6, with 9 possible pairs where the recombining electron-hole pair resides in opposite valleys. We show these configurations in Figure 4.3. For all but 2 of the 9 pairs, formation of a superposition state is expressly prohibited due to inequivalent final electronic states after electron-hole recombination, as with X^+. However, there are two pairs for which a X^-superposition state is allowed, namely a superposition of Fig. 4.3 **i** and **ii** and of Fig. 4.3 **iv** and **v**. Here, the same electronic state (identical valley and spin indices) remains after recombination and photon emission. The difference here between the two configurations comprising the superposition state lies in exchange interactions experienced by only one component of the superposition. For example, in a superposition of **i** and **ii**, configuration **i** experiences electron-electron exchange interactions which

are not present in configuration **ii**. This electron-electron exchange interaction is given by [91]

$$\begin{aligned} J_{ee} &\approx -f_{ee} \int d\mathbf{r}_1 d\mathbf{r}_2 \psi^*_{\boldsymbol{K}c\downarrow}(\mathbf{r}_1)\psi^*_{-\boldsymbol{K}c\downarrow}(\mathbf{r}_2)v(\mathbf{r}_1-\mathbf{r}_2)\psi_{\boldsymbol{K}c\downarrow}(\mathbf{r}_2)\psi_{-\boldsymbol{K}c\downarrow}(\mathbf{r}_1) \\ &\approx -f_{ee}v(\mathbf{K})|\langle u_{-\boldsymbol{K}c\downarrow}|u_{\boldsymbol{K}c\downarrow}\rangle|^2 \end{aligned} \tag{4.4}$$

where $\psi_{\boldsymbol{K}c\downarrow}(\mathbf{r}) = e^{i\boldsymbol{K}\cdot\boldsymbol{r}}u_{\boldsymbol{K}c\downarrow}(\mathbf{r})$ is the conduction band Bloch state, $v(\mathbf{r})$ is the real space Coulomb potential, and f_{ee} represents the square modulus of the electron-electron envelope at zero distance. First principles Bloch function calculations [9] give $|\langle u_{-\boldsymbol{K}c\downarrow}|u_{\boldsymbol{K}c\downarrow}\rangle|^2 \approx 0.15$, while f_{ee} is on the order of $1/a_B^2$ [90]. Taking $v(\mathbf{q}) \propto 1/q$, we then have J_{ee} on the order of $\frac{0.1E_b}{Ka_B}$, where E_b is the exciton binding energy. With an excitonic binding energy of 100's of meV [39,82,83] and TMD Bohr radius $a_B \approx$1 nm [34,92,93], we extract an exchange splitting of $O(1)$ meV. This breaking of energy degeneracy between the two configurations will then result in inter-valley decoherence and eliminate the superposition state. We thus conclude that in monolayer WSe_2, a coherent superposition of valley states should only be seen for neutral excitons.

4.2.3 Observation of a Coherent Superposition of Valley Excitons

With the theoretical framework established, we now turn to the experiments which mark the first observation of a coherent superposition between valley-separated excitons [9]. The superposition state is optically created by linearly polarized, off-resonant excitation (130 meV above emission). As previously discussed, a linearly polarized photon couples to both K-valleys as a result of their circularly-polarized optical selection rules. If dephasing between each component of the superposition state occurs on timescales longer than the electon-hole recombination time, we expect to observe linearly polarized emission.

Figure 4.4 presents the PL spectra obtained under horizontally polarized excitation for horizontally (black) and vertically (red) polarized detection, at selected gate voltages. For the complete set of polarization-resolved PL spectra, see Appendix A. As expected from our discussion of exchange interactions in the previous section, we find a pronounced contrast between the behavior of neutral and charged excitonic states. Emission from X^o displays a high degree of co-linear polarization while it is entirely absent for X^+, X^-, and $X^{-\prime}$. Additionally, the degree of X^o linear polarization remains constant with changes in electrostatic doping. Though this response aligns with the anticipated behavior of an excitonic superposition state, we must also rule out anisotropies in the crystal lattice

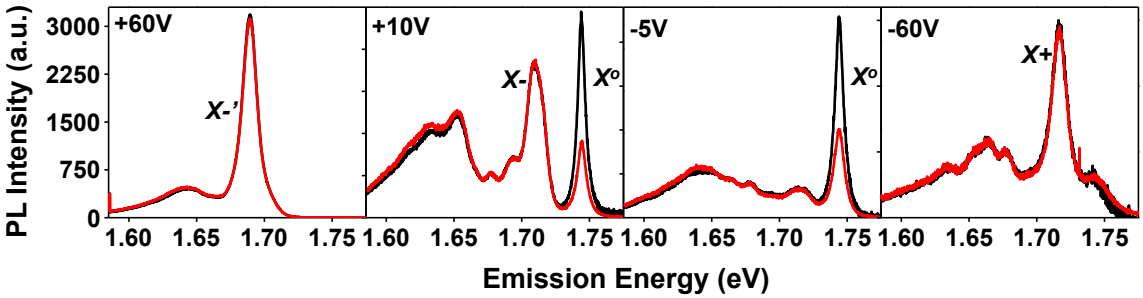

Figure 4.4: Photoluminescence spectra for horizontally polarized excitation and horizontally (black data) and vertically (red data) polarized detection under the applied electrostatic gate voltages indicated in the top left corner. While the neutral exciton shows significant linearly polarized emission, the charged excitonic species do not.

as a potential source of linearly polarized emission [94–96]. For this, we examine the orientation and degree of linearly polarized emission as a function of the excitation beam orientation. Importantly, for these studies care was taken in reflecting a linearly polarized beam with any polarization orientation away from the s- and p-polarized planes of reflective optics. Such reflections can often lead to significant ellipticity of the reflected beam due to phase shifts between s- and p-polarization components, the effect of which is especially pronounced in dielectric mirrors [97].

Figure 4.5a presents polar plots of the X^o PL response, where the radial coordinate corresponds to the PL intensity at each polarization detection angle (the angular coordinate). It is immediately apparent that the linearly polarized X^o emission follows the orientation of the exciting photons. We obtain a more quantitative analysis by fitting the detection polarization-dependent intensity with $r = A(1 + \rho \times \cos 2[x - \phi])$, shown as the black fitted lines. Here, ϕ denotes the X^o polarization angle, x the detection angle, and ρ the degree of linear polarization with normalization constant A. In Fig. 4.5b we show the fitted orientation angle, ϕ, as a function of incident polarization angle, θ (black data). The two are directly proportional. These data also show the degree of polarization, ρ, to be $\approx 33\%$ and isotropic with respect to θ (red data). This demonstrates that the observed linear polarization does not arise from crystallographic anisotropies.

From the isotropic response shown here, we conclude that excitation by a linearly polarized

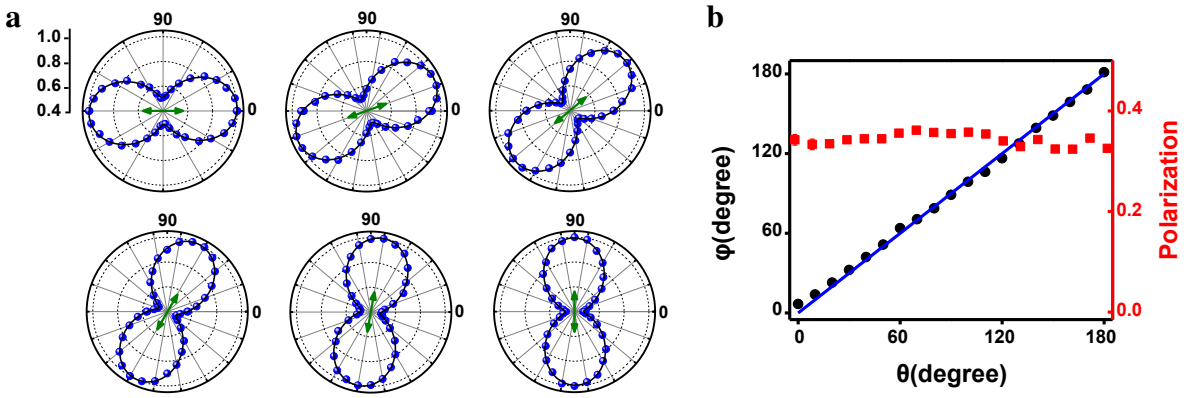

Figure 4.5: **a,** Photoluminescence intensity of X^o at $V_g = 0$ V as a function of polarization detection angle (black data), with the green arrow indicating the excitation beam polarization orientation. Black lines show fits to the data as described in the text. **b,** X^o polarization angle ϕ (black data) and degree of linear polarization ρ (red data) for varying excitation polarization angles θ. The blue line shows the linear proportionality $\phi = \theta$.

photon creates neutral excitons in a coherent superposition of each valley state. This stems from the coupling of a linearly polarized photon to the circularly-polarized optical selection rules inherent to both K valleys, as well as the absence of overpowering valley depolarization and decoherence processes. Further, the isotropic response effectively demonstrates our ability to create X^o valley superposition states with any relative phase, θ, between its two valley components (see equation 4.2.1). This represents a significant step in the development of coherent valleytronics and sets the stage for controlling valley pseudospin in a manner analogous to Bloch sphere rotations of electron spin.

4.3 Conclusion

Extending the capability to create and detect valley polarized states, the chapter presents the optical generation of coherent superpositions of valley-separated excitons. In contrast, we find an inability to create coherent superposition states of charged excitons, in agreement with limitations imposed by allowed X^- and X^+ configurations. The fact that the linearly polarized X^o emission orientation

follows that of the excitation denotes the ability to create valley-coherent states with arbitrary phase between the two valley-exciton components. As with the electron spin Bloch sphere and superposition states, this corresponds to the creation of valley superposition states anywhere along the equator of the valley pseudospin Bloch sphere, and sets the stage for future exploration of arbitrary state preparation throughout the valley pseudospin Bloch sphere.

Chapter 5

THE ADDITION OF LAYER PSEUDOSPIN IN BILAYER WSe_2

In this chapter we move from the monolayer system to bilayer WSe_2. With the addition of another layer comes access to another pseudospin index, the layer pseudospin. Using polarization-resolved photoluminescence measurements, we examine the interplay of the three correlated indices of electron spin, valley pseudospin, and layer pseudospin available in multi-layer TMDs. Additionally, we apply electric fields perpendicular to the 2D crystal plane to examine electrostatic manipulation of layer pseudospin and the interplay with electron spin and valley pseudospin. The coupling of layer pseudospin to the electric field enables an enhancement of spin polarization and spectral discrimination of layer-specific trions, with interesting implications for valley superposition states of trions spanning both layers.

5.1 Theory of Coupled Spin, Valley, and Layer Indices

5.1.1 Layer Pseudospin

As outlined in Chapter 2, the presence of time-reversal symmetry and inversion symmetry breaking in monolayer WSe_2 dictates a spin inversion when comparing electronic bands in opposing valleys. With the combination of large spin-orbit coupling from the heavy transition metal atoms splitting the valence bands by 100's of meV and the coupling of opposite light polarization helicities to individual valleys, monolayer TMDs provides direct access to individual valley and spin indices. In bilayer TMDs, the addition of a second layer in AB stacking order breaks the direct correlation between spin orientation and valley index in the system as a whole. For example, the +K valley valence bands are composed of both spin up and spin down hole states, coming from the upper and lower layers, respectively, as depicted in Figure 5.1. This stems from a restoration of inversion symmetry in AB-stacked bilayers [29, 98], which can be confirmed by a lack of second-harmonic generation as shown in the SHG map of Fig. 3.1 [76–78, 99]. For clarity, we explicitly enumerate the relevant, lowest-energy valence band states in terms of their spin, valley and layer occupation.

Table 5.1: Bilayer TMD Quantum Indices

Layer	+K Valley	-K Valley
Upper	$\|\sigma_z = 1, K, \Downarrow\rangle$	$\|\sigma_z = 1 - K, \Uparrow\rangle$
Lower	$\|\sigma_z = -1, K, \Uparrow\rangle$	$\|\sigma_z = -1, -K, \Downarrow\rangle$

In this system effectively comprised of two vertically stacked monolayers, another quantum index associated with layer occupation is introduced - the layer pseudospin. Akin to momentum-separated valleys, electronic bands residing within opposing layers of an AB-stacked bilayer TMD carry opposite spin orientation (see Fig. 5.1). We thus introduce the layer pseudospin to index this sign reversal, which yields three correlated quantum indices $\lambda\sigma_z\tau_z s_z$, where s_z, τ_z, and σ_z denote the spin, valley, and layer indices, respectively, tied together by the strength of the spin-orbit coupling, λ [5]. Bilayer TMDs thus furnish a system in which spin, valley, and layer pseudospin quantum indices may be strongly coupled to one another.

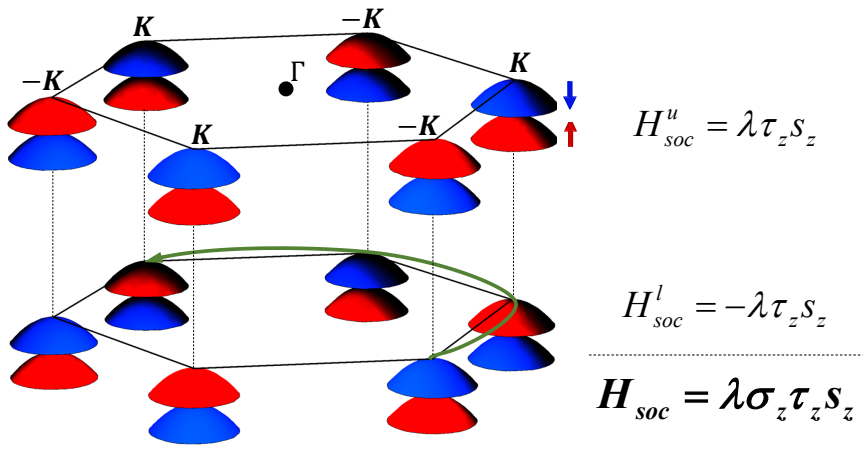

Figure 5.1: Schematic of the uppermost ±K valley valence bands in bilayer TMDs, where blue/red denotes opposite spin orientation. The combination of time-reversal symmetry, inversion symmetry breaking, and AB stacking in TMDs leads to the coupling of three quantum indices - spin (s_z), valley pseudospin (τ_z), and layer pseudospin (σ_z) - in the low energy spin-orbit coupling component of the Hamiltonian.

5.1.2 Interlayer Coupling and Perpendicular Electric Fields

The caveat to the coupling between the three quantum indices of bilayer TMDs lies in the strength of the interactions between the two layers. It is at this point that an excursion must be made to identify the relevance of interlayer coupling in TMDs, with corresponding effects on the robustness of the layer pseudospin index. To elucidate this, we present the effective K-point Hamiltonian of low energy hole states [5]

$$H_v = -\lambda\sigma_z\tau_z s_z + t_\perp\sigma_x \tag{5.1}$$

where the final term is composed of the interlayer hopping strength, $t_\perp$, and the off-diagonal layer pseudospin spinor, σ_x. The relative dominance of the layer-separated and layer-mixing terms is then given by the comparative strengths of λ and $t_\perp$. If $\lambda \gtrless t_\perp$, the uppermost valence bands within each layer and valley remain highly spin-oriented, while if $\lambda \ll t_\perp$ the interlayer hopping effectively mixes the bands of the upper and lower layers, resulting in coupled spin-up and spin-down bands.

The magnitude of the interlayer hopping comes from the wavefunction overlap between opposing layers. At the K-points, the conduction bands are almost entirely composed of d_{z^2} orbitals. The overlap between layers is then given by $\sum_{n=1,2,3} e^{i\mathbf{K}\cdot\mathbf{r}_n}\left\langle d^l_{m=0}(\mathbf{r}_n)\middle|d^u_{m=0}(0)\right\rangle$, where $\mathbf{r}_n$ is the separation between a transition metal atom at $\mathbf{r} = 0$ and the n^{th} neighboring transition metal atom. Here the index n runs over the three nearest neighbors within the opposing layer.

With $\mathbf{K} = \frac{4\pi}{3a}$ (a is the lattice constant) and the three-fold symmetry of the TMD lattice, we have $e^{i\mathbf{K}\cdot\mathbf{r}_1} = 1$, $e^{i\mathbf{K}\cdot\mathbf{r}_2} = e^{-i2\pi/3}$, and $e^{i\mathbf{K}\cdot\mathbf{r}_3} = e^{i2\pi/3}$. The symmetric nature of the $d_{m=0}$ orbitals dictates that $\left\langle d^l_{m=0}(\mathbf{r}_1)\middle|d^u_{m=0}(0)\right\rangle = \left\langle d^l_{m=0}(\mathbf{r}_2)\middle|d^u_{m=0}(0)\right\rangle = \left\langle d^l_{m=0}(\mathbf{r}_3)\middle|d^u_{m=0}(0)\right\rangle$, which gives a conduction band interlayer hopping proportional to $\sum_{n=1,2,3} e^{i\mathbf{K}\cdot\mathbf{r}_n} = 0$. Thus, the only component of interlayer hopping for the conduction bands arises from the small contributions of the d_{xz} and d_{yz} orbitals [25], which at the K-points has a strength of $2t_\perp \approx 0.8$ meV [100]. Note that the much larger magnitude of the spin splitting in the conduction band ($2\lambda_c \approx 40$ meV) serves to suppress this contribution, allowing us to ignore interlayer coupling here.

On the other hand, the overlaps from the valence band $d_{x^2-y^2} \pm id_{xy}$ orbitals are not equivalent. By example, we take the valence band orbital from the upper layer to be $d^u_{m=-2}(\mathbf{r} = 0)$, while $m = +2$ for the three nearest neighbor transition metal atoms of the lower layer. Explicitly, the overlap between the three nearest neighbors are related by $\left\langle d^l_{m=+2}(\mathbf{r}_2)\middle|d^u_{m=-2}(0)\right\rangle =$

$e^{i2\pi/3}\left\langle d^l_{m=+2}(\mathbf{r}_1)\middle|d^u_{m=-2}(0)\right\rangle = e^{i4\pi/3}\left\langle d^l_{m=+2}(\mathbf{r}_3)\middle|d^u_{m=-2}(0)\right\rangle$ and so

$$\sum_{n=1,2,3} e^{i\mathbf{K}\cdot\mathbf{r}_n}\left\langle d^l_{m=+2}(\mathbf{r}_n)\middle|d^u_{m=-2}(0)\right\rangle = 3\left\langle d^l_{m=+2}(\mathbf{r}_1)\middle|d^u_{m=-2}(0)\right\rangle,$$

yielding a finite interlayer hopping, $t_\perp$, in the valence band.

While $t_\perp$ couples bands between the two layers of the bilayer TMD system (within a given valley), we find its importance is further elucidated by examining the perturbed K-point eigenenergies under application of an out-of-plane electric field. This treatment sets the stage for the studies of Section 5.2.2. In the basis of the upper and lower layer conduction and valence band orbitals, $\{\left|d^u_{z^2}\right\rangle, \left|d^l_{z^2}\right\rangle, 1/\sqrt{2}\left(\left|d^u_{x^2-y^2}\right\rangle - i\tau_z\left|d^u_{xy}\right\rangle\right), 1/\sqrt{2}\left(\left|d^l_{x^2-y^2}\right\rangle + i\tau_z\left|d^l_{xy}\right\rangle\right)\}$, we have the Hamiltonian [99]

$$\begin{bmatrix} \Delta - \tau_z s_z \lambda_c + \frac{Ed}{2} & 0 & 0 & 0 \\ 0 & \Delta + \tau_z s_z \lambda_c - \frac{Ed}{2} & 0 & 0 \\ 0 & 0 & -\tau_z s_z \lambda_v + \frac{Ed}{2} & t_\perp \\ 0 & 0 & t_\perp & \tau_z s_z \lambda_v - \frac{Ed}{2} \end{bmatrix} \tag{5.2}$$

with the conduction (valence) band spin-orbit coupling λ_c (λ_v), the monolayer TMD band gap Δ, valley index τ_z, and Pauli spin matrices s_z [25]. Here, "u" and "l" indicate the upper and lower layers, respectively, and following our earlier discussion, the conduction band interlayer hopping has been omitted, while $t_\perp$ gives the strength of the valence band interlayer hopping. Application of a perpendicular electric field induces a potential energy difference, Ed, across the two layers.

The new eigenenergies resulting from the interlayer hopping and applied electric field are then $\Delta + \tau_z s_z \lambda_c \pm \frac{Ed}{2}$ for the lowest conduction bands and $\sqrt{(\lambda_v \pm Ed/2)^2 + |t_\perp|^2}$ for the uppermost valence bands. Even in the absence of electric fields, the finite interlayer hopping results in a shift of the band gap energies when comparing monolayers and bilayers. Due to the coupling between layers, the monolayer band gap, $\Delta - \lambda_c - \lambda_v$, becomes $\Delta - \lambda_c - \sqrt{\lambda_v^2 + |t_\perp|^2}$ in bilayers. The difference, $\sqrt{\lambda_v^2 + |t_\perp|^2} - \lambda_v$ is relatively small in bilayer WSe_2 ($\approx$10 meV) when compared to the 30 meV trion binding energy. Thus, we can expect similar K-valley emission energies for monolayer and bilayer WSe_2, as verified in the PL measurements presented in Figure 5.3a. In contrast, the comparatively smaller spin-orbit coupling in $MoSe_2$ (λ_v = 91 meV) leads to a significant shift of the excitonic emission between monolayers and bilayers [8].

We then turn our attention to the effects of interlayer hopping and applied electric fields on

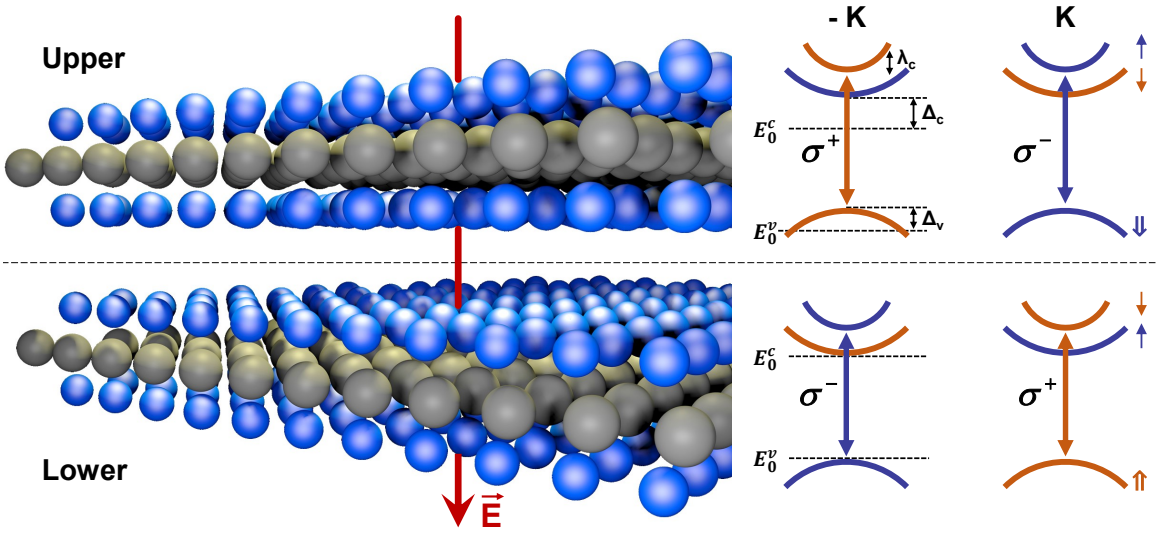

Figure 5.2: Schematic of bilayer WSe_2, its corresponding band structure, and optical selection rules under application of an out-of-plane electric field (red arrow). The band color marks opposite spin orientation (orange and blue arrows), λ_c labels the conduction band splitting, E_0^c and E_0^v indicate the energy levels of the conduction and valence bands within the lower layer, and Δ_c and Δ_v denote the field-induced energy shifts of the conduction and valence bands of the upper layer relative to those of the lower layer.

the emission energy. As evidenced by the electron and hole eigenenergies, application of an electric field perpendicular to the bilayer TMD 2D plane (red arrow in Figure 5.2) will shift the valence band energies more slowly than the conduction bands. Within the conduction bands, the energy separation between the upper and lower layers is directly given by the potential drop, $\Delta_c = Ed$, while in the valence band we have an energy difference of $\Delta_v = \left(\sqrt{(\lambda_v + Ed/2)^2 + |t_\perp|^2} - \sqrt{(\lambda_v - Ed/2)^2 + |t_z|^2}\right) \approx \frac{\lambda_v Ed}{\sqrt{\lambda_v^2 + |t_\perp|^2}}$. Thus, as a result of finite $t_\perp$ in the valence bands, application of electric fields will break the energy degeneracy of the electronic band gap between the upper and lower layers.

Figure 5.2 schematically depicts the relative band gap shift between upper and lower TMD

layers. Here, the uppermost valence bands and the spin-split conduction bands in the ±K valleys are shown for upper and lower layers, where the energy separation between E_0^c and E_0^v gives the electronic band gap in the lower layer. Holding the upper layer at a higher potential induces a shift of conduction and valence bands by Δ_c and Δ_v, respectively, where for bilayer WSe_2 $\Delta_v \approx 0.96\Delta_c$ [99]. Thus, the band gap of the lower layer will lie below that of the upper layer as, $E_0^c - E_0^v < E_0^c - E_0^v + \Delta_c - \Delta_v$.

As mentioned, the relative strength of the spin orbit coupling λ_v and the interlayer hopping $t_\perp$ dictates whether optical fields couple to spin-oriented states or not, and importantly, these values vary significantly among the TMD species. For example, in bilayer MoS_2, $\lambda \approx t_\perp$, such that optical fields do not intrinsically couple to spin-oriented states, though application of external fields can effectively tune layer-layer interactions [101]. In bilayer WSe_2, $\lambda \approx 230$ meV while $t_\perp \approx 70$ meV [5]. We then expect bilayer WSe_2 to meet the condition $\lambda \gg t_\perp$, yield electronic bands which remain highly polarized within each layer, and maintain the coupling of $\sigma^+(\sigma^-)$ polarized optical fields with predominantly spin up (down) hole states at the ±K valleys as depicted in Fig. 5.2b.

In the following sections, we explore the coupling of optical fields to oriented spins in bilayer WSe_2, as well as the effects of applied electric fields.

5.2 Optoelectronic Response in Bilayer WSe_2

In this section we present the optical characteristics of bilayer WSe_2 obtained by white light differential reflectance, photoluminescence, and (low-field) gate-dependent PL measurements.

5.2.1 ±K Valley Optical Properties

Measurements of the low-temperature photoluminescence spectrum of bilayer WSe_2 near 1.75 eV (black curve, Fig. 5.3a) reveal two peaks which, when compared to monolayer WSe_2 emission under identical conditions (blue data), exactly coincide with the $X^o$and X^-emission peaks. The inset to Figure 5.3a shows the differential reflectivity spectrum of bilayer WSe_2, where the sharp derivative feature near 1.7 eV can be assigned to the strong absorption of excitons at the direct-gap of the ±K valleys. The bilayer emission near 1.75 eV can then be assigned to K-valley excitonic recombination. However, the photoluminescence intensity shown here has been multiplied by a

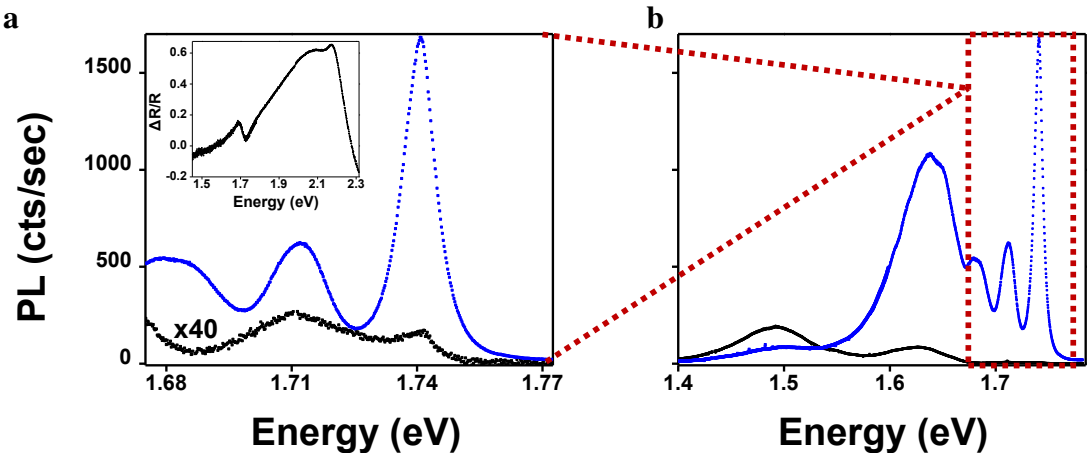

Figure 5.3: **a,** K-point PL spectrum of monolayer (blue) and bilayer (black) WSe_2 under identical conditions. The bilayer intensity has been magnified by a factor of 40 for visibility. Inset: Differential reflectance spectrum of bilayer WSe_2, showing a strong derivative-like feature near 1.7 eV. **b,** Full PL spectrum of monolayer (blue) and bilayer (black) WSe_2, with the bilayer showing significant indirect-gap recombination at lower energies.

factor of 40 to allow comparison on the same scale as the monolayer emission. This much weaker emission intensity is expected for bilayers due to the well-established transformation from a direct to indirect band gap semiconductor with increasing TMD layer number [3, 4, 81]. As shown in Figure 5.3b, emission attributed to the indirect band gap can be seen at ≈1.5 eV, well below ±K valley recombination.

Turning to gate-dependent photoluminescence measurements, we present the spectra obtained near the K valleys for moderate doping levels ($|V_g| \leq 60V$) in Figure 5.4a [99]. We find that, as with monolayer WSe_2, bilayers show electrostatic tunability from electron-doped, to intrinsically doped, to hole-doped regions for applied gate voltages between +60 V to -60 V. The data show an evolution of the emission near 1.7 eV from X^- to X^o and finally to X^+ as we sweep V_g from positive to negative values. The intense peak near 1.6 eV for $|V_g| \approx 0V$ arises from defect state recombination, as in monolayer WSe_2 [9]. Measurement of the gate-dependent differential reflectivity (Fig. 5.4b) shows strong optical response arising from the large oscillator strength of these excitonic transitions at the K-points. Note the absence of any $\Delta R/R$ response from the defect state emission. We thus conclude

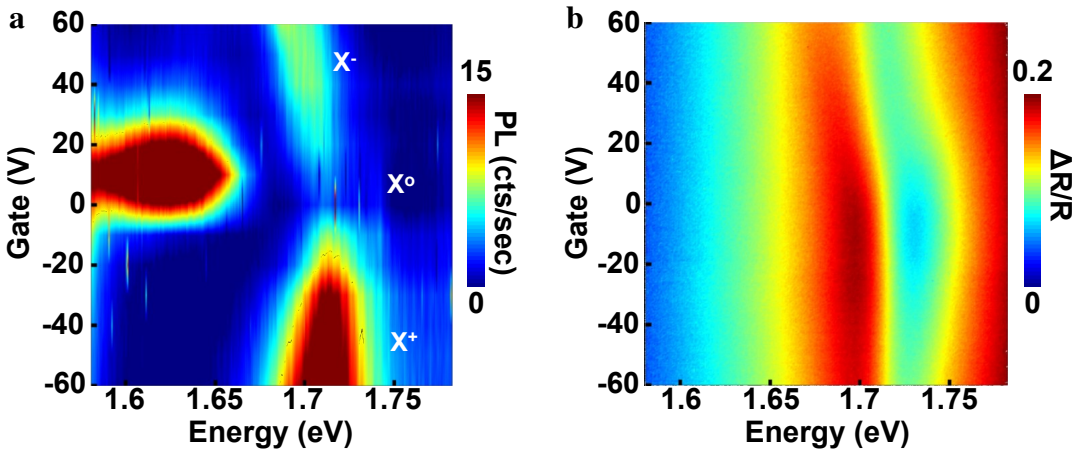

Figure 5.4: **a,** Gate-dependent photoluminescence spectrum of bilayer WSe_2 near the energies of K valley exciton emission. The weak emission near 1.73 eV and $V_g = 0$ V originates from the neutral exciton, X^o, while the emission labeled X^-/X^+corresponds to negatively/positively charged trions. The strong emission near 1.63 eV coincides with defect-state emission observed in monolayer WSe_2. **b,** Differential reflectivity gate map showing strong derivative features aligned with the trion state emission observed in **a**.

that emission observed near 1.7 eV arises from excitonic states akin to those presented earlier in monolayer WSe_2, and now pursue an exploration of the effects of strong electric fields on the spin and pseudospin properties of bilayer WSe_2.

5.2.2 Spectrally Resolving Layer-Specific Emission

As developed in Section 5.1.2, we expect strong out-of-plane electric fields to lead to an energetic splitting between the K valley band gaps of the upper and lower layers. We now present PL measurements of bilayer WSe_2 over an extended gate voltage range of $-100V \leq V_g \leq 150V$. Note that the SiO_2 dielectric layer separating the heavily-doped Si gate from the bilayer WSe_2 device is ≈ 300 nm thick. This means that application of 150 V across the layer corresponds to 0.5 V/nm, which approaches the dielectric breakdown of SiO_2 [102]. Consequently, we only apply these high gate voltages at cryogenic temperatures as doing so at room temperature inevitably led to a breakdown of the insulating SiO_2 dielectric layer.

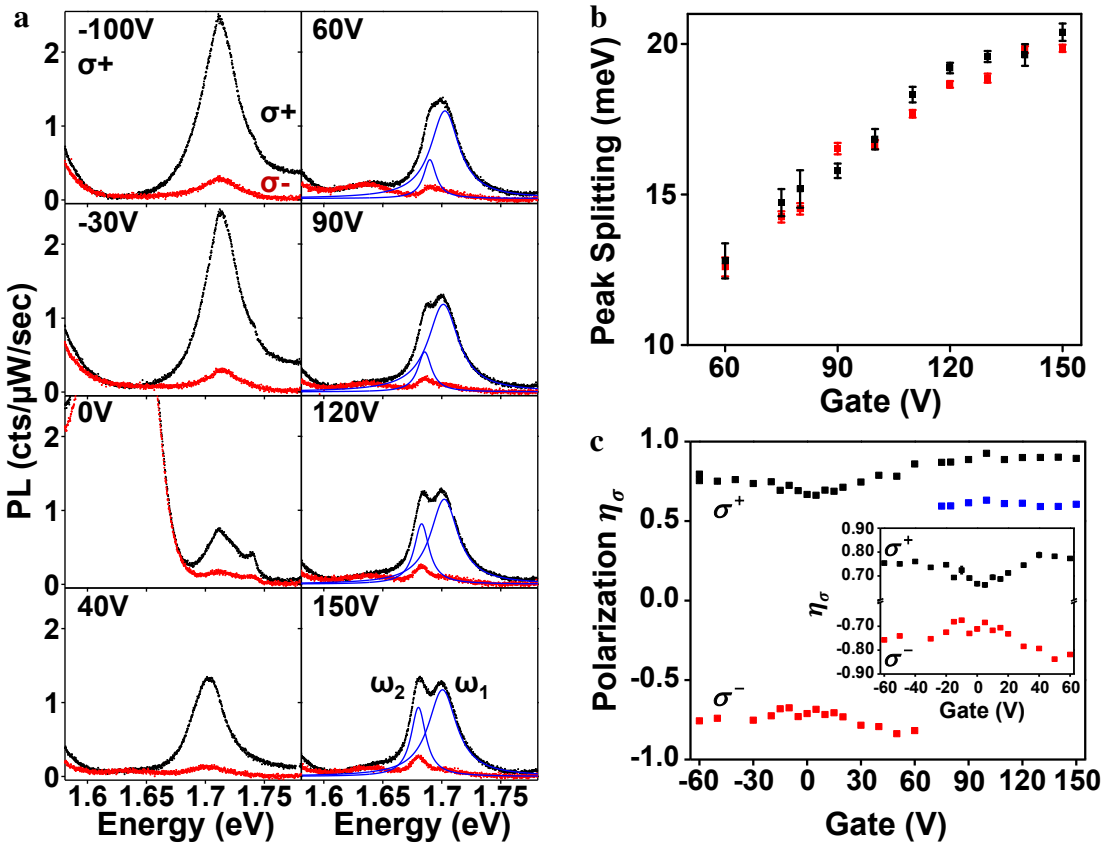

Figure 5.5: **a,** Polarization-resolved PL spectra of bilayer WSe_2 at the energies of K valley exciton emission, for select gate voltages. At large positive gate voltages, X^- splits into a doublet, most easily seen in the co-polarized (black) spectra. We fit the co-polarized X^- doublet with a bi-Lorentzian (blue curves), and label the higher- and lower-energy peaks ω_1 and ω_2, respectively. **b,** Extracted doublet peak splitting, $\omega_1 - \omega_2$, at each gate voltage, for circularly (black) and linear (red) polarized excitation. **c,** Degree of circular polarization, η_σ, of trions for varying gate voltage. For $V_g \geq 60$ V, we resolve the ω_1 and ω_2 emission peaks, whose degree of polarization is given by the black and blue data, respectively. Inset: Zoomed-in plot of η_σ for 60 V $\leq V_g \leq$ 60 V, showing an enhancement of circular polarization for increasing $|V_g|$.

In this section we examine the gate-dependent evolution of only co-polarized PL and save the polarization-dependent studies for the next section. Figure 5.5a presents the progression of the co-polarized PL response (black data) as we vary V_g from -100 V to 150 V. Beyond the tunability between exciton species presented in the former section, we observe that application of large, positive gate voltages causes the negative trion peak to split into a doublet. For $V_g \geq 60$ V, we fit the peak doublet with a bi-Lorentzian, as indicated by the blue curves in corresponding spectra, and label the higher (lower) energy peak as ω_1 (ω_2). The extracted peak separation for both circularly and linearly polarized excitation is shown in Fig. 5.5b, demonstrating a monotonic increase in energy splitting from 13 meV to 20 meV over the voltage range presented.

Uniquely, we find a splitting of the trion peak for positive gate voltages only - the positive trion, X^+, does not split into two. This can be understood in light of the underlying configurations which compose such a trion peak doublet. We schematically represent the allowed trion configurations in Figure 5.6. For the negative trion, the higher emission energy ω_1 originates from interlayer trion states - that is, a photo-excited electron-hole pair in the upper layer with the excess electron in the lower layer (Fig. 5.6a) - while the lower energy peak at ω_2 can be traced to intralayer trions with all quasi-particles in the lower layer (Fig. 5.6b). Additional support for this assignment of trion configurations with their respective emission energies is found in the results of Section 5.4. Though the energy difference between emission from neutral excitons residing in the upper and lower layers can simply be written as $\Delta_c - \Delta_v$, for trions we must also take into account the charging energy. For an intralayer X^-which emits at ω_2, we have a charging energy E_{c2}. Since interlayer negative trions emitting at ω_1 span both layers, their charging energy, E_{c1}, will be comparatively smaller. With a layer separation (7 Å) roughly equivalent to the exciton Bohr radius ($\approx$ 10 Å) [92], the difference $E_{c2} - E_{c1}$ may be as much as a few meV. This then aides in the observation of X^-peak splitting, where the total energy difference is given by $(\Delta_c - \Delta_v) + (E_{c2} - E_{c1})$.

Just the opposite occurs for positive trions, though. While reversing the applied gate voltage switches which layer is held at a higher potential and thus emits at higher energy (ω_1), the electric field-driven increase in conduction band energy, Δ_c, remains larger than that of the valence bands, Δ_v. This results in emission at ω_1 originating from intralayer configurations (see Fig. 5.6c), while the interlayer X^+emits at ω_2 (Fig. 5.6d). Correspondingly, we now have $E_{c1} > E_{c2}$, with an overall X^+energy separation of $(\Delta_c - \Delta_v) - (E_{c1} - E_{c2})$, where the significant magnitude of $(E_{c1} - E_{c2})$

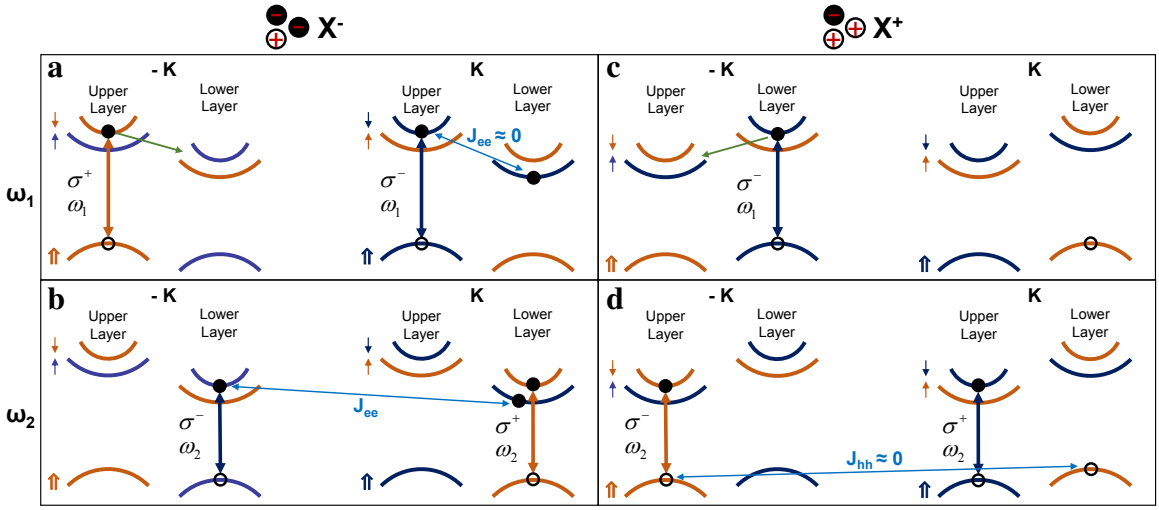

Figure 5.6: X^-configurations which, under an applied electric field, emit at **a,** higher (ω_1) and **b,** lower (ω_2) energies. In both instances, the excess electron resides in the lower layer, whose bands lie at an overall lower energy due to the applied potential. J_{ee} denotes the electron-electron exchange interaction, which is virtually suppressed for interlayer X^-states due the layer separation. X^+configurations which, under an applied electric field, emit at **c,** higher (ω_1) and **d,** lower (ω_2) energies. Here, the excess hole contribution comes from the lower energy valence bands of the upper layer. With the application of negative gate voltages, the electric field reverses direction causing the relative shift between the electronic bands of each layer to switch sign.

obfuscates any X^+peak splitting, in line with our observations (e.g. -100 V spectrum in Fig. 5.5).

Examining just the negative trion states now, we plot the peak energies and widths of ω_1 and ω_2 vs. V_g. In Figure 5.7a, we immediately notice a discrepancy between the peak shifting of ω_2 for increasing gate and the constant energy of ω_1 at $\approx$ 1.7 eV. The decreasing peak energy of ω_2 is consistent with the red-shift observed in monolayer WSe_2, attributed to the quantum-confined Stark effect [9, 103]. We then attribute the constancy of ω_1 as potentially stemming from a cancellation of the quantum-confined Stark effect-induced red shift with the increase in band gap energy caused by the applied electric field. Meanwhile, Figure 5.7 shows the widths of both peaks ω_1 ($\approx$ 30 meV) and ω_2 ($\approx$ 15 meV) to be insensitive to the potential drop across the bilayer.

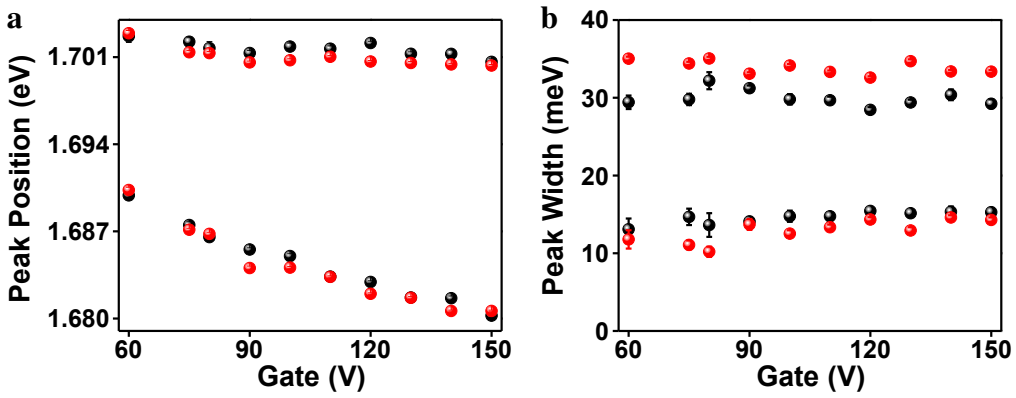

Figure 5.7: **a,** Peak energies of the X^- doublet, where higher (lower) energy data points correspond to emission at ω_1 (ω_2). Black and red data are obtained from peak fittings under circularly and linearly polarized excitation, respectively. **b,** Peak widths extracted from the X^- doublet for circularly (black) and linearly (red) polarized excitation. Larger and smaller peak widths come from emission at ω_1 and ω_2, respectively.

5.3 Enhancing Valley Polarization in Bilayer WSe_2

Now, armed with a better understanding of the trion configurations underlying the observed spectral peaks, we turn to the polarization behavior of bilayer WSe_2. At zero field, trions within bilayer WSe_2 already exhibit a large degree of circular polarization ($\approx 65\%$). As a reminder, the restoration of inversion symmetry in bilayer (vs. monolayer) TMDs signifies that the observed circular polarization does not indicate a net valley polarization, but rather corresponds to a net spin orientation of the excitonic states. Explicitly, σ^+polarized light excites spin down electrons in the -K valley of the upper layer as well as in the +K valley of the lower layer (see Fig. 5.2), and these carriers remain in their respective layers and valleys due to the effective suppression of interlayer hopping by WSe_2's large spin orbit coupling. Our observations of spin polarization are consistent with spin-resolved ARPES studies and first-principles calculations which similarly found the persistence of spin-polarized valence bands within individual layers of an overall centrosymmetric, multilayer crystal [58, 104].

Turning to the effect of an out-of-plane electric field on the observed spin orientation, we exam-

ine the degree of circular polarization, η_σ, at varying gate voltages (see Fig. 5.5c). A comparison of the black and red data show that a reversal of the incident photon polarization helicity from $\sigma^+$to σ^-excites spins of opposite orientation, leading to PL which carries a similar magnitude, but opposite sign, of polarization. The inset to Figure 5.5c shows that closer examination of the magnitude of η_σ reveals an increase in $|\eta_\sigma|$ for increasing $|V_g|$. This can be understood as an effective decoupling of the two layers with increasing electric field, which gradually turns off the interlayer spin relaxation channel. More precisely, an increase in $|Ed|$ effectively suppresses the off-diagonal, layer-coupling component ($t_\perp$) of the Hamiltonian in Equation 5.2. Thus, bilayer WSe_2 offers a system in which spin orientation can be optically created and electro-statically enhanced in the absence of magnetic fields [99].

Figure 5.5c also shows that at high electric fields where X^-splits into a doublet, η_σ continues to increase up to $\approx 90\%$ for emission at ω_1 (black data) while the value for ω_2 (blue data) remains much lower at $\approx 55\%$. Returning again to the band structure schematic of bilayer WSe_2 in an applied electric field, we notice that X^-emission at ω_1 stems from trion states in which the electron-hole pair are located in the upper layer of our depiction (Fig. 5.6a). As the conduction bands within this layer reside at a higher potential than those of the lower layer, intravalley relaxation of photo-excited electrons from the upper to lower layer (indicated by the green arrow) will then contribute to cross-polarized emission at energy ω_2. In comparison, the channel in which electrons move from the lower to the upper layer remains blocked by the large mismatch between the available thermal energy at 30 K (< 3 meV), and the energy splitting, $\Delta_c > 10$ meV (as in Fig. 5.6b). This is clearly evident in the data for $V_g = 150$ V in Figure 5.5a, where the cross-polarized contribution to ω_2 is many times stronger than for ω_1 (red data).

Polarization-resolved PL measurements of bilayer WSe_2 in the regime where V_g splits X^-into a peak doublet then reveal that we can optically create and observe emission coming from distinct layers. Further, the large spin orientation of the split X^-peaks signifies the observation of an all-electrical spin Zeeman splitting, where the once-degenerate energy levels of the spin-oriented excitonic states are spectrally separated according to their layer index.

5.4 Observation and Enhancement of Intervalley Trion Coherence

We now examine optically generated and measured valley-separated coherent superposition states in bilayer WSe_2, similar to the studies presented in Chapter 4 on monolayer WSe_2. With the suppression of interlayer hopping as discussed above, the creation of coherent superpositions of intervalley excitons can be expected, with the distinction that now the superposition states may form within each of the two layers. Referring back to Figure 5.2, such states would correspond to an electron-hole pair in a superposition of the -K and +K valleys in the upper or lower layer. While the orientation of the linearly polarized excitation determines the relative phase between the valley-separated components, we find a reversal of the optical selection rules for the ±K valleys when moving from the upper to the lower layer (c.f. valley indices of σ^+transitions in Fig. 5.2). For linearly polarized excitation of a given orientation, this merely implies a sign inversion of the relative phase, θ, when comparing the superposition state of each layer, and as the individual layers of the bilayer WSe_2 system are largely decoupled ($\lambda > t_\perp$), we expect a persistence of the superposition state with corresponding linearly polarized X^oemission.

The relevant data, labeled "0 V" in Figure 5.8a, do indeed show linearly polarized emission of X^o. Interestingly, the data also show significant linearly polarized emission for trions at all gate voltages. Further, at high gate voltages (e.g. $V_g = 150$ V in Figure 5.8a), the split X^-emission peaks at ω_1 and ω_2 display highly contrasting degrees of linear polarization. This is best visualized in Figure 5.8a, $V_g = 150$ V, where the identical magnitudes of the co- and cross-polarized components of X^-at ω_2 are seen in the overlap of the red data with the ω_2 component of the peak fit (blue line).

Following the work presented in Chapter 4, we examine the degree of anisotropy present in this linearly polarized response. The data shown in Figure 5.8b present the trion peak intensity as the radial magnitude (blue data) at varying linear polarization detection angles (polar angle), for the three excitation polarization orientations shown by the green arrows (c.f. Fig. 4.5). These data verify that the orientation of the linearly polarized emission follows that of the excitation, with a constant degree of polarization, as with measurements in monolayer WSe_2 [9]. This linearly polarized emission then originates from coherent superpositions of valley trions, which stands in contrast to the absence of trion superposition states in monolayer WSe_2.

We return yet again to the trion configuration depictions of Fig. 5.6 to understand how the struc-

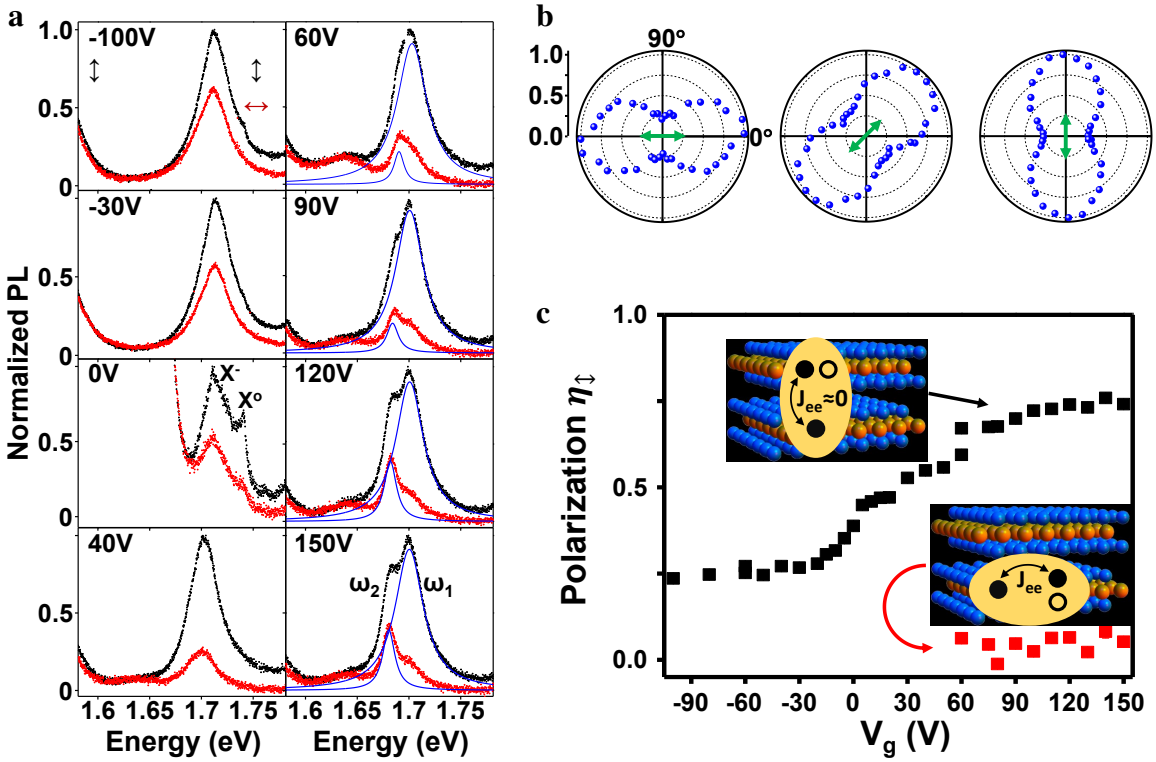

Figure 5.8: **a,** Polarization-resolved PL spectra of K valley emission in bilayer WSe_2 under vertically polarized excitation. Spectra are taken under the applied gate voltage indicated in the upper left corner, with black (red) arrows and data indicating vertical (horizontal) detection polarization. The split X^- peaks at large gate voltages are labeled ω_1 and ω_2 for the higher and lower energy emission, respectively, with the blue curves showing the bi-Lorentzian fit of the co-polarized spectrum. **b,** Trion peak PL intensity (radial magnitude) as a function of the polarization detection angle (polar angle), for three different excitation polarization orientations (indicated by green arrows). Data taken at $V_g = 0$. **c,** Trion peak degree of linear polarization vs. applied gate voltage. For $V_g > 60$ V, X^- splits into two, with the degree of linear polarization of the peak at ω_1 (ω_2) given by the black (red) data. The upper (lower) inset depiction shows that negligible (finite) electron-electron exchange leads to significant (zero) intervalley coherence for interlayer (intralayer) trions.

ture of bilayer WSe_2 makes possible superpositions of valley-separated trions. First, we examine the allowed X^+states. As previously discussed, the lowest energy X^+states include an extra hole from the highest valence bands, i.e. the lower layer in our depiction here. For emission at ω_1, all carriers would come from the same, lower layer (see Fig. 5.6c), and as established in Chapter 4, a valley superposition of X^+states with all carriers in the same layer is strictly forbidden. The linearly polarized contribution must then come from the *inter*-layer X^+configurations depicted in Figure 5.6d. With the addition of another layer, bilayer TMDs now allow for the creation of coherent X^+superposition states since the electron-hole pair can now reside within the layer opposite the excess hole. Additionally, this spatial separation also suppresses hole-hole exchange interactions, enabling the preservation of intervalley coherence throughout the X^+formation and recombination lifetime. This then permits our observation of X^+intervalley coherence shown in Figure 5.8, $V_g = -100$ V.

Similarly, we reach a straightforward explanation for our measurements of disparate valley coherence magnitudes for the ω_1 and ω_2 components of X^-. The absence of intervalley coherence at ω_2, easily seen in the high-field data of Figure 5.8a, stems from the same arguments used in the case of monolayer WSe_2 [9]. Namely, all carriers are localized within the same (e.g. lower) layer as in Figure 5.6b. They are thus expressly forbidden from forming a coherent superposition state, or, for those configurations which are allowed, the trion experiences valley-asymmetric electron-electron exchange interactions, J_{ee}, which introduce decoherence. We schematically illustrate this in the lower inset of Fig 5.8c, where finite J_{ee} is indicated.

As with X^+, the successful creation of X^-valley superposition states at emission energy ω_1 comes only from excitation of the interlayer trion configurations depicted in Figure 5.6a. Similar to the X^+configurations of Figure 5.6d, the excess carrier resides in the layer opposite the electon-hole pair, which separation quells the exchange interaction, J_{ee}, and allows for the preservation of intervalley coherence during the X^-lifetime. This is depicted in the upper inset diagram to Figure 5.8c, where X^-spans both layers and $J_{ee} \approx 0$.

We show the magnitude of the linear polarization extracted by fitting the spectra at each gate voltage in Figure 5.8c. At large gate voltages, we resolve the split X^-emission and present the degree of valley coherence at ω_1 (black) and ω_2 (red). The increase in the degree of X^-linear polarization at ω_1 can be understood as resulting from an electric field-induced decrease in layer-layer coupling, with a concomitant reduction of J_{ee}. In contrast, the null value of $\eta_\updownarrow$ for X^-at ω_2

agrees with the absence of valley coherence seen for X^- in monolayer WSe_2 at all gate voltages (c.f. Fig. 4.4). In the hole doping regime, the flat response seen here for $V_g < 0$ V indicates that for the interlayer X^+ configurations, J_{hh} interactions across both layers may be heavily suppressed, such that the degree of valley coherence of X^+ states at ω_2 does not improve as the applied field increases and further decouples the two layers.

With this understanding of our polarized PL measurements, we have now established the first observations of optically-created inter-valley coherence for both negatively and positively charged excitons. These results are made possible in bilayer WSe_2 due to allowed interlayer trion configurations and a weak layer-layer coupling.

5.5 Conclusion

In this chapter we have shown that the intrinsically suppressed interlayer hopping found in bilayer WSe_2 allows for optical preparation of oriented spin states, as well as another system in which coherent superpositions of valley-separated excitons is made possible. The addition of the layer pseudospin offers facile electrostatic manipulation of its coupled spin and valley pseudospin indices, as developed theoretically. Subsequently, the structure of bilayer WSe_2 offers the ability to spectrally differentiate interlayer and intralayer trion species, electrostatically tune the net spin orientation, and create coherent superpositions of interlayer trions.

Chapter 6

TRION-TO-EXCITON ENERGY UP-CONVERSION AND MULTI-VALLEY TRIONS IN MONOLAYER WSe_2

In this chapter we develop a more thorough understanding of the PL peaks observed in monolayer WSe_2 near the emission energy of the negative trion and with application of positive gate voltages. We first propose a model of state hybridization between the neutral exciton and trion polarons. This model provides a framework for, and agrees with, the experimental evidence obtained by a variety of fluorescence excitation and detection schemes. In Section 6.2.1 we perform resonant fluorescence measurements which elucidate strong phonon-exciton interactions and indicate a peak doublet within the X^- emission. We then pursue an investigation of the X^- doublet valley polarization and its temperature-dependence in Section 6.2.2. While manipulation of the electrostatic gate in the PL studies of Section 6.2.3 supports the level hybridization picture proposed in the first section, the strongest evidence of the hybridized exciton/trion-polaron model comes from the reverse-PL polarization, temperature, and gate-dependent measurements of Section 6.2.4. Finally, this Chapter's final section provides an understanding of the other trion state, $X^{-\prime}$, first seen in the PL spectra of Section 3.2.2, and outlines evidence of its formation due to the multi-valley band structure of ultra-thin TMDs.

6.1 Hybridized Exciton and Trion-Polaron Model

In this section, we introduce a model of hybridization between neutral excitons and phonon-dressed charged excitons (i.e. trion-polarons), which agrees well with our optical studies of two nearly-degenerate emission peaks at the X^- energy. Inherent to the model are assumptions of 1) near energy degeneracy of the neutral exciton, X^o, and phonon-dressed negative trion (X^-) states, and 2) strong quasiparticle interactions. The second assumption, enhanced quasiparticle interactions in 2D materials, naturally comes from the reduced dielectric screening inherent to 2D semiconductors in which the membrane thickness and effective interaction radii are comparable, which has been well-

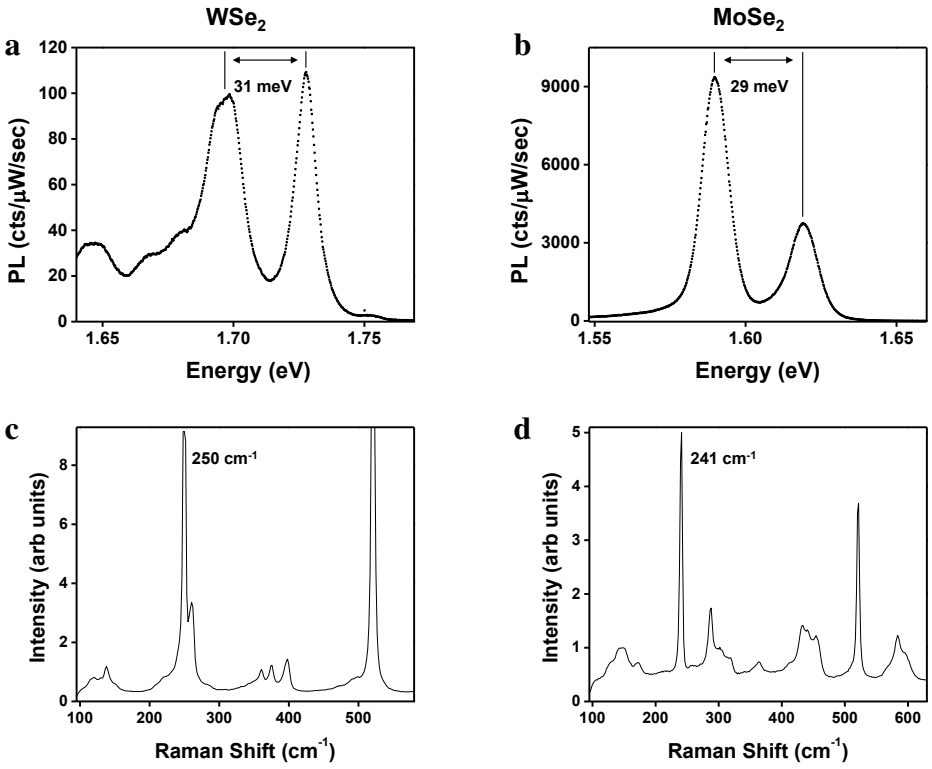

Figure 6.1: PL spectra of monolayer **a,** WSe_2 and **b,** $MoSe_2$. Approximate trion charging energies are indicated. Raman spectra of monolayer **c,** WSe_2 and **d,** $MoSe_2$. The peak position of the strongest Raman emission is indicated (note the peak at 520 cm^{-1} comes from the Si substrate). The PL spectra are measured at a sample temperature of 30 K, while the Raman spectra are taken in ambient conditions.

established both theoretically [32, 60, 105, 106] and experimentally [36, 39, 82, 107]. Regarding our first assumption, we find support for the energy degeneracy of excitons and a trion plus a phonon by comparing the trion charging energy with the crystal phonon energies. Figures 6.1a,b present the low-temperature PL spectra of monolayer WSe_2 and $MoSe_2$, with trion charging energies of 31 meV [9] and 30 meV [8], respectively. In the Raman spectra of Figures 6.1c,d, we find dominant scattering wavenumbers of 250 cm^{-1} = 31 meV and 241 cm^{-1} = 30 meV for WSe_2 and $MoSe_2$, respectively [108–111]. The near equivalence of the optically active phonon modes and trion charging energies then supports the assumption of nearly-degenerate neutral exciton and phonon-dressed

trion states.

Interestingly, preliminary measurements indicate that the correlation between trion charging energies and dominant phonon energies may also extend to the monolayer TMDs MoS_2 and WS_2. Unfortunately, accurate determination of the trion emission energy remains difficult due to the broad spectral peaks characteristic of the sulfur-series TMDs, while the literature offers a large variation in reported charging energies; 30 - 45 meV in monolayer WS_2 [36, 38, 112, 113] and 18 - 67 meV in monolayer MoS_2 [41, 88, 114–121].

For the selenium-based TMDs WSe_2 and $MoSe_2$, the coincidence revealed here is unmistakeable. In order for the formation of a trion-polaron to be stable, the bound state must lie at a lower energy than the total of its constituents (i.e. X^-+ phonon). Thus, equivalent phonon and trion charging energies would dictate that the trion-polaron state must lie below the neutral exciton. In our model, we assume such an ordering.

With such a small energy separation between the neutral exciton and trion-polaron, we propose a hybridization scheme which results in the new eigenstates $|1\rangle$ and $|2\rangle$. Figure 6.2 presents a diagram of the relevant energy levels, with the un-hybridized X^o and X^-+ phonon states shown in gray, and the hybrid states $|1\rangle = \sqrt{1-\delta}|X^-\rangle \otimes |n\rangle + \sqrt{\delta}|e, X^o\rangle \otimes |n-1\rangle$ and $|2\rangle = \sqrt{1-\delta}|e, X^o\rangle \otimes |n-1\rangle + \sqrt{\delta}|X^-\rangle \otimes |n\rangle$ in black. Here, e denotes a free (unbound) electron, and n the total number of phonons. For significant detuning of the underlying states, we have $\delta \ll 1$, yielding a weak hybridization such that the contribution of $|e, X^o\rangle \otimes |n-1\rangle$ to $|1\rangle$ (and $|X^-\rangle \otimes |n\rangle$ to $|2\rangle$) is only a small perturbation. Thus, we can still largely consider $|2\rangle$ as a neutral exciton and $|1\rangle$ as a negative trion-polaron. Still, the finite hybrization remains important as it facilitates conversion between $|1\rangle$ and $|2\rangle$, as we find to be important in the next section.

The relevant ground states here are $|e\rangle \otimes |n\rangle$ and $|e\rangle \otimes |n-1\rangle$ which differ in total phonon number by one. Transitions from the excited states $|2\rangle$ and $|1\rangle$ then occur at energies near X^o and X^-, respectively. In the detuned limit, the strength of these transitions can vary strongly depending on the excitonic optical oscillator strength and the mismatch in phonon number. Figure 6.2 indicates the relative transition strengths by the thickness of the dashed lines. For example, the dominant transition to $|e\rangle \otimes |n-1\rangle$ comes from $|2\rangle$ (thick dashed line labeled Γ_2^o) due to a combination of the overwhelming oscillator strength of the neutral exciton (see Figure 6.16c) and conservation of phonon number (recall $\delta \ll 1$). Conversely, transitions between $|1\rangle$ and the $|e\rangle \otimes |n-1\rangle$ ground state

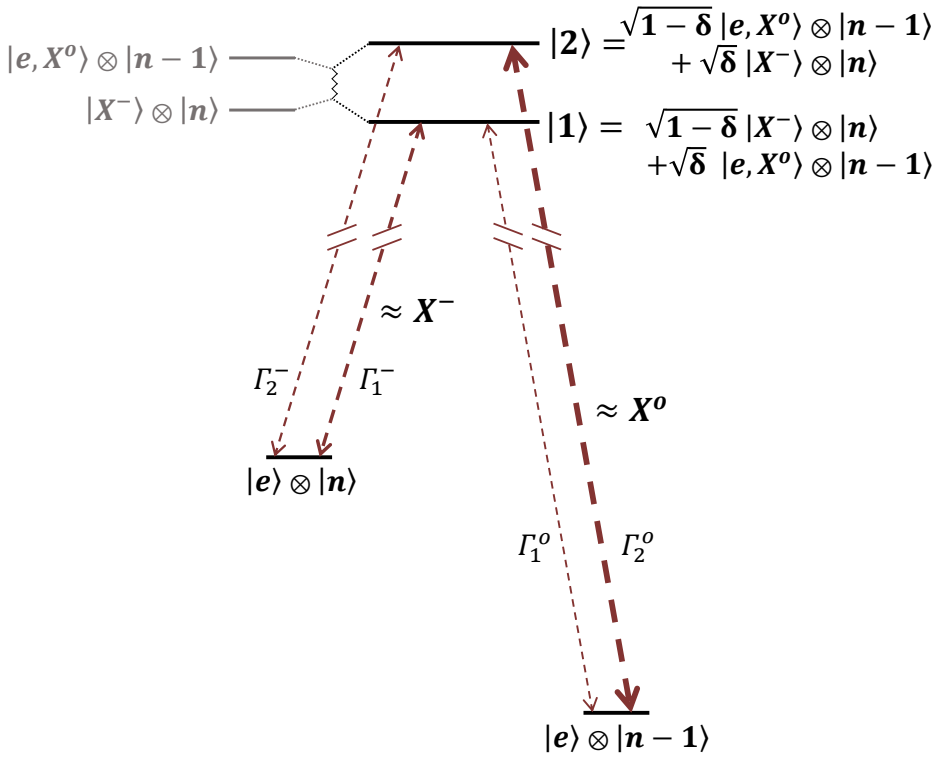

Figure 6.2: Energy level diagram depicting a hybridization of neutral excitons, X^o, with phonon-dressed trions, $|X^-\rangle \otimes |n\rangle$, shown in gray. Here e denotes a free electron and n the phonon number. The resulting hybrid states $|1\rangle$ and $|2\rangle$ carry contributions from each of these states, but for $\delta \ll 1$ (weak hybridization), each is still predominantly composed of either $|X^-\rangle \otimes |n\rangle$ or $|e, X^o\rangle \otimes |n-1\rangle$. Relaxation to the two ground states $|e\rangle \otimes |n\rangle$ and $|e\rangle \otimes |n-1\rangle$, which differ in energy by one phonon, then occurs at energies near X^- and X^o, respectively. The relative strength of these radiative transitions is denoted by the thickness of the dashed lines, with $\Gamma_2^o \gg \Gamma_1^o$ for $\delta \ll 1$ (see text for explanation).

require emission of a phonon, and are predominantly composed of charged excitons which possess an oscillator strength nearly an order of magnitude lower than neutral excitons. Thus the transition Γ_1^o occurs with much lower probability.

We find that such a large disparity in transition strengths may not occur for the $|e\rangle \otimes |n\rangle$ ground state. Though Γ_1^- largely conserves phonon number while Γ_2^- does not, the much larger oscillator strength of the predominantly $X^o|2\rangle$-state will increase Γ_2^-. As the spectra of Section 6.2.3 show, comparable intensities of the emission peaks at X^-indicate similar strengths of Γ_1^- and Γ_2^-, which we incorporate into our model. Of course, if the energy difference between $|e, X^o\rangle \otimes |n-1\rangle$ and $|X^-\rangle \otimes |n\rangle$ can be reduced while keeping the phonon energy fixed, the degree of hybridization will increase toward $\delta = 1/2$ and the disparity between the relative strengths of the radiative transitions (e.g. Γ_1^- vs. Γ_2^-) will diminish.

Before proceeding, we briefly note the difference between our model of exciton/trion-polaron hybridization, and that of X^opolaron formation from the viewpoint of phonon scattering found in Reference [122].

6.2 Exciton-Phonon Interactions, X^- Fine Structure, and Photon Up-Conversion

With this model of the neutral and charged exciton energy levels of monolayer WSe_2 in mind, we now examine the supporting experimental results from a variety of flourescence experiments. We find distinct signatures indicative of correlations between neutral excitons, charged excitons, and phonons, which agree with the proposed energy level diagram.

6.2.1 Signatures in Resonant Fluorescence

The initial signatures of strong correlations between phonons and the neutral and charged excitonic states come from resonant fluorescence measurements. This measurement technique differs from conventional photoluminescence in that it allows for spectral readout at energies surrounding the excitation laser. In order to accomplish this without damagie to sensitive CCDs, strict polarization selectivity must be employed on the luminescent output. For this, we create a high fidelity of polarization in the incident laser using a Glan-laser polarizer. Note it is often best to accurately orient this polarization axis along one of the principal axes (s- or p-polarization) of the optics following

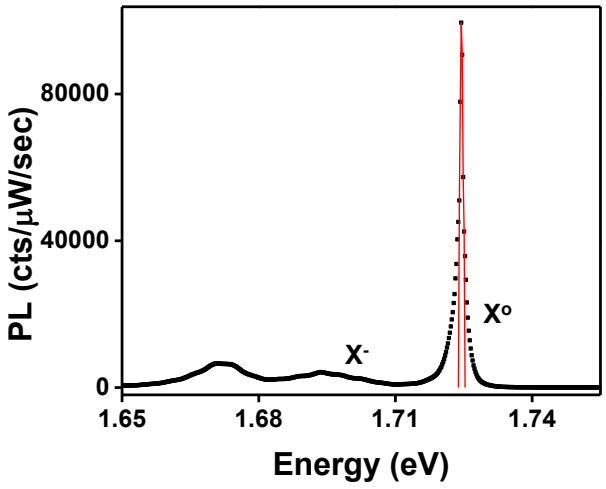

Figure 6.3: Resonant fluorescence spectrum of monolayer WSe_2 at 30 K for 40 μW of 1.724eV excitation and 10 sec integration time. The measured width of the laser line is limited by the spectral resolution of the spectrometer configuration. The X^o emission is strongly enhanced around the excitation energy, with notable X^- emission as well.

the polarizer to avoid a shift to elliptical polarization [97]. The beam reflects off of a wedged beamsplitter to avoid parasitic interface reflections, after which it focuses onto the WSe_2 monolayer via a polarization-maintaining objective. We analyze the reflected beam and emitted fluorescence transmitted through the beamsplitter. On this detection side, we achieve nearly perfect extinction of the excitation beam through a combination of a quarter wave-plate, half wave-plate, and high-extinction linear polarizer. The half wave-plate orients the emitted laser polarization perpendicular to the polarizer transmission axis. The quarter wave-plate operates at small relative angles between the crystal fast axis and the laser polarization, eliminating the slight ellipticity present in the reflected laser beam caused by imperfect optical surfaces, the focusing objective, and reflections from the substrate. After passing through the polarizer, the light is then focused into a single-mode optical fiber, which not only suppresses stray laser light due to the small entrance aperture, but carries the benefit of being a 'coherent detector' where the overlap integral of the light field *amplitude* can largely cancel remnant laser contributions in this cross-polarized detection scheme [123–125].

Nearly perfect extinction of the excitation beam is then accomplished in two stages. First, we

orient the detection polarizer roughly perpendicular to the excitation polarization and shine the output of the optical fiber onto a photodiode/power meter with sensitivity of ≈ 50 nW. Fine adjustment of the polarizer orientation (only) should achieve a null reading on the photodiode. The fiber output is then sent into the spectrometer and read by a high quantum-efficiency CCD. We achieve further attenuation of the remnant laser light through iterative adjustments of the half wave-plate and quarter wave-plate to reduce the laser emission line. To achieve high extinction ratios, the microscope objective position must be positioned to provide an optimal focus on the sample surface. Care must also be taken to eliminate movement or vibration of the sample surface as these instabilities lead to increased 'leakage' of the laser light through the detection polarizer and fiber.

Following these techniques, we present an example of a resonant fluorescence spectrum of monolayer WSe_2 at 30 K in Figure 6.3. The spectrum demonstrates the high degree of polarization extinction obtained in our apparatus as evidenced by the comparable amplitude of the luminescence (broad peaks) and transmitted laser intensity (sharp, red peak at 1.724 eV). In our measurements, the width of the laser line from an MSquared SolsTiS appears much broader (0.3 nm = 0.7 meV) than the true spectral width (10^{-7} nm = 0.2 neV), due to the spectrometer entrance slit width and overall resolution. Since the laser wavelength of Figure 6.3 overlaps part of the X^o peak, we find a resonant enhancement of the neutral exciton emission around the excitation (red line), in addition to significant trion emission near 1.695 eV. The peak near 1.67 eV emerges with a redshift from X^o consistent with the $X^{-\prime}$ peak seen in Figure 3.4 and discussed later in this chapter.

With the resonant fluorescence technique established, we perform scanning-wavelength measurements where we monitor the emission of monolayer WSe_2 as the excitation sweeps over the observed excitonic peaks seen in standard PL spectra. Throughout these measurements, we take caution to scan the laser in small steps since the high polarization extinction initially achieved rapidly deteriorates with modification of the excitation wavelength due to the wavelength-dependent response of the wave-plates and other optical elements. For small (few nm) changes, the increased laser transmission often still lies below the CCD damage threshold, and can be readily extinguished via feedback from the CCD reading.

After optimization of the polarization rejection at each excitation wavelength, we arrive at the 2D resonant fluorescence map presented in Figure 6.4a. The point-like features located where excitation energy equals emission energy come from the small portion of laser light that makes it through the

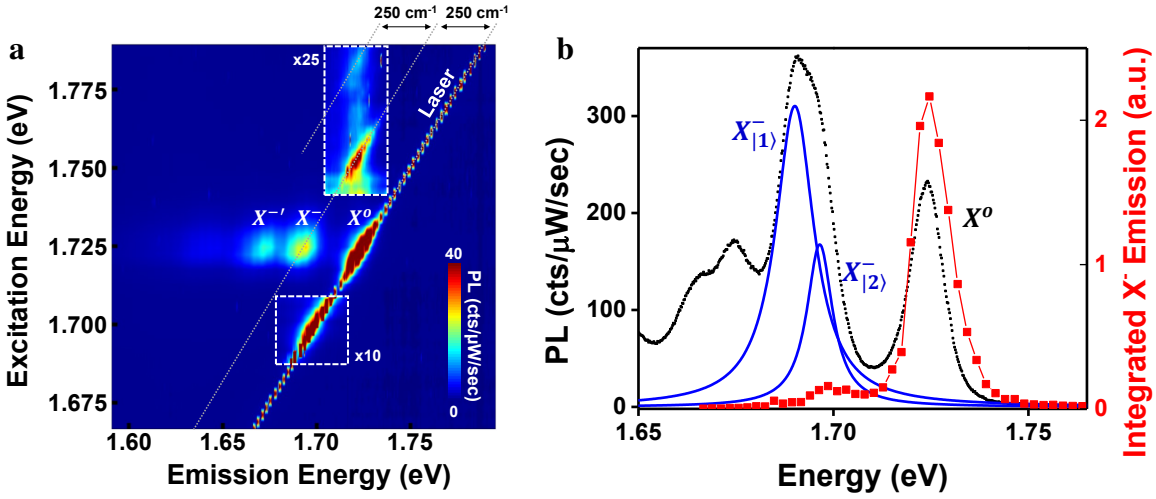

Figure 6.4: **a,** 2D resonant fluorescence map of monolayer WSe_2. A constant readout window is maintained while the excitation sweeps from 1.667 eV to 1.789 eV. The line of sharp points where excitation equals emission comes from remnant laser light. The dotted lines indicate emission lying one and two 250 cm^{-1} phonons below excitation. The zoomed-in regions surrounded by the white dashed lines elucidate the excitonic response of the monolayer for significant detuning of the excitation from X^o. The upper box has the color scale magnified by a factor of 25 to show the response at X^o emission energies for blue-detuned excitation, while the lower box magnifies the response around resonantly-excited X^- energies by a factor of 10. **b,** Photoluminescence spectrum under 2.33 eV excitation (black data). The blue lines show a bi-Lorentzian fit to the X^- peak, with peaks labeled as $X^-_{|2\rangle}$ and $X^-_{|1\rangle}$ for the higher and lower energy peaks, respectively. The red data show the integrated luminescence intensity for the trion emission energy range 1.679 eV - 1.710 eV, while the horizontal axis indicates the excitation energy. In addition to the strong peak when pumping X^o, a secondary peak emerges for excitation at $X^-_{|2\rangle}$.

polarizers and optical fiber. When resonantly exciting the neutral exciton, we find strong emission at energies characteristic of X^o, X^-, and $X^{-\prime}$as labeled. The boxes enclosed by the white dashed lines show regions where the color scale has been magnified by the indicated factor to elucidate the behavior of small signals. The dotted, diagonal lines with a slope of one indicate an energy shift of one and two phonons from the excitation, with the labeled energy separation of "250 cm^{-1}" (cf. Raman spectrum in Figure 6.1c).

Interestingly, the uppermost box with a zoom of 25x shows resonantly-enhanced X^oemission when pumping at energies of X^o+ 250 cm^{-1} and X^o+ 500 cm^{-1}, pointing to strong exciton-phonon interactions [126]. Note also for 1.725 eV excitation the overlap of the X^-peak with the line denoting a 250 cm^{-1} shift from the excitation and X^o. In contrast to this X^-emission at $\approx$ 1.69 eV, we find in the lower box (with a zoom of 10x) that maximum trion emission occurs for excitation and detection at $\approx$ 1.70 eV. This shift is clearly visualized in Figure 6.4b. Here, the integrated intensity of the data in Figure 6.4a for emission energies 1.679 eV - 1.710 eV (red) is overlaid with a 2.33 eV excitation PL spectrum (black). The strongest peak in the red data occurs when resonantly exciting X^o, indicating efficient exciton-to-trion conversion. A secondary peak in the red data emerges near 1.70 eV, on the high-energy side of the PL-spectrum X^-emission.

Examination of the PL spectrum also reveals an X^-peak which more closely resembles a peak doublet rather than a single Gaussian or Lorentzian shape, consistent with the spectrum of Figure 6.1a. We attribute our ability to resolve the dual-peak structure of $X^-$to cleaner mechanical exfoliation and lithography techniques implemented since the measurements presented in Chapters 4 and 5. Returning to our model presented in Section 6.1, we find this dual peak structure to be consistent with the two distinct emission energies expected at the trion energy for transitions Γ_2^- and Γ_1^-. We thus label these peak as $X^-_{|2\rangle}$and $X^-_{|1\rangle}$, respectively and as discussed earlier, find similar peak intensities.

The following sections now focus on understanding the behavior of $X^-_{|1\rangle}$and $X^-_{|2\rangle}$by examining their valley polarization and energy splitting at varying temperatures, as well as by performing gate-dependent PL studies with the X^-doublet resolved.

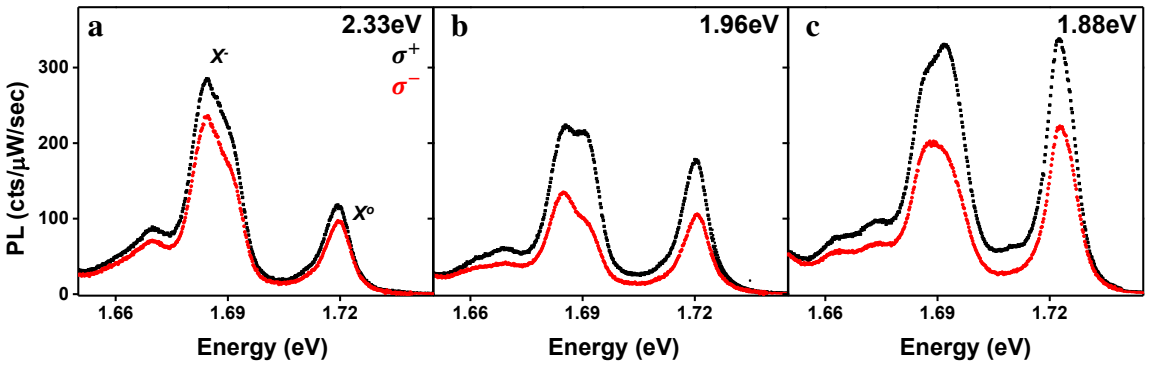

Figure 6.5: Polarization-resolved PL spectra for σ^+excitation at **a,** 2.33 eV, **b,** 1.96 eV, and **c,** 1.88 eV. Black and red data show $\sigma^+$and σ^-detection polarizations, respectively. Note the differing degrees of valley polarization on the high- and low-energy sides of X^-.

6.2.2 Valley Polarization of the Split X^-

As a first step in the characterization of the $X^-_{|1\rangle}$and $X^-_{|2\rangle}$peaks, we study the valley polarization of the X^-doublet by exciting with circularly polarized light and detecting the co- and cross-circularly polarized components of the emission (as in Section 4.1). In Figure 6.5a-c, we present the polarization-resolved PL spectra for excitation energies of 2.33 eV, 1.96 eV, and 1.88 eV. With the $X^-_{|1\rangle}$and $X^-_{|2\rangle}$peaks now distinguishable, we note two behaviors not previously revealed. First, as the excitation energy decreases, the emission intensity of $X^-_{|2\rangle}$relative to $X^-_{|1\rangle}$increases, as does the intensity of X^orelative to X^-. Second, the degree of polarization for $X^-_{|2\rangle}$is noticeably higher than for $X^-_{|1\rangle}$(c.f. the high- and low-energy components of X^-emission for 1.96 eV excitation). The correlation between $X^o$and $X^-_{|2\rangle}$emission intensities for varying laser energies agrees with our model proposed earlier in the chapter where both emission lines originate from state $|2\rangle$.

The disparate degrees of valley polarization between $X^-_{|1\rangle}$and $X^-_{|2\rangle}$may also indicate significantly different lifetimes for $|1\rangle$ and $|2\rangle$. This hypothesis aligns well with our model as well as time-resolved PL measurements of monolayer WSe_2. In our model, $X^-_{|2\rangle}$originates from state $|2\rangle$ which is predominantly neutral exciton-like and lies at higher energy than the mostly trion-polaron $|1\rangle$ state involved in $X^-_{|1\rangle}$emission. As level hybridization couples $|1\rangle$ and $|2\rangle$, efficient non-radiative emptying

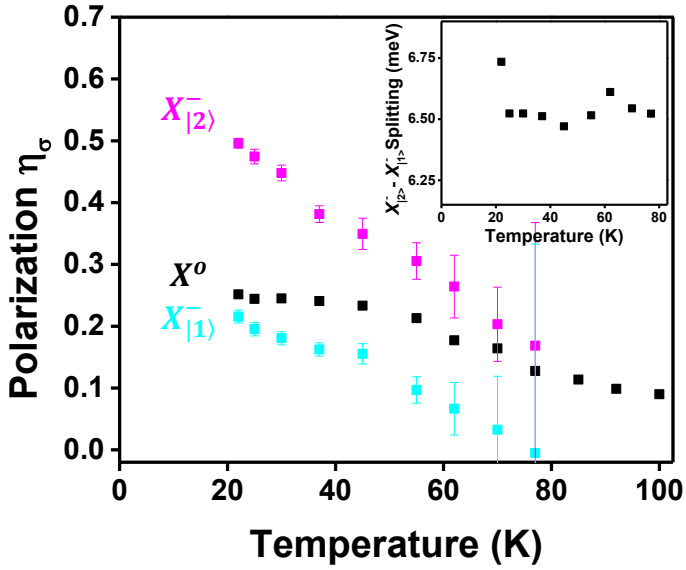

Figure 6.6: Temperature dependent valley polarization, η_σ, of X^o, $X^-_{|2\rangle}$, and $X^-_{|1\rangle}$. Inset: $X^-_{|2\rangle}$-$X^-_{|1\rangle}$peak splitting vs. temperature. Data for $X^-_{|1\rangle}$and $X^-_{|2\rangle}$not shown for temperatures above 80 K due to unreliable fitting caused by weakening and broadening of the peaks. Error bars indicate the standard deviation obtained from the peak fits, which are too small to see in the inset.

of $|2\rangle$ (to e.g. $|1\rangle$) may be expected. Regardless of the mechanism and final state, the measurements of Wang *et al.* in monolayer WSe_2 find a measured X^oluminescence decay time nearly an order of magnitude shorter than the fastest trion decay time, pointing to an ultra-fast emptying of the neutral exciton state [66]. Additionally, they observed two distinct timescales for the decay of trion valley polarization: $\approx$ 10 ps and $\approx$ 1 ns. Thus, the more highly polarized trion states decay orders of magnitude more quickly than those with less-robust valley polarization. Again, this coincides with our model and observations of stronger valley polarization at $X^-_{|2\rangle}$than $X^-_{|1\rangle}$. Since the short radiative lifetime of the neutral exciton state provides fewer opportunities for intervalley scattering, a stronger valley polarization for emisison from neutral exciton-like states (e.g. $|2\rangle$ state emission at $X^-_{|2\rangle}$) is reasonable. Future time-resolved PL measurements which resolve the time dynamics of both $X^-_{|1\rangle}$and $X^-_{|2\rangle}$states individually should provide more definitive conclusions on this matter.

We also perform temperature dependence measurements of valley polarization. We fit the

X^- emission with a summation of two Lorentzian peaks, (see e.g. Figure 6.4b) for each detection polarization, and extract the degree of polarization, η_σ, for the peaks X^o, $X^-_{|1\rangle}$, and $X^-_{|2\rangle}$ as a function of temperature. From the data shown in Figure 6.6 we find a monotonic decrease in η_σ with increasing temperature as can be expected with phonon-activated intervalley scattering processes [9]. Data for $X^-_{|2\rangle}$ and $X^-_{|1\rangle}$ do not extend beyond 80 K due to inaccurate peak fits caused by a broadening and amplitude reduction of both peaks with increasing temperature. The data immediately show values of η_σ for $X^-_{|2\rangle}$ more than double those of $X^-_{|1\rangle}$ at all temperatures. η_σ for $X^-_{|2\rangle}$ also remains greater than the valley polarization of X^o for the temperature regime explored here. While the disparity between valley polarizations of $X^-_{|2\rangle}$ and $X^-_{|1\rangle}$ may be linked to contrasting state lifetimes as discussed above, the reduced η_σ of X^o relative to $X^-_{|2\rangle}$ is counter-intuitive, though potentially connected to an interplay of exciton exchange [70] and helicity-dependent phonon modes [127].

From the peak fits we also extract the magnitude of the $X^-_{|2\rangle}$-$X^-_{|1\rangle}$ peak splitting at each temperature (see Figure 6.6 inset). From this we find a constant peak separation of 6.55 ± 0.08 meV. This corresponds to a temperature of 76 ± 1 K, which we show to be significant in Section 6.2.4.

6.2.3 X^- Doublet Gate Dependence

In this section we aim to investigate regimes of differing strengths of exciton/trion-polaron hybridization, δ, through gate-dependent PL measurements of the split X^- states.

For the measurements presented in this section only, we study a WSe_2 FET created by transferring a WSe_2 monolayer onto an insulating hexagonal boron nitride (h-BN) sheet ≈ 15 nm thick using the PMMA transfer method of Reference [128]. The h-BN is located on top of a Pd backgate as with the devices of Reference [17]. Electrical contacts to the monolayer on top of the h-BN are then patterned. Compared to a 300 nm SiO_2 dielectric on a highly-doped Si wafer surface, the much thinner h-BN dielectric separating the monolayer from the Pd gate offers an atomically-smooth substrate [129] and significantly enhances electrostatic doping, requiring much smaller applied voltages to achieve the same doping levels presented in Figure 3.4.

A typical spectrum near intrinsic doping levels shows X^o emission along with a split X^- peak (Figure 6.7). We find that compared to SiO_2-supported crystals, the spectra from WSe_2 monolayers on a h-BN substrate typically display a redshift of ≈ 30 meV. This shift likely stems from the

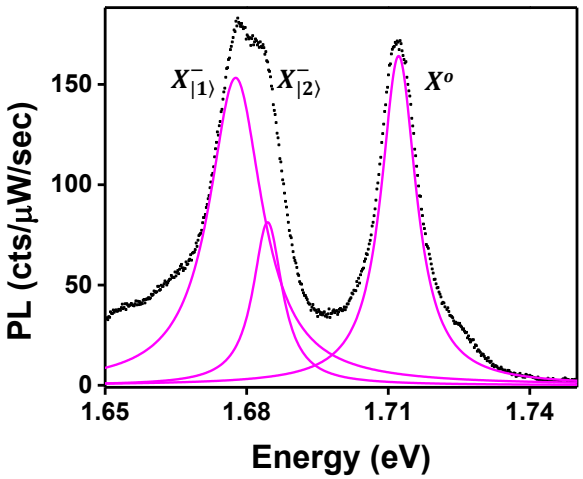

Figure 6.7: Typical PL spectrum of BN-supported monolayer WSe_2 for 1.96 eV excitation and near intrinsic doping levels (black data). A triple Lorentzian fit to the X^o and X^- peaks is shown in magenta.

different dielectric environment and/or a slightly higher sample temperature, with its magnitude comparable to other studies [41]. We fit the spectrum with a sum of Lorentzians for the X^o, $X^-_{|2\rangle}$, and $X^-_{|1\rangle}$ peaks, as shown by the magenta curves. As shown here, we find that across many samples, $X^-_{|2\rangle}$ consistently exhibits a lower spectral weight than $X^-_{|1\rangle}$, which qualitatively agrees with the somewhat stronger transition strength of Γ^-_1 vs. Γ^-_2 in our model.

By monitoring the PL response and fitting the emission peaks as we sweep the gate voltage, V_g, we obtain the PL map and peak data shown in Figure 6.8a-d. As before, the gate map shows a high degree of tunability between excitonic species. Figure 6.8b presents the dependence of the excitonic peak positions on V_g, where the plot symbol size is proportional to the peak intensity. These data reveal a variation in trion charging energies stemming from the quantum-confined Stark effect, which contrasts the constant X^o emission energy [9].

Unlike the studies of Section 3.2.2, we now have the trion fine structure resolved. Interestingly, the peak energy of $X^-_{|2\rangle}$ remains constant from $V_g = 0$ to 1 V, in contrast to the noticeable shifts of the X^+, $X^-_{|1\rangle}$, and $X^{-\prime}$ trion species. This behavior coincides with that of X^o and supports our conclusion of a correlation between $X^-_{|2\rangle}$ emission and state $|2\rangle$.

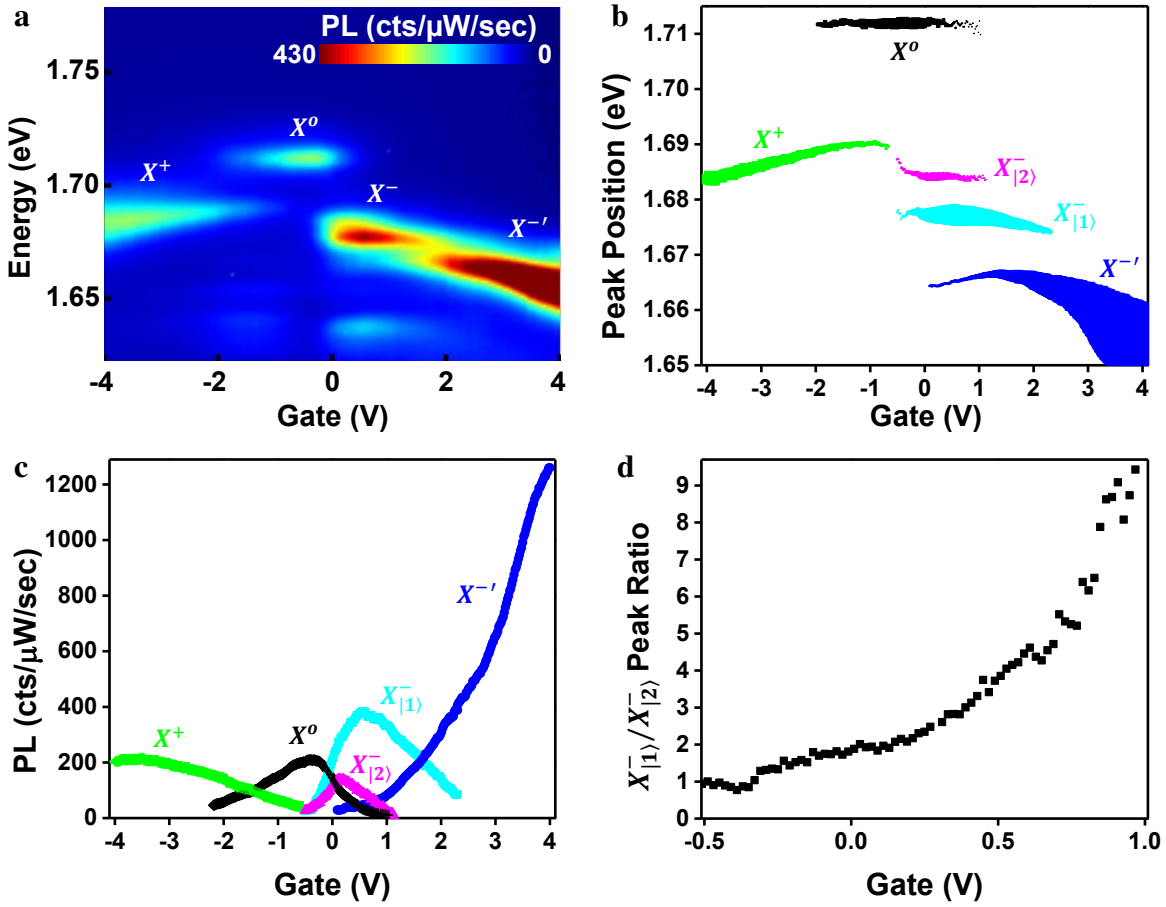

Figure 6.8: **a,** Gate-dependent photoluminescence measurements of BN-supported monolayer WSe_2. **b,** Peak positions of X^o, X^+, $X^-_{|2\rangle}$, $X^-_{|1\rangle}$, and $X^{-\prime}$obtained by fitting the spectrum at each gate voltage with a sum of Lorentzian lineshapes. Plot symbol size indicates fitted peak intensity. **c,** Corresponding gate dependence of excitonic peak intensities. Data for $X^-_{|1\rangle}$ends just above $V_g = 2$ V due to unreliable fitting caused by the overwhelming magnitude of $X^{-\prime}$. **d,** Peak intensity ratio of $X^-_{|1\rangle}$:$X^-_{|2\rangle}$, which approaches unity with decreasing V_g.

Definitive confirmation of state hybridization would take the form of an obvious energy level anti-crossing [130]. Within our model of weak coupling in the detuned limit (i.e. trion binding energy > phonon energy), we could potentially utilize the gate-induced Stark shift of the trion to bring the exciton and trion-polaron into resonance, effectively increasing δ. In the data of Figure 6.8b, the slight curve of $X^-_{|2\rangle}$ to higher peak energies for $V_g < 0$ V and the downward curve of $X^-_{|1\rangle}$ for $V_g > 1$ V hint at an avoided crossing between the two peaks. Since lower voltages correspond to smaller red-shifts of trion states, this behavior agrees with a raising of the phonon-dressed trion energy to bring it nearer the exciton resonance. Unfortunately, the rapidly diminishing peak intensities of $X^-_{|2\rangle}$ and $X^-_{|1\rangle}$ at high and low voltages prohibit accurate determination of peak energies beyond what is shown here. We are thus left without conclusive evidence of level anti-crossing to support the hybridization model.

We note that, though the strong relationship between X^o and $X^-_{|2\rangle}$ has been emphasized many times in this chapter, the gate dependence of X^o, $X^-_{|2\rangle}$, and $X^-_{|1\rangle}$ peak intensities strongly point to charged-exciton contributions within $X^-_{|2\rangle}$. Figure 6.8c presents the fitted excitonic peak heights at each gate. The data clearly show maximum X^o emission near $V_g = -0.5$ V, while $X^-_{|2\rangle}$ peaks near $V_g = 0.1$ V and $X^-_{|1\rangle}$ peaks near $V_g = 0.5$ V. The distinct intensity dependence of $X^-_{|2\rangle}$ confirms that it does not simply stem from a phonon sideband of the X^o state, but rather requires the injection of excess carriers into the monolayer. Note that the offset of maximal X^o emission from $V_g = 0$ V stems from a slight hysteresis in gate-dependent measurements, observed many times by the author.

By recasting the peak intensity data of Fig 6.8c as a ratio of the $X^-_{|1\rangle}$ to $X^-_{|2\rangle}$ peak intensities, we obtain additional evidence of an approach toward equal hybridization of the exciton and trion-polaron. In Figure 6.8d, we see that this peak intensity ratio tends toward unity for decreasing V_g. In a two-state hybridization model, a reduction of the energy separation between levels eventually leads to equal contributions of the two unmixed states, with similar populations within the two hybrid levels [131]. The approaching of $X^-_{|1\rangle}$ intensities to those of $X^-_{|2\rangle}$ at low V_g may indicate a bringing of the exciton and phonon-dressed trion states into resonance near intrinsic doping levels, enabled by the near-degeneracy of the 250 cm^{-1} phonon and trion charging energies (see Figure 6.1a,c).

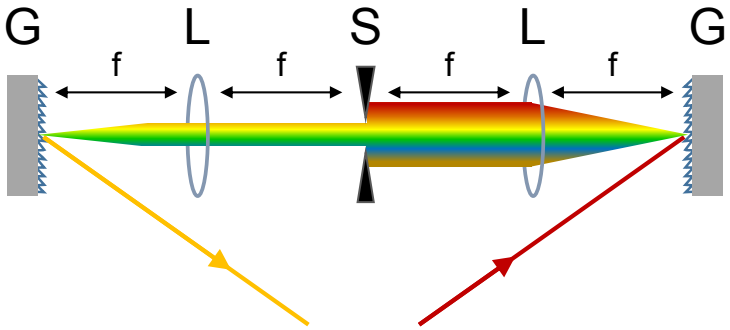

Figure 6.9: Diagramatic depiction of a 4f spectral filter. G, L, S, and f denote diffraction gratings, lenses, an adjustable slit, and the lens focal length, respectively. The first grating spectrally separates the incident light (red line), which the first lens then focuses onto the plane of the adjustable slit. Light passing through the slit is spatially and spectrally recombined by the second lens and grating.

6.2.4 Energy Up-Conversion via Reverse Photoluminescence

With the above discussion in mind, we now turn to our measurements which provide strong evidence for the level hybridization model. We refer to the spectroscopic technique employed here as reverse photoluminescence (reverse-PL). In contrast to conventional PL measurements which excite with an energy higher than detection, reverse-PL excites significantly (> 5 meV) below the detection energy.

For this technique, wavelengths below the peak laser energy are strongly filtered by placing a longpass filter in the excitation beam path at an angle which cuts into the tail of the laser line but transmits the majority of the beam power. We utilize a wedged 50-50 beamsplitter to reflect the incident beam so that the laser wavelength may be scanned for reverse-PLE measurements. On the detection side, a combination of an ultra-steep shortpass filter and adjustable 4f spectral filter separate the remnant laser light from the reverse-PL signal before passing into the spectrometer.

As depicted in Figure 6.9, the 4f filter consists of two gratings located at the outside conjugate planes of two lenses with identical focal lengths, f, for a total spatial separation of 4f. This creates a collimated, spatially-separated spectrum between the two lenses. Placement of a reflective, adjustable slit at the central focal plane spatially filters remnant laser light transmitted through the shortpass filter (indicated by the red arrow), yielding a spectrum comprising only the desired wave-

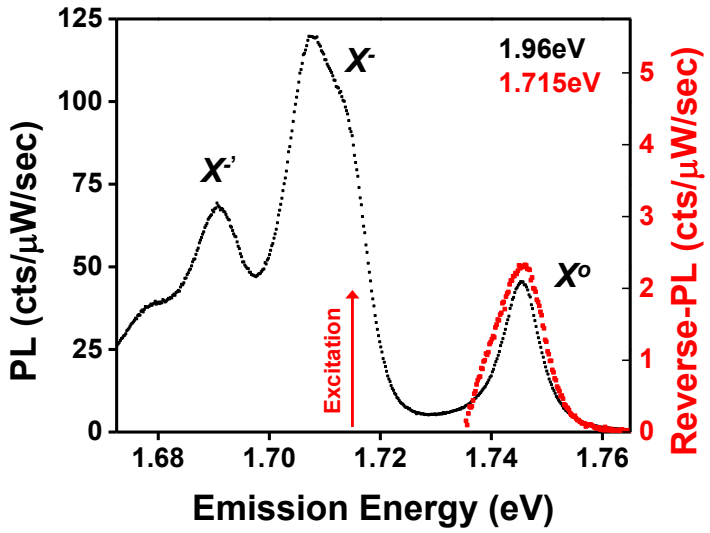

Figure 6.10: Comparison of PL (black data) and reverse-PL spectra (red data) for excitation energies of 1.96 eV and 1.715 eV, respectively. The red arrow indicates the energy of the reverse-PL excitation relative to both the reverse-PL and standard PL spectra. Though the sample temperature corresponds to < 3 meV, the reverse-PL emission peaks ≈ 30 meV above excitation.

length range. While highly-dispersive gratings and long focal lengths provide for sharp spectral resolution, we desire to utilize the 4f filter across a broad wavelength range ($\approx$ 100 nm) in conventional PL measurements as well, which in our configuration effectively limits the separation between excitation and detection energies to > 5 meV.

Our initial reverse-PL measurements show a striking up-conversion of the excitation photon energy by more than $10k_BT$. In Figure 6.10, we present the emission spectrum of monolayer WSe_2 held at 30 K for both 1.96 eV (black) and 1.715 eV (red) excitation energies. The overlap of the red spectrum peak with X^o emission observed in standard PL measurements stands in contrast to the exponential shape one would expect were it to originate from the tail of the resonantly excited trion. In addition, the conversion from trion-energy excitation to X^o emission appears to be quite efficient as the reverse-PL emission strength of X^o is only 20 times weaker than for conventional PL (though this does not account for the wavelength-dependence of the absorption coefficient). This indicates monolayer WSe_2 may function well as an optically-cooled, ultra-thin sheet. Interest in

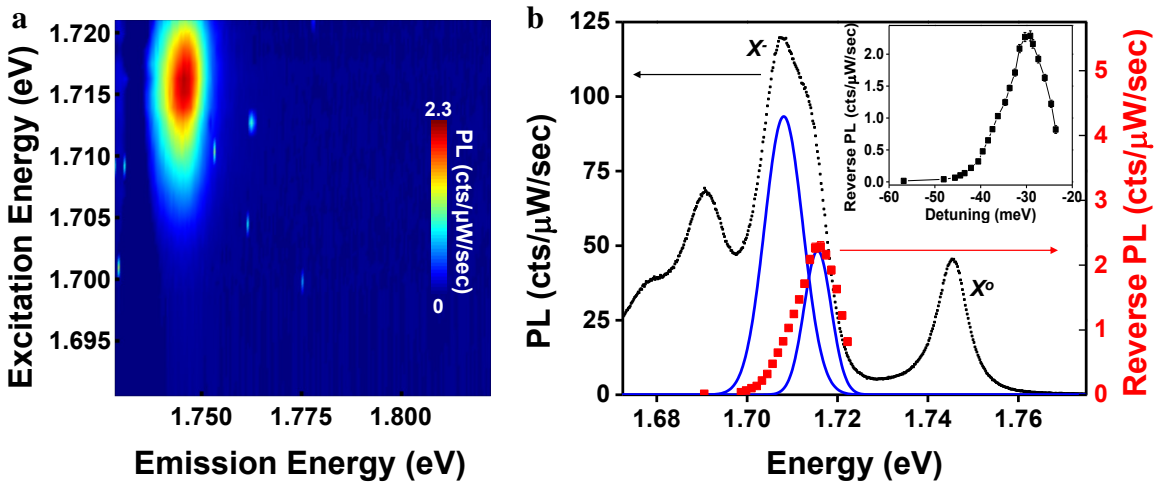

Figure 6.11: **a,** Reverse-PLE map for excitation energies from 1.691 eV to 1.722 eV, showing maximum X^o emission for $\approx$ 1.715 eV excitation. Note the intensity peak of the X^o emisison as well as the constancy of the peak position. **b,** Comparison of reverse-PLE peak intensity (red data) with a standard, 1.96 eV excitation PL spectrum (black data). Blue lines show the $X^-_{|2\rangle}$ and $X^-_{|1\rangle}$ components of X^-. The reverse-PLE peak coincides with $X^-_{|2\rangle}$ emission. Inset: PLE intensity as a function of detuning from X^o.

solid-state laser cooling dates back to 1929 with the theoretical development of Pringsheim [132]. However, experimental realizations did not emerge until 1995 [133], though now cooling by > 100 K in glasses [134, 135] and 40 K in semiconductors [136] has been achieved.

To obtain a more thorough understanding of the trion to exciton energy up-conversion, we perform reverse-PLE measurements where the excitation scans through a range of energies below our detection window. In Figure 6.11a, we present the resulting intensity map with the excitation energy on the vertical axis and the detection energy along the horizontal axis. Interestingly, we observe a distinct intensity peak in the X^o emission. Also note that the emission energy remains constant for all excitation energies explored here.

By taking a line-cut of the reverse-PL peak intensity for each excitation energy and overlaying it with the standard PL spectrum (see Figure 6.11b), we find a maximal up-converted intensity for

excitation at ≈ 1.715 eV, on the high-energy side of X^-. From the standard PL spectrum of Figure 6.11b, a dual-peak fitting to X^- shows both $X^-_{|2\rangle}$ and $X^-_{|1\rangle}$ components given by the blue lines. In this sample, we find Gaussian peaks provide the best fit for the split X^- emission, which indicates significant inhomogeneous broadening contributions to the linewidth. Nonetheless, the overlap between the reverse-PLE peak and $X^-_{|2\rangle}$ is striking. This offers the understanding that when resonantly pumping the trion (i.e. transitions Γ^-_1 and Γ^-_2 in Figure 6.2), the most efficient up-conversion process is excitation from $|e,n\rangle$ to $|2\rangle$ followed by radiative recombination via Γ^o_2. As this process begins in $|e,n\rangle$ and ends in $|e,n-1\rangle$, the net difference between ground states equals one phonon. This optical extraction of crystal phonons is the solid-state analog to laser (or Doppler) cooling of atomic vapors [133].

Additional support of our model comes from the inset to Figure 6.11b, which shows the same reverse-PLE data as in the main figure but with the horizontal axis rescaled to show the energy separation between emission (at X^o) and excitation. A Gaussian fitting of the peak here yields a detuning of 29.9 $\pm$0.15 meV from X^o. Since the excitation and recombination pathways for this process correspond to the Γ^-_2 and Γ^o_2 transitions, respectively, which differ in energy by exactly one phonon, the agreement between the peak detuning and the 250 cm^{-1} Raman mode in monolayer WSe_2 (see Section 6.1) bolsters confidence in the proposed scheme.

Returning again to the valley degree of freedom, the polarization-dependent reverse-PL studies now discussed reveal valley-dependent energy up-conversion inherent in monolayer WSe_2. As a basis for comparison, we first present standard polarization-resolved PL studies under 1.96 eV excitation in Figures 6.12a,c. For circularly polarized excition, the data show a valley polarization of 22% for both X^o and X^- (we do not resolve $X^-_{|2\rangle}$ and $X^-_{|1\rangle}$ here) [53, 62, 63]. With linearly polarized excitation, we find an intervalley coherence of 9% for X^o [9]. The data from low-energy excitation reveal X^o emission which exhibits the same degree of valley polarization, as can be seen in Figure 6.12b. In contrast, linearly polarized, low-energy excitation leads to unpolarized emission as Figure 6.12d shows. Additional measurements also reveal (not shown here) that the degree of valley polarization and absence of intervalley coherence in reverse-PL is consistent for any range of excitation energies for which a reverse-PL signal can be monitored.

The fact that the valley polarization persists in both the up-converted and standard PL measurements of X^o indicates a preservation of valley index during each of the processes. The contrasting

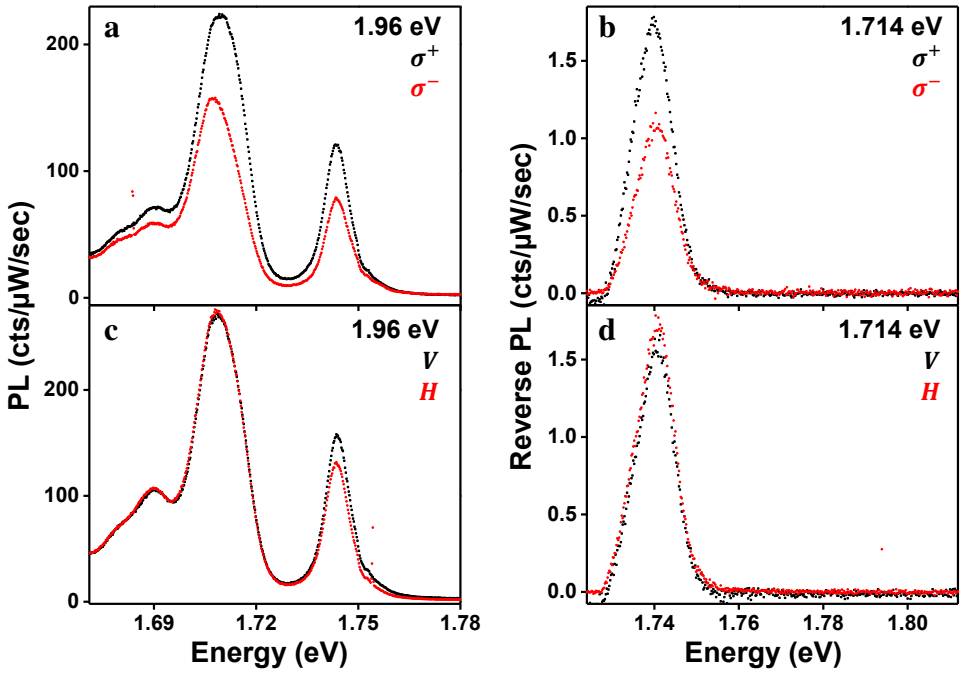

Figure 6.12: **a,** Circularly- and **c,** linearly-polarized PL spectra for co-polarized (black) and cross-polarized (red) detection under 1.96 eV excitation. The circularly polarized emission in **a** reveals valley polarization of X^o and X^- while the linearly polarized emission of X^o in **c** shows the creation of intervalley coherence [9]. **b,** Circularly- and **d,** linearly-polarized *reverse*-PL spectra for co-polarized (black) and cross-polarized (red) detection, using 1.714 eV excitation. The degree of reverse-PL valley polarization matches that of standard PL, while an absence of linear polarization indicates a lack of valley coherence.

absence of linear polarization in reverse-PL offers the additional insight that intervalley coherence does not survive the up-conversion process, which we find in good agreement with our model. Namely, as the up-conversion process involves two orthogonal ground states at very different energies, a lack of intervalley coherence is not surprising.

We also find striking evidence of the importance of charged exciton contributions to the photon up-conversion from $X^-_{|2\rangle}$ to X^o by comparing back-to-back gate-dependent PL and reverse-PL measurements. In Figure 6.13a we present a standard gate-dependent PL map under 1.96 eV excitation, showing tunability between all excitonic species as before (Section 3.2.2). The conjugate reverse-PL

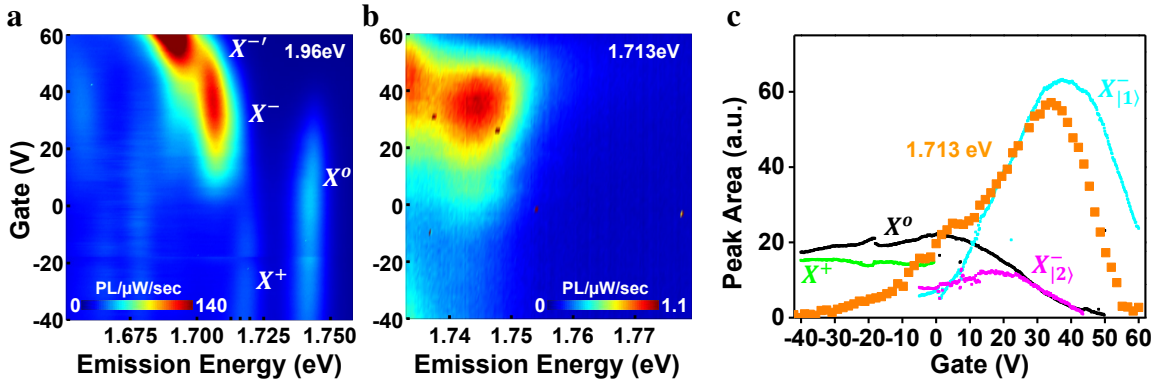

Figure 6.13: **a,** PL intensity gate map, showing tuning between X^+, X^o, X^-, and $X^{-\prime}$via electrostatic doping. **b,** Reverse-PL gate dependence map for 1.713 eV excitation (near $X^-_{|2\rangle}$), showing the correlation between the strongest up-converted X^oemission and maximum X^-emission in **a**, both occurring at $V_g \approx 35$ V. **c,** Comparison of the peak area of each excitonic species for the gate-dependent PL and reverse-PL data shown in **a** and **b**. For 1.96 eV excitation, we extract the peak areas by fitting the spectrum at each gate with a Lorentzian for $X^o$and a Gaussian for every other peak (small symbols). The resulting peak areas for X^+, X^o, $X^-_{|2\rangle}$, and $X^-_{|1\rangle}$are shown in green, black, magenta, and teal, respectively. For reverse-PL measurements, we obtain the X^opeak area (large, orange symbols) by fitting a Gaussian at $X^o$and at the excitation energy (see text for explanation). Note that the magnitude of the reverse-PL peak area has been scaled by a factor of 10 to facilitate comparison.

gate map of Figure 6.13b for 1.713 eV excitation likewise shows strongly tunable emission, though the maximum in X^oemission occurs for $V_g \approx 35$ V. The fact that reverse-PL emission peaks at the same voltage as X^-in standard PL measurements corroborates our understanding that the photon up-conversion process relies on the presence of excess electron doping, which allows for the formation of negative trion-polarons. With the corresponding level hybridization proposed here, transitioning from a ground state with n to $n-1$ phonons is facilitated.

To aid in the comparison of the gate-dependent behavior of reverse-PL with the emission pattern of standard PL measurements, we fit each spectrum with a summation of peaks and present

the extracted peak area in Figure 6.13c. The results show a maximum in X^+(green), X^o(black), $X^-_{|2\rangle}$(magenta), and $X^-_{|1\rangle}$(teal) emission at -40 V, 2 V, 18 V, and 38 V, respectively. We do not show the data of $X^{-\prime}$to enhance figure clarity. Note that scatter in the peak areas as well as the discontinuity in X^opeak area near $V_g = -20$ V stem from artifacts of the automated peak fitting and do not affect our interpretation.

For the reverse-PL data, we fit each spectrum with two Gaussians. From the Gaussian at 1.745 eV we obtain the up-converted peak area (Figure 6.13c, orange markers), while the second Gaussian centered at the energy of the excitation laser accounts for the emission from resonantly excited trions. The "tail end" contribution of this resonantly-excited trion emission can be seen most clearly on the low-energy edge of the gate map of Figure 6.13b for V_g near ±40 V, doping levels for which standard PL trion emission is strongest. The reverse-PL peak fits reveal a X^oarea which closely follows the summation of the $X^-_{|1\rangle}$and $X^-_{|2\rangle}$peak areas, with a decay to zero amplitude for positive doping. This unambiguously establishes the relationship between photon up-conversion in monolayer WSe_2 and contributions from charged excitonic states, in line with the presence of $|X^-\rangle \otimes |n\rangle$ components within the $|1\rangle$ and $|2\rangle$ hybrid states of our model.

Finally, we perform a similar comparison of the PL and reverse-PL temperature-dependent response of monolayer WSe_2. Akin to the data of Section 3.2.1, Figure 6.14a presents the PL spectra over a temperature range of 20 - 240 K, for 1.96 eV excitation and $V_g = 0$ V. We find that with increasing temperature the contribution of X^-diminishes while X^opeaks in intensity near 100 K.

Figure 6.14b presents the temperature-dependent reverse-PL spectra obtained under conditions of resonant trion excitation. Due to the strong red-shift of the spectra with temperature, we hold the excitation energy at 30 meV below peak X^oemission. As with our standard PL measurements, we find a strong increase in X^oemission for sample temperatures near 100 K. We note that the color intensity scales of Figures 6.14a,b differ by one order of magnitude, again signaling the efficiency of reverse-pumped PL in monolayer WSe_2. Repetition of these measurements across three samples yields consistent results.

After integrating the peak area of low energy-excited X^oat each temperature, we arrive at the temperature-dependent intensity of reverse-PL emission presented in Figure 6.14c. To facilitate comparison, we normalize the data obtained from three different samples by their respective peak areas at 30 K. In contrast with the exponential temperature dependence of anti-Stokes luminescence

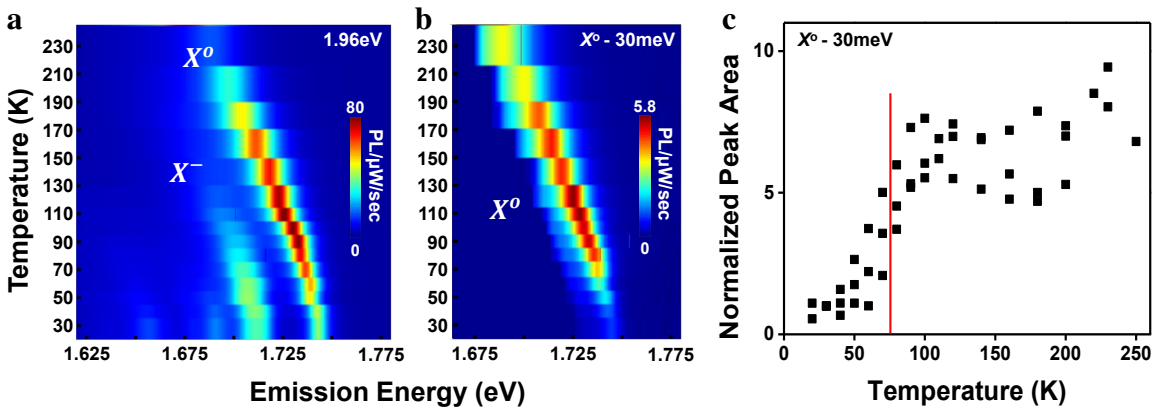

Figure 6.14: **a,** PL intensity temperature map, showing red-shifting of X^o and X^- with increasing temperature. X^o emission increases significantly as temperature rises through 70 K. **b,** Reverse-PL temperature dependence map showing a similar increase in X^o emission as seen in **a**. For all spectra here, the excitation was maintained 30 meV below the peak X^o emission energy. **c,** Normalized peak area of X^o emission for reverse-pumping at each temperature, showing data obtained on three different WSe_2 monolayers. To facilitate comparison, each data point is normalized by the peak area at 30 K. The red line indicates a temperature of 76 K.

up-conversion observed in GaAs quantum wells [137], we find an intensity step, with an intensity increase of more than 5x. We also note that the increase observed in conventional PL measurements is much lower, a factor of 2.5x. The red line in Figure 6.14c shows that the reverse-PL intensity step occurs near 75 K. Recall that in Section 6.2.2 we found a $X^-_{|2\rangle}$-$X^-_{|1\rangle}$ peak splitting of 6.55 meV = 76 K. From our model, this corresponds to the $|2\rangle - |1\rangle$ energy separation. We then understand the reverse-PL intensity increase as thermal excitation from the predominantly phonon-dressed trion state $|1\rangle$ to the neutral exciton-like state $|2\rangle$. As this significantly increases the population of the higher-lying $|2\rangle$ state, we observe a concomitant increase in X^o emission. For temperatures of 100 K and above, $|1\rangle$ and $|2\rangle$ are brought into thermal equilibrium and the increase in X^o emission saturates.

We thus find that all of the data presented in this section support the assignment of the dual X^- peaks to recombination from weakly hybridized levels comprised of neutral excitons and trion-polarons.

6.3 $X^{-\prime}$- The Multi-Valley Heavy Trion

In the final section of this chapter, we outline evidence for assignment of the $X^{-\prime}$peak of monolayer WSe_2 to trion states arising from the multi-valley and nearly degenerate conduction band structure of tungsten-based TMDs. Strong support for this model comes from the contrasting band structures of W and Mo based TMDs with the corresponding observation and absence of a low-energy, $X^{-\prime}$spectral feature in each. Specifically, such a feature emerges in WSe_2 [9] and WS2 [138] while absent in MoSe2 [8] and MoS2 [41, 101].

Following the work of References [26,139], we depict the low-energy band structure of tungsten TMDs in Figure 6.15. In contrast to the abundant band depictions of monolayer WX_2's which focus predominantly on the K-valleys at the corners of the 1st Brillouin zone, here we take into consideration that the lowest energy conduction band possesses nearly-degenerate minima at both K and λ valleys. Note that the λ valley resides halfway along the line from Γ to **K** and is strongly spin-split with the lowest-energy band carrying the same spin orientation as the dipole transition-allowed band at the K-point. Calculations show that at nearly intrinsic doping levels ($V_g \approx 0$), the λ valley conduction band minimum lies slightly higher than the K valley minimum, as in Figure 6.15a, with an energy separation of 100 meV or less [139]. Here we expect configurations leading to trion formation to arise from all carriers located at the ±K valleys. Application of a large gate voltage, leading to large electron-doping, causes the λ valley band to move to lower energy while the K valley energy remains nearly constant as depicted in Figure 6.15b [139]. With this change in band structure, we find the dominant contribution to optically-active trion states (i.e. the lowest energy configuration) comes from an electron-hole pair at the K-valley bound to an excess electron within the λ valley.

Importantly, we note that the magnitude of the doping-induced shift of the λ valley conduction band depicted in Figure 6.15b occurs at very large carrier concentrations (e.g. 2×10^{14} cm^{-2}). Still, the near energy degeneracy between the λ and K valley bands requires consideration of both bands when studying low energy carriers, especially with the injection of excess negative carriers. This is due to the large ratio of λ valley effective electron mass, m_e^{λ}, to that derived from the K valley bands, m_e^{K}. Calculations of electron effective masses in monolayer TMDs yield a constant m_e^{λ}:m_e^{K} ratio of 1.5 for bilayers, trilayers, and quadrilayers of WSe_2 and 1.8 for bilayer WS_2 [140]. A larger

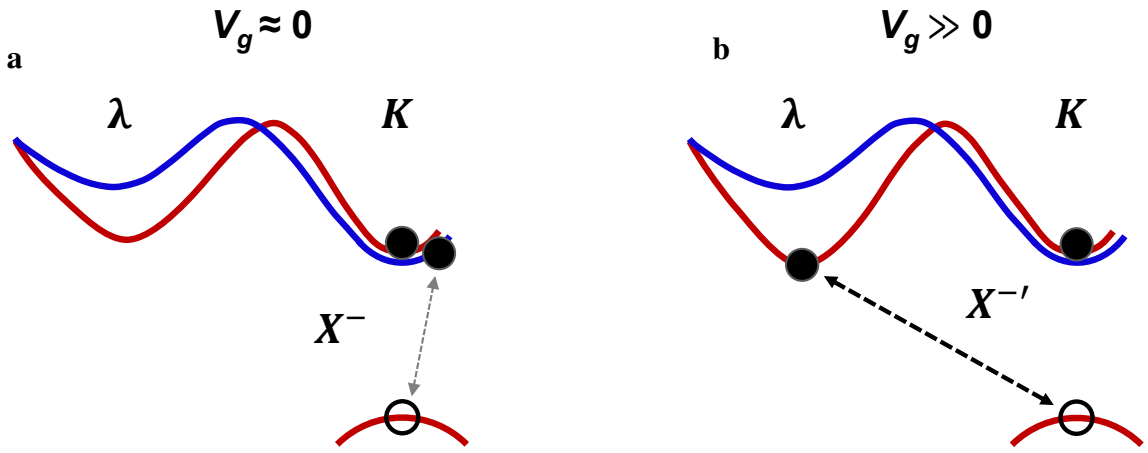

Figure 6.15: Band structure schematic of tungsten-based monolayer TMDs at low and high doping levels. **a,** At low electrostatic gate voltages, the lowest energy trion states originate from all carriers residing within the ± K valleys. **b,** For large doping levels, the λ-valley conduction band significantly lowers, leading to the formation of trions with an electron contribution from the λ valley. Arrow thickness indicates Coulomb interaction strength. Note that the λ valley conduction band minimum is also the dipole-transition allowed K-point conduction band, potentially allowing for efficient optical pumping of λ valley electrons.

effective mass corresponds to stronger Coulomb interactions and thus greater binding energies. This then indicates that with an X^-binding energy of $\approx$ 30 meV for $V_g \approx 0$, a binding energy of 45 meV is reasonable for λ valley trions. Note the strong correlation to the $\approx$ 47 meV binding energy of $X^{-\prime}$near its onset ($V_g \approx$ 25 V) shown in the inset to Figure 3.4b.

Such a contrast in binding energy means that for degenerate K and λ valley conduction bands, a λ valley trion configuration would be energetically favorable. Expressing this in a four-particle subspace, we have a higher energy for $|X_K^-\rangle|e_\lambda\rangle$ than for $|X_\lambda^-\rangle|e_K\rangle$, where X_K^- (X_λ^-) denotes a trion state with the excess carrier in a K (λ) valley, while $|e_K\rangle$ ($|e_\lambda\rangle$) denotes an electron in valley K (λ). We also note that these two trion configurations are directly coupled via the Coulomb interaction, without the involvement of phonons. Consequently, trion formation in tungsten-based TMDs may

contain contributions from multiple valleys, depending on the doping level. With the above considerations, we assign $X^{-\prime}$emission to λ valley trion configurations, X_{λ}^{-}, as in Figure 6.15b, and provide supporting evidence throughout the rest of this section.

If the heavier effective mass of the λvalley electron leads to stronger binding between $|e_{\lambda}\rangle$ and the K valley hole, $|h_K\rangle$, than between $|e_K\rangle$ and $|h_K\rangle$, we expect a reduction in the optical transition strength. We find support for this in our comparisons of the white light differential reflectivity of $X^{-\prime}$states in monolayer WSe_2 and WS_2 shown in Figure 6.16. For monolayer WSe_2 we find that the strong $X^{-\prime}$peak already discussed in Section 3.2.2 corresponds to the weakest white light $\Delta R/R$ feature (cf. Figure 6.16a,c at large voltages). In contrast, X^o, X^-, and X^+lead to strong $\Delta R/R$ features. Similarly, in WS_2 we find the strongest PL emission near 2.0 eV, with a small neutral exciton contribution near 2.07 eV (Figure 6.16b), while the dominant white light derivative features occur at 2.07 eV and 2.05 eV. Our assignment of the 2.07 eV emission to X^ocoincides with measurements of Chernikov *et al.* [36]. We thus assign the $\Delta R/R$ signals near 2.07 eV and 2.05 eV as arising from the exciton and negative trion, respectively, whose signal strength diminishes for increasingly positive gate voltages, consistent with the behavior of the $X^o$and X^-features in $\Delta R/R$ measurements of monolayer WSe_2. The weak differential reflectance signal below 2.05 eV in WS_2 also exhibits significant red-shifting with increasing gate voltage, which aligns with the behavior of WSe_2 at high gate.

Further support for our assignment of $X^{-\prime}$emission to X_{λ}^{-} trions comes from time-resolved PL studies. In monolayer WSe_2, these measurements reveal a significantly longer emission time for $X^{-\prime}$compared to $X^o$and X^- [66], which agrees with a reduced transition strength and our observations of a lower absorption cross-section.

Another probe of X_{λ}^{-} configurations comes from the ordering of the λvalley bands. If the trion configuration underlying $X^{-\prime}$emission does indeed stem from the configuration depicted in Figure 6.15, then the contributing λvalley electron will be highly spin oriented due to the 100's meV conduction band splitting there [26, 139]. Correspondingly, our measurements of valley polarization for $X^{-\prime}$reveal significantly higher values than for X^o, X^-, and X^+(see Figure 4.1d) [9], which is reasonable assuming a trion configuration with robust spin orientation of the excess electron.

As already mentioned, in our gate dependent measurements of monolayer WSe_2 (Figure 3.4), we find the emergence of $X^{-\prime}$at a higher red-shift than X^-, and only for strongly negative doping

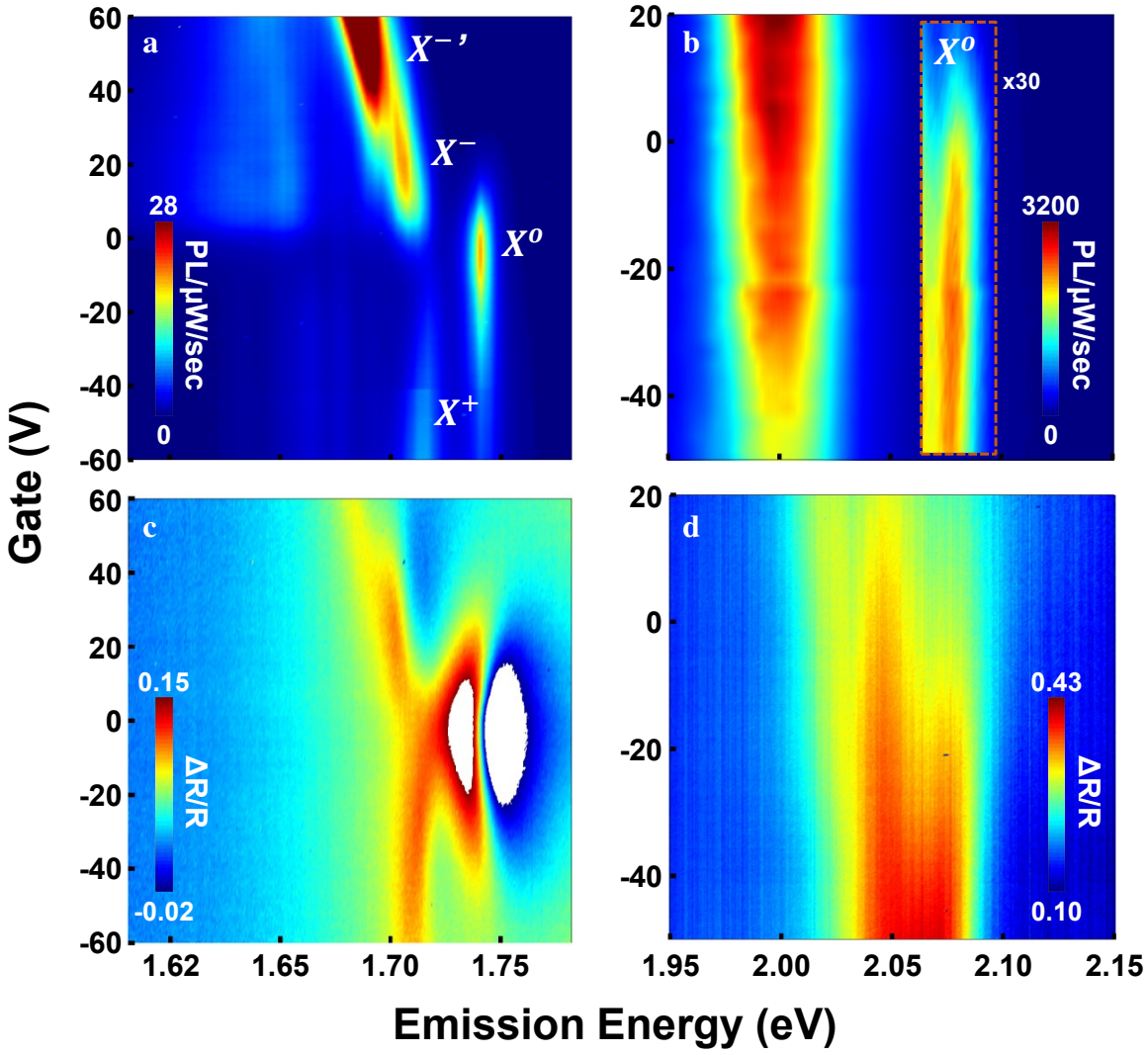

Figure 6.16: **a,** Gate-dependent PL spectrum of monolayer WSe_2. **b,** Gate-dependent PL spectrum of monolayer WS_2 showing strong emission near 2.0 eV, with increasing intensity at higher electron doping. The dashed orange box outlines the region of X^o emission, with the color scale magnified by a factor of 30. A weak emission peak near 2.05 eV may also indicate negative trion states. **c,** White light differential reflectivity of monolayer WSe_2 showing strong derivative-like features for the excitonic emission of X^o, X^+, and X^-, while $\Delta R/R$ at high gate near $X^{-\prime}$ emission remains weak. **d,** White light differential reflectivity of monolayer WS_2 showing strong response near 2.07 eV and 2.05 eV, with weak response below 2.05 eV.

levels. This emission continues to quickly redshift with increasing doping (see Figure 6.8b), which aligns well with the prediction of doping-induced downward movement of the λ valley [139], in addition to the quantum-confined Stark effect [9]. While significant shifts of the λ valley band are easily seen at very high doping levels in the data of Reference [139], their calculations do show a lowering by 50 meV with a doping concentration increase from 1×10^{13} cm^{-2} to 2×10^{13} cm^{-2}. While these are achievable doping levels in TMDs [141], they are likely not the dominant source of the shift seen here. Still, the drastic intensity increase of $X^{-\prime}$at higher gates does signal a transition to becoming an evermore energetically-favorable state, consistent with the decrease of the λ valley band.

While other measurements of monolayer WSe_2 have previously attributed emission near $X^{-\prime}$to localized excitons [66], our power-dependent measurements of its emission intensity do not show any saturation behavior for intensity variations over 3 orders of magnitude. Additionally, our observations of strong $X^{-\prime}$emission emerging only for significant electron doping (Figure 6.16a,b) also contradict a biexciton interpretation [138, 142] since biexcitons are expected to follow the neutral exciton density (strongest for intrinsic doping levels) [143] and which do not form in the presence of large excess carrier populations [144]. Further, our measurements across multiple devices of WSe_2, WS_2, MoS_2, and $MoSe_2$ reveal that such a low-energy, strong emission peak only occurs in the gate-dependent studies of WSe_2 [9] and WS_2 [138] while entirely absent in MoS_2 [41, 101] and $MoSe_2$ [8]. This contrast can be attributed to the landscape of the λvalley conduction bands in Mo-based TMDs, which are not nearly degenerate with those of the K valleys, but lie at much higher energies [26, 139]. Consequently, the formation of X_λ^- in MoS_2 and $MoSe_2$ does not occur. Further, temperature-dependent measurements of $X^-$and $X^{-\prime}$in monolayer WSe_2 (not presented here) reveal similar evolutions in intensity and red-shift, which corroborate the assignment of $X^{-\prime}$as a trion state.

We find that, when taken together, the calculated TMD band structures, our experimental observations, and others' findings support the assignment of the $X^{-\prime}$emission to a λvalley negative trion, X_λ^-.

6.4 Conclusion

In this chapter we have explored the various emission peaks which emerge below the neutral exciton in monolayer WSe_2. From the coincidence between trion charging and phonon energies we introduce a model of weak hybridization for the neutral exciton and trion-polaron, which accounts for the two peaks which emerge at the energy of X^-.

Support for this model comes from our measurements of gate-, temperature-, and polarization-dependent PL studies. Following this characterization, we find further evidence by repeating these studies in a reverse-PL configuration, in which we resonantly excite the trion and monitor emission at the exciton energy. This efficient energy up-conversion occurs on scales much larger than the available thermal energy. Such a behavior indicates the applicability of monolayer WSe_2 in solar cells as near-IR photon up-conversion holds promise to beat the single-junction Shockley-Queisser efficiency limit of 32% [145]. Additionally, efficient optical cooling of ultra-thin membranes may find unique scientific and technological applications.

Finally, we outline our measurements of $X^{-\prime}$emission. We find the most consistent explanation for the observed behaviors comes in the form of a trion state where the excess electron resides in the λvalley. Importantly, we only find such a trion configuration in the tungsten-based TMD species, consistent with the conduction band energy landscape obtained by band structure calculations for all TMDs mentioned here.

These studies elucidate the richness of the spectral landscape within monolayer WSe_2 and establish a framework for directing future studies.

Chapter 7

OPTICALLY DRIVING MECHANICAL RESONANCES OF SUSPENDED MEMBRANES

7.1 Non-linear Damping Theory and Experimental Setup

This chapter presents studies of optically-driven nanomechanical motion of ultra-thin TMDs suspended over micron-size holes. The motivation for examining suspended nanomechanical oscillators comes from applications such as compact frequency references [146], rf receivers [147], and mass and pressure sensors [148–154], in addition to being macroscopic probes of non-linearly damped Duffing oscillators [155–157], and quantum phenomena [158, 159]. Suspended membranes such as graphene and ultrathin TMDs offer the additional benefit of a high fracture strain limit for durability and large amplitude oscillations [160].

To aide in the discussion of non-linearities observed in the nanomechanical response of our suspended membranes, we briefly outline the theory of overdriven Duffing oscillators. The non-linear, second order Duffing equation describes the response of damped and driven oscillators where deviations from a harmonic response must be accounted for, and has the form

$$\ddot{x} + 2\gamma\dot{x} + \omega_0^2 x + \beta x^3 = F_0 \cos(\omega t) \tag{7.1}$$

with the damping coefficient γ, resonant frequency ω_0, non-linear restoring force β, and driving force amplitude F_0 and frequency ω. For $\beta = 0$, this reduces to the driven, damped simple harmonic oscillator. The role of the β is perhaps best seen in the frequency-dependent response of the oscillator amplitude for increasing driver amplitudes. To examine this, we assume a steady-state response of $A\cos(\omega t + \theta)$, which, when inserted into Equation 7.1, yields an amplitude-frequency relation of the form

$$A^2(\omega_0^2 - \omega^2 + \beta A^2)^2 + (2A\gamma\omega)^2 = F_0. \tag{7.2}$$

Solving for the frequency response of A yields the oscillator amplitude curves shown in Figure 7.1, where we have taken $\omega_0 = 20$, $\gamma = 0.1$, $\beta = 0.1$. The black, red, green and blue curves correspond

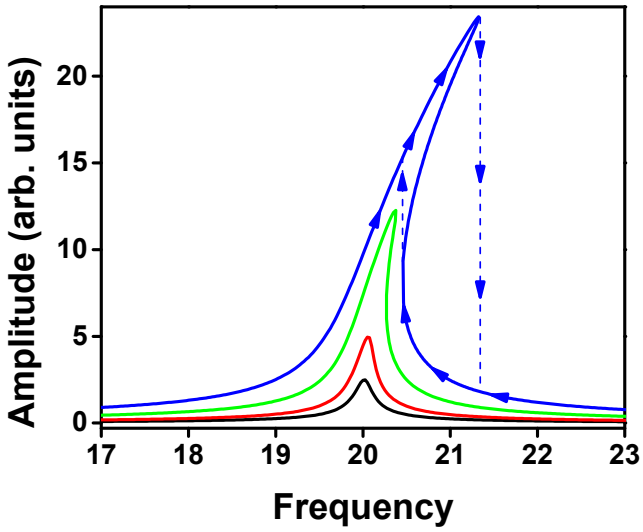

Figure 7.1: Oscillation amplitude of a non-linear damped Duffing oscillator as described by Equation 7.1, with $\omega_0 = 20$, $\gamma = 0.1$, $\beta = 0.1$. Black, red, green, and blue curves correspond to $F_0 = 10$, 20, 50, and 100. The overshoot of the peak stems from the non-linearity, β, of the system for larger driving forces, which for positive values gives a hardening of the 'spring' with the resultant up-shift in resonant frequency. A sign reversal of β yields a softening of the spring, which would yield the same resonance curves shown here just reflected across the axis of the resonant frequency, ω_0. The blue arrows on the $F_0 = 100$ curve indicate the frequency hysteresis characteristic of overdriven Duffing oscillators.

to driving amplitudes of F_0 =10, 20, 50, and 100, respectively. For high driving forces, the non-linearity causes the resonance to change from a Lorentzian to a 'cresting wave' shape, resulting in an amplitude bistability with frequency hysteresis. As indicated by the blue arrows, when the driving frequency is swept from low to high frequencies, the oscillator amplitude grows until reaching the global maximum, at which point it falls to the baseline. When sweeping from high to low frequencies, the amplitude will rather follow the left-facing arrows until reaching the underside wall of the 'wave', where the amplitude jumps to the higher curve. This frequency hysteresis provides a type of memory in which the direction the driving frequency has been swept is remembered.

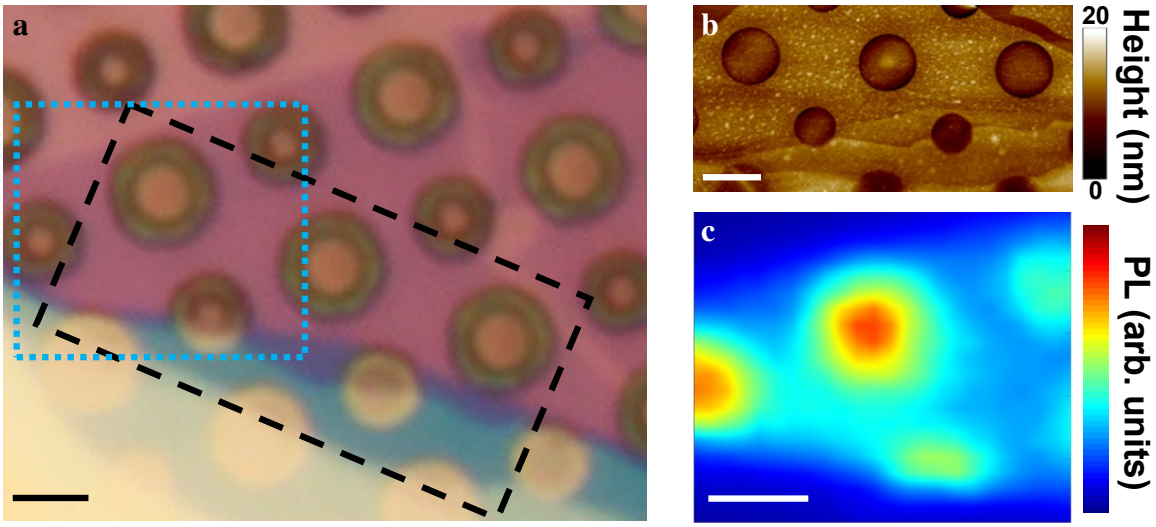

Figure 7.2: **a,** Optical microscope image of mono- and multi-layer WSe_2 transferred onto a hole-patterned substrate. **b,** AFM height map of the region indicated by the black dashed lines in **a**, showing monolayer WSe_2 suspended over all holes within the map area. **c,** Spatial PL intensity map of exciton emission within the region marked by the blue dotted lines in **a**, showing stronger emission for suspended areas. All scale bars are 2 μm.

We now move on to an examination of non-linearities in suspended ultrathin TMDs. The suspended ultrathin TMD membranes are obtained either through mechanical exfoliation onto hole-patterned substrates, or by transferring substrate-supported flakes using dry transfer techniques (see Supplementary Material of [161]). Since the difference in optical contrast between suspended and supported membranes is negligible, verification of membrane suspension can be performed using AFM or, for monolayers, PL measurements. Figure 7.2a shows an optical microscope image of a monolayer WSe_2 flake dry-transferred onto a grid of 1 μm and 2 μm holes etched into SiO_2. The purple film filling the central region of the image corresponds to the monolayer portion of the transferred flake. The black dashed lines indicate the region in which the AFM height measurements shown in Figure 7.2b were performed. With a hole depth of $\approx$ 2 μm, the relatively small height variation across the entire map reveals that all holes within the AFM region are covered by

drumhead-like membranes. The apparent drop in height near the edges of the holes is likely an artifact of the measurement, and matches previous AFM measurements of suspended ultrathin materials [162]. Spatially mapping the PL intensity from the region enclosed by the blue dotted lines in Figure 7.2a yields Figure 7.2c. Here, the localized regions of stronger luminescent intensity correspond to the locations of the subtrate holes, and thus likewise verify the suspended nature of the monolayer in this region [3, 163].

To investigate the behavior of TMD membranes in mechanical resonance, we designed an all-optical driving system for the excitation and readout of nanoscale motion, similar to the one employed in Reference [150]. As the presence of air molecules significantly damps the sub-nm oscillations we aim to study, the sample must be held in vacuum ($\lessapprox 10^{-5}$ Torr). To drive the membrane, we direct the output of a vector network analyzer (Agilent E5072A) to the rf driver (Gooch Housego 1200AF-AIF0) of an AOM (see Figure 7.3). This modulates the output of a 532 nm diode laser, which a dichroic mirror combines with a cw reference beam from a 633 nm diode laser. Both beams reflect off of another dichroic mirror and are then focused to a spot size of $\approx 1\mu$m by a 40x Olympus microscope objective. The dichroic mirror which reflects both excitation and detection beams allows for simultaneous photothermal driving of the suspended membrane and collection of the PL spectrum by the coupled CCD/monochromator.

The 633 nm reference beam acts as an interferometric detector of membrane oscillations which are in phase with the 532 nm driver. As depicted in the bottom of Figure 7.3, the membrane (gray curve) is suspended above a hole or trench. A fraction of the reference beam reflects from the membrane surface, while the majority is reflected by the Si substrate below. Relative phase shifts between the two reflections lead to intensity modulations, which are detected on the return path of the 633 nm beam by the fast photodiode on the output of the beamsplitter. Under a non-resonant driving force, small motions of the membrane surface remain incoherent with respect to the phase of the driving frequency. These motions are not resolved as the input port of the VNA measures the in-phase component of the photodiode output with reference to the driving frequency. However, when driven into resonance, the moving membrane surface alters the relative phase between the two reflected reference beam components in-phase with the driving force. The magnitude of this phase shift corresponds to the membrane oscillation amplitude and leads to corresponding oscillations in the reflected 633 nm beam intensity.

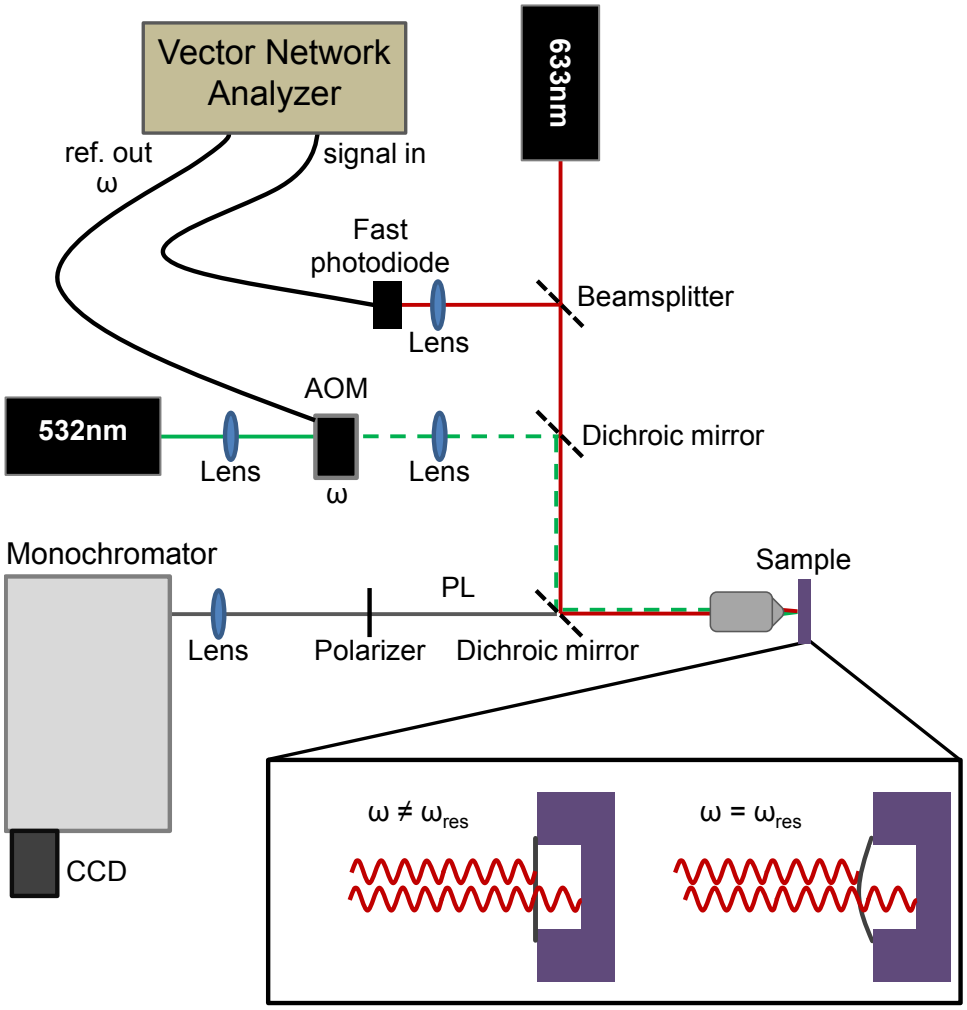

Figure 7.3: Two-laser optically-driven membrane resonance experimental configuration. The output port of a vector network analyzer drives an acousto-optic modulator which modulates the 532 nm pump beam (dashed green line). A dichroic mirror combines the pump and reference (633 nm) laser, which are then focused on the suspended sample. A beamsplitter sends the reflected reference beam onto a fast photodiode, whose signal is referenced to the drive output. When $\omega = \omega_{res}$, oscillation of the membrane varies the phase between optical fields reflected from the membrane and the bottom of the substrate. The monochromator allows for simultaneous examination of the photoluminescence spectrum as the pump beam drives the membrane.

With reference beam optical powers of $\leq 100\mu$W, the $\approx$ nV oscillatory signal expected from the photodiode presents some difficulties in detection. Specifically, such a small signal must be amplified before detection, requiring compensation for rf broadcasting from imperfect connections and cable shielding. For instance, the use of common RG-58 coaxial cables and the small separation between the "ref. out" and "signal in" lines depicted in Figure 7.3 would completely swamp the true signal due to intense broadcasting of the driver signal and significant pickup on the detection side. For this reason, we use RG142B/U double shielded coaxial cables, which offer 90 dB of rf attenuation, with an additional braided cable sleeve on the VNA output line for added shielding. We also use two Mini Circuits rf amplifiers (ZHL-3A and ZFL-1000LN+) in series for the dual purposes of increasing the photodiode output signal by 45 dB as well as to strip the large DC offset from the oscillatory signal. With each stage of amplification, electromagnetic shielding requirements become less stringent. Finally, to block the small but finite amount of 532 nm beam which makes it back to the detection arm, we place a 532 nm notch filter (optical density > 6) before the photodiode's focusing lens.

7.2 Preliminary Results on Overdriven Suspended Membranes

In this section we present our initial results from optically driving ultrathin suspended TMD sheets into mechanical resonance utilizing the system just discussed. These initial studies focus on a 5 layer-thick sheet of WSe_2 suspended over a 2 μm hole in a vacuum better than 10^{-5} Torr. This sheet thickness lies at the crossover between the membrane-like and circular plate-like response found in related studies of MoS_2, where the fundamental resonance frequency is lowest [164].

For the data shown in Figure 7.4, 10 μW of rf-modulated 532 nm laser light focused to $\approx 1\mu$m drives the resonance while 50 μW of the cw 633 nm probe detects the membrane oscillations. Normalization of the reflected probe intensity modulation by the total reflected power allows for a quantitative measure of the oscillation amplitude, $\Delta R/R$. The strongest peak in the spectrum presented here corresponds to fundamental mode oscillations at f_{01} =29.1 MHz, with a beam intensity modulation of $\approx 0.4\%$. The peak has a quality factor Q=40. At higher frequencies, a higher order mode appears at $1.5f_{01}$, which agrees well with the $f_{11} = 1.59f_{01}$ expected for the next resonant mode of a circular membrane [165]. The insets depict the membrane displacements for both of these

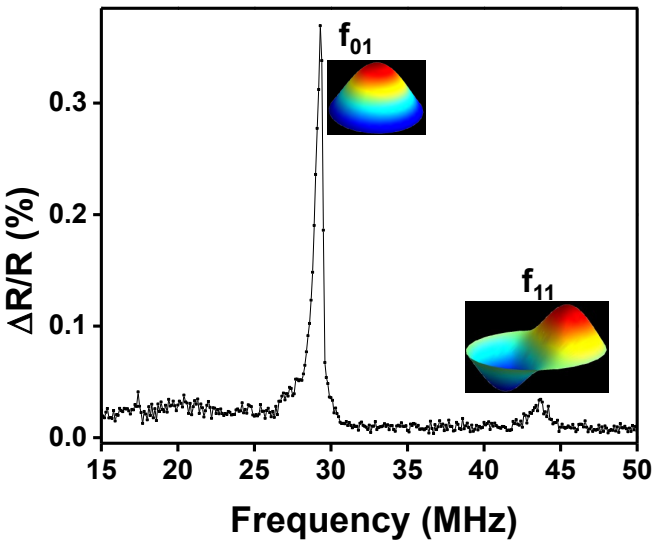

Figure 7.4: Percent change in probe beam power reflected from a few-layer WSe_2 sheet suspended over a 2 μm hole, driven by 10 μW of 532 nm laser light modulated at the frequency indicated on the bottom axis. The resonance at 29.1 MHz corresponds to the fundamental oscillation mode of a drumhead, as indicated by the inset depiction, while the resonance at 43.7 MHz comes from the higher order mode depicted. The drive frequency is swept from low to high frequencies.

oscillatory modes.

The shape of the resonance spectrum also reveals a slight asymmetry, indicating that the amplitude of the membrane oscillations has already entered the non-linear regime. Due to the fixed scan direction set within the VNA, all measurements sweep the drive from low to high frequency and thus don't allow verification of the frequency hysteresis discussed in the previous section.

To estimate the magnitude of the membrane oscillations, we utilize the fact that physical displacement of the oscillating membrane corresponds to a fraction of the probe beam wavelength, λ_p. Thus, a peak-to-peak membrane oscillation amplitude of $O(\frac{\lambda_p}{2})$ will lead to maximum constructive and destructive interference of the pump and probe beams. To estimate the magnitude of the intensity modulations, we take 40% as the reflected power from the highly doped silicon wafer [166], which we reduce by a factor of 2 to account for losses associated with defocusing and scattering as the beam traverses the few μm deep hole and re-enters the objective. A 20% intensity reflection

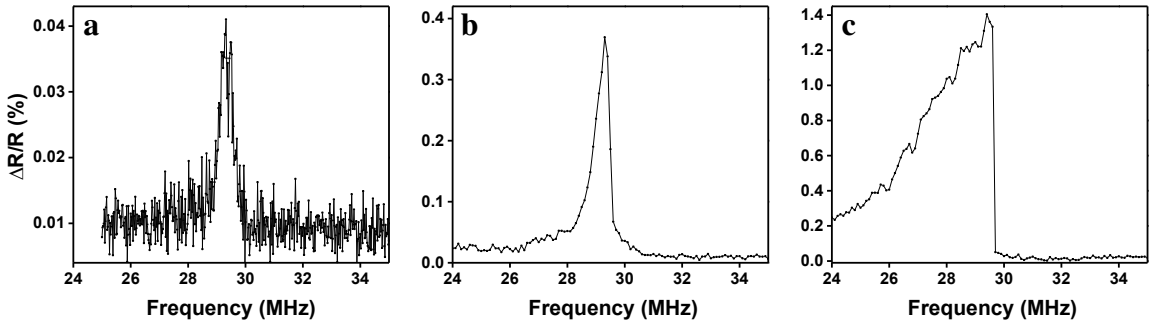

Figure 7.5: Membrane oscillation amplitude for an rf-modulated optical drive power of **a,** 2 μW, **b,** 10 μW, and **c,** 50 μW. The symmetric peak shape in **a** indicates an oscillation amplitude where the non-linear response remains insignificant. The larger driving powers of 10 μW in **b,** and 50 μW in **c,** induce increasing asymmetries in the frequency response as the non-linear component of the restorative force turns on. The driving frequency sweep direction is from low to high.

from the membrane surface is also assumed [167]. With equal reflected powers of the two beams, we assume that full modulation of the total reflected power occurs for $\lambda_p/2$ movements. Solving for the membrane displacement which provides the proper phase shift for a 0.4% intensity modulation furnishes an amplitude estimate of 13 nm peak-to-peak. Clearly, the inset schematics to Fig 7.4 exaggerate the out-of-plane displacement as the proper aspect ratio of the displacement to the suspended membrane width is ≈ 200.

Performing drive intensity-dependent measurements allows for estimation of the oscillation amplitude at which non-linear effects become significant. In Figure 7.5a-c we present the resonance spectra of this few-layer sheet for three different drive intensities and constant probe/readout power. At a low driving power of 2 μW (Fig. 7.5a), we find a symmetric resonance at 29 MHz and a change in probe reflectivity that corresponds to $\approx$ 4 nm vibrations of the membrane. The zoomed in view of the fundamental mode for a 10 μW drive, presented in Figure 7.5b (cf. Fig. 7.4), more clearly shows the non-linear response apparent for $\approx$ 13 nm oscillations, while Figure 7.5c shows that 50 μW driving power ($\approx$ 24 nm movements) leads to a strongly non-linear response similar to the path of the right facing arrows of the blue curve in Figure 7.1. We then estimate an on-

set of non-linearity for displacements on the order of 5 nm, which agrees with the expectation of non-linear response for vibrations on the order of the membrane thickness in nanoscale mechanical resonators [150, 164, 168].

With the capability to simultaneously measure PL spectra and drive suspended membranes into resonance, we attempt to cool our rf 'drum' to cryogenic temperatures where the excitonic emission becomes narrow and exhibits the rich spin and pseudospin physics described in earlier chapters. The mechanical resonance spectra for substrate temperatures from room temperature down to 130 K are presented in Figure 7.6a for a drive power of 30 μW. The higher temperature spectra with $f_{01} \approx 30$ MHz show a strongly non-linear response as evidenced by the instantaneous drop in $\Delta R/R$ as the drive passes the peak response frequency. In addition to a significant decrease in the membrane vibration amplitude, we find a strong blue-shift of f_{01} as the sample temperature decreases.

The inset to Figure 7.6a shows the extracted peak frequency (obtained without fitting) vs. temperature. Performing a linear fit (red line) to this temperature dependent peak frequency shift yields a zero-temperature intercept of 89 MHz and a red-shift of 0.21 MHz/K. Interestingly, if followed to higher temperatures, this indicates a zero-frequency resonance at 430 K, though the linear approximation will undoubtedly fail before then.

Unfortunately, the strong blue-shift with decreasing temperature limits the effective temperature range over which our AOMs can resonantly modulate the 523 nm beam. As the 60 MHz resonance frequency seen at a temperature of 130 K lies near the limit of our AOM driver capabilities, we leave an examination of TMD mechanical resonance at lower temperatures for future studies.

In Figure 7.6b we present the extracted $Q = \frac{f_{01}}{\Delta f_{01}}$ at each temperature, which shows a strong enhancement at low temperatures, consistent with measurements of suspended graphene [150]. Here, Δf_{01} is the fundamental resonance full width at half maximum (FWHM). The increase in Q by a factor of 7 over this temperature range likely results from 1) a reduction of incoherent vibrations as the phonon population decreases, 2) an increase in the resonance frequency f_{01}, and 3) a reduction in non-linear effects [150]. A larger Q for increasing resonance frequency is apparent as ($Q \propto f_{01}$). The reduced phonon population at lower temperatures effectively suppresses dissipation pathways of the moving membrane, allowing for longer oscillation periods and thereby reducing Δf_{01}. The increase in Q afforded by a reduction in non-linear effects is most easily seen by comparing the FWHM of the blue peak of Figure 7.1 with that of the red peak (assuming a low-to-high frequency

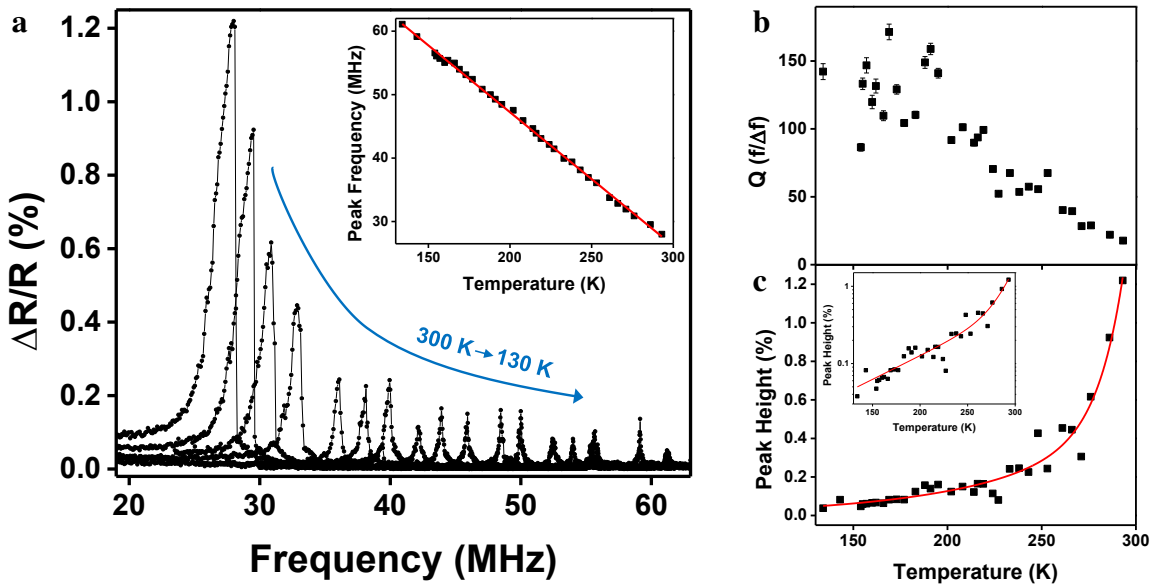

Figure 7.6: **a,** Percent change in reflected probe beam intensity vs. drive frequency for temperatures from 300 K to 130 K. The peak $\Delta R/R$ decreases and blue-shifts as temperature is lowered. Inset: Extracted peak resonance energies vs. sample temperature, showing a nearly linear response as indicated by the red line. Optical powers were maintained at 30 μW for the 532 nm drive and 100 μW for the 633 nm probe. **b,** Temperature dependence of the fundamental mode quality factor, Q. **c,** Height of the peak resonance vs. temperature (black data) with bi-exponential fit (red curve). Inset: Same plot on a semi-log scale to show the bi-exponential behavior.

sweep direction) . Since our experimental configuration limits us to driving frequency up-sweeps, a reduction in the non-linear response reduces the observed Δf_{01}.

The reduction in non-linear response for sample temperatures below 250 K directly stems from the measured drop in oscillation amplitude. The data in Figure 7.6c present the resonance peak height vs. temperature. The red line shows a bi-exponential fit to the data, with the form $3.4 \times 10^{-8} e^{(T-130K)/13.2K} + 4.7 \times 10^{-4} e^{(T-130K)/71.1K}$ where the relevant decay constants are then 13.2 K and 71.1 K. The inset to Fig 7.6c plots the response on a semi-log scale, more clearly showing the two decay rates. From the two extremes of the data shown here, we extract a range of estimated

oscillation amplitudes of 22 nm at room temperature down to 4 nm at 130 K. From the data in Figure 7.5, this is comparable to a 20x decrease in drive power.

The bi-exponential behavior of the peak $\Delta R/R$ intensity indicates that more than a simple stiffening of the crystal lattice may occur with cooling of the membrane, such as a combination of changes in the absorption of the 532 nm drive, changes in the reflectivity of the 633 nm probe, as well as stiffening of the crystal lattice. Greater tension within the crystal will cause the fixed driving power to yield smaller amplitude oscillations, while an increase in optical absorption will enhance the efficiency with which oscillations are drive. It is then possible that the decreasing temperatures will lead to a stiffening of the crystal, giving rise to a blue-shift of f_{01} and a reduction in the oscillation amplitude, while changes in the electronic band structure at lower temperatures may increase the absorption of the 532 nm excitation, effectively slowing the decay of the vibration amplitude. Changes in the optical absorption near the energy of the 633 nm probe will likewise directly affect the magnitude of the signal. The data in the inset to 7.6a support the conclusion that tension within the membrane continually grows as the continued up-shift in f_{01} with decreasing temperatures does not saturate within the temperature range explored. To obtain more concrete conclusions will require more thorough studies spanning a larger temperature range with varying pump/probe laser energies.

7.3 Conclusion

Initial measurements of ultrathin suspended TMD membranes presented here show non-linear behaviors characteristic of overdriven Duffing oscillators. By observing the asymmetric response arising from non-linearities in the restorative force, we determine an onset vibration amplitude of ≈ 5 nm. Temperature-dependent studies of driven membranes reveal strong blue-shifting of the fundamental resonance, f_{01}, as well as an increase in Q by almost an order of magnitude when cooling from 300 K to 130 K.

Future directions of this project include the pursuit of simultaneously driving monolayer TMD membranes into resonance at low temperatures (< 70 K) while monitoring the PL emission. Of special interest is an examination of the dependence of valley-dependent properties on the mechanical oscillation amplitude. Issues faced in these initial studies include the steep resonant frequency up-

shifting with decreasing temperature and an inability to detect optically driven vibrations in WSe_2 monolayers.

Overcoming the strong frequency shift merely lies in 1) modification of the experimental setup to include an AOM (or EOM) and detection photodiode with higher frequency capabilities, and/or 2) preparation of crystals suspended over larger voids. Since the resonant frequency of a suspended drumhead scales inversely with its diameter, obtaining membranes suspended over holes 2 to 3 times larger may down-shift the room-temperature resonant frequency enough so as to permit measurements below 70 K. However, the sharp increase in resonance frequency seen for decreasing membrane thickness will further exacerbate this issue in studies of monolayer TMDs [164].

In addition to high resonant frequencies, the difficulty in detecting resonantly-driven monolayer WSe_2 membranes may stem from a small optical cross-section for laser energies away from the excitonic transitions [169]. In the monolayer MoS_2 studies of Reference [164], a fortunate coincidence of the common 633 nm laser diode energy overlapping the 1.96 eV room-temperature excitonic energy likely aided in the detection of resonantly driven monolayer membranes. For WSe_2, similar studies may require a probe beam resonant with the excitonic transition, or at least another other optical transition with large oscillator strength.

As a system which enables optical fields and mechanical motion to interact with the valley pseudospin, suspended TMDs show promise for exciting studies in the field of nanomechanical membranes.

BIBLIOGRAPHY

[1] Wallace, P. R. The band theory of graphite. *Physical Review* **71**, 622–634 (1947).

[2] Novoselov, K. S. *et al.* Two-dimensional atomic crystals. *Proceedings of the National Academy of Sciences of the United States of America* **102**, 10451–10453 (2005). 0503533.

[3] Mak, K. F., Lee, C., Hone, J., Shan, J. & Heinz, T. F. Atomically Thin MoS2: A New Direct-Gap Semiconductor. *Physical Review Letters* **105**, 136805 (2010). URL http://link.aps.org/doi/10.1103/PhysRevLett.105.136805.

[4] Splendiani, A. *et al.* Emerging photoluminescence in monolayer MoS2. *Nano letters* **10**, 1271–5 (2010). URL http://www.ncbi.nlm.nih.gov/pubmed/20229981.

[5] Gong, Z. *et al.* Magnetoelectric effects and valley-controlled spin quantum gates in transition metal dichalcogenide bilayers. *Nature Communications* **4**, 15 (2013). URL http://arxiv.org/abs/1303.3932http://www.nature.com/doifinder/10.1038/ncomms3053.

[6] Xiao, D., Liu, G.-B., Feng, W., Xu, X. & Yao, W. Coupled Spin and Valley Physics in Monolayers of MoS2 and Other Group-VI Dichalcogenides. *Physical Review Letters* **108**, 196802 (2012). URL http://link.aps.org/doi/10.1103/PhysRevLett.108.196802.

[7] Ataca, C., Åđahin, H. & Ciraci, S. Stable, single-layer MX 2 transition-metal oxides and dichalcogenides in a honeycomb-like structure. *Journal of Physical Chemistry C* **116**, 8983–8999 (2012).

[8] Ross, J. S. *et al.* Electrical control of neutral and charged excitons in a monolayer semiconductor. *Nature communications* **4**, 1474 (2013). URL http://dx.doi.org/10.1038/ncomms2498.

[9] Jones, A. M. *et al.* Optical generation of excitonic valley coherence in monolayer WSe2. *Nature nanotechnology* **8**, 634–8 (2013). URL http://dx.doi.org/10.1038/nnano.2013.151.

[10] Li, T. & Galli, G. Electronic properties of MoS 2 nanoparticles. *Journal of Physical Chemistry C* **111**, 16192–16196 (2007).

[11] Lebègue, S. & Eriksson, O. Electronic structure of two-dimensional crystals from ab initio theory. *Physical Review B - Condensed Matter and Materials Physics* **79** (2009). arXiv:0901.0440v1.

[12] Zhu, Z. Y., Cheng, Y. C. & Schwingenschlögl, U. Giant spin-orbit-induced spin splitting in two-dimensional transition-metal dichalcogenide semiconductors. *Physical Review B - Condensed Matter and Materials Physics* **84** (2011).

[13] Bonaccorso, F. *et al.* Graphene, related two-dimensional crystals, and hybrid systems for energy conversion and storage. *Science* **347**, 1246501–1246501 (2015). URL http://www.sciencemag.org/cgi/doi/10.1126/science.1246501.

[14] Geim, a. K. & Grigorieva, I. V. Van der Waals heterostructures. *Nature* **499**, 419–25 (2013). URL http://www.ncbi.nlm.nih.gov/pubmed/23887427. 1307.6718.

[15] Sundaram, R. S. *et al.* Electroluminescence in single layer MoS2. *Nano Letters* **13**, 1416–1421 (2013). 1211.4311.

[16] Pospischil, A., Furchi, M. M. & Mueller, T. Solar-energy conversion and light emission in an atomic monolayer p-n diode. *Nature nanotechnology* **9**, 257–61 (2014). URL http://www.ncbi.nlm.nih.gov/pubmed/24608229. 1309.7492.

[17] Ross, J. S. *et al.* Electrically tunable excitonic light-emitting diodes based on monolayer WSe2 p-n junctions. *Nature nanotechnology* **9**, 268–72 (2014). URL http://www.ncbi.nlm.nih.gov/pubmed/24608230. 1312.1435.

[18] Baugher, B. W. H., Churchill, H. O. H., Yang, Y. & Jarillo-Herrero, P. Optoelectronic devices based on electrically tunable p-n diodes in a monolayer dichalcogenide. *Nature nanotechnology* **9**, 262–7 (2014). URL http://www.ncbi.nlm.nih.gov/pubmed/24608231. 1310.0452.

[19] Gunawan, O., Habib, B., De Poortere, E. P. & Shayegan, M. Quantized conductance in an AlAs two-dimensional electron system quantum point contact. *Physical Review B* **74** (2006).

[20] Rycerz, A., Tworzydlo, J. & Beenakker, C. W. J. Valley filter and valley valve in graphene. *Nature Physics* **3**, 172 – 175 (2007). URL http://arxiv.org/abs/cond-mat/0608533. 0608533.

[21] Xiao, D., Yao, W. & Niu, Q. Valley-contrasting physics in graphene: Magnetic moment and topological transport. *Physical Review Letters* **99** (2007). 0709.1274.

[22] Yao, W., Xiao, D. & Niu, Q. Valley-dependent optoelectronics from inversion symmetry breaking. *Physical Review B* **77** (2008).

[23] Bishop, N. C. *et al.* Valley polarization and susceptibility of composite fermions around a filling factor ν=32. *Physical Review Letters* **98** (2007). 0706.1195.

[24] Shkolnikov, Y. P., De Poortere, E. P., Tutuc, E. & Shayegan, M. Valley splitting of AlAs two-dimensional electrons in a perpendicular magnetic field. *Physical review letters* **89**, 226805 (2002). 0207431.

[25] Liu, G.-B., Shan, W.-Y., Yao, Y., Yao, W. & Xiao, D. Three-band tight-binding model for monolayers of group-VIB transition metal dichalcogenides. *Physical Review B* **88**, 085433 (2013). URL http://prb.aps.org/abstract/PRB/v88/i8/e085433http://link.aps.org/doi/10.1103/PhysRevB.88.085433.

[26] Kormányos, A. *et al.* Monolayer MoS2: Trigonal warping, the Γ valley, and spin-orbit coupling effects. *Physical Review B* **88** (2013).

[27] Liu, G.-B., Xiao, D., Yao, Y., Xu, X. & Yao, W. Electronic structures and theoretical modelling of two-dimensional group-VIB transition metal dichalcogenides. *Chem. Soc. Rev.* (2015). URL http://xlink.rsc.org/?DOI=C4CS00301B.

[28] Zeng, H. & Cui, X. An optical spectroscopic study on twodimensional group-VI transition metal dichalcogenides. *Chemical Society Reviews* **44**, 2629 (2015). URL http://dx.doi.org/10.1039/C4CS00265B.

[29] Mattheiss, L. F. Band structures of transition-metal-dichalcogenide layer compounds. *Physical Review B* **8**, 3719–3740 (1973).

[30] Wilson, J. & Yoffe, A. The transition metal dichalcogenides discussion and interpretation of the observed optical, electrical and structural properties. *Advances in Physics* **18**, 193–335 (1969).

[31] Kumar, A. & Ahluwalia, P. K. Electronic structure of transition metal dichalcogenides monolayers 1H-MX2 (M = Mo, W; X = S, Se, Te) from ab-initio theory: new direct band gap semiconductors. *The European Physical Journal B* **85** (2012).

[32] Ramasubramaniam, A. Large excitonic effects in monolayers of molybdenum and tungsten dichalcogenides. *Physical Review B* **86** (2012).

[33] Kumar, A. & Ahluwalia, P. K. Tunable dielectric response of transition metals dichalcogenides MX2 (M=Mo, W; X=S, Se, Te): Effect of quantum confinement. *Physica B: Condensed Matter* **407**, 4627–4634 (2012).

[34] Berkelbach, T. C., Hybertsen, M. S. & Reichman, D. R. Theory of neutral and charged excitons in monolayer transition metal dichalcogenides. *Physical Review B* **88** (2013). 1305.4972.

[35] Consadori, F. & Frindt, R. F. Crystal size effects on the exciton absorption spectrum of WSe2. *Physical Review B* **2**, 4893–4896 (1970).

[36] Chernikov, A. *et al.* Exciton Binding Energy and Nonhydrogenic Rydberg Series in Monolayer WS2. *Physical Review Letters* **113**, 076802 (2014). URL http://link.aps.org/doi/10.1103/PhysRevLett.113.076802. arXiv:1403.4270v3.

[37] Ye, Z. *et al.* Probing Excitonic Dark States in Single-layer Tungsten Disulfide. *Nature* **5**, 214–218 (2014). URL http://arxiv.org/abs/1403.5568. 1403.5568.

[38] Zhu, B., Chen, X. & Cui, X. Exciton Binding Energy of Monolayer WS2. *Scientific reports* **5**, 9218 (2015). URL http://www.nature.com/srep/2015/150318/srep09218/full/srep09218.html. 1403.5108.

[39] He, K. *et al.* Tightly bound excitons in monolayer WSe2. *Physical Review Letters* **113** (2014).

[40] Ugeda, M. M. *et al.* Giant bandgap renormalization and excitonic effects in a monolayer transition metal dichalcogenide semiconductor. *Nature materials* **13**, 1091–1095 (2014). URL http://arxiv.org/abs/1404.2331. 1404.2331.

[41] Mak, K. F. *et al.* Tightly bound trions in monolayer MoS2. *Nature materials* **12**, 207–11 (2013). URL http://www.ncbi.nlm.nih.gov/pubmed/23202371. 1210.8226.

[42] Lin, Y. *et al.* Dielectric Screening of Excitons and Trions in Single-Layer MoS2. *Nano Letters* **14**, 5569–5576 (2014). URL http://pubs.acs.org/doi/abs/10.1021/nl501988y.

[43] Jorio, A., Dresselhaus, G. & Dresselhaus, M. S. *Carbon Nanotubes: Advanced Topics in the Synthesis, Structure, Properties and Applications*, vol. 111 (Springer-Verlag Berlin Heidelberg, 2008). URL http://doi.wiley.com/10.1002/anie.200385171.

[44] Song, Y. & Dery, H. Transport theory of monolayer transition-metal dichalcogenides through symmetry. *Physical Review Letters* **111** (2013). 1302.3627.

[45] Wang, Q. H., Kalantar-Zadeh, K., Kis, A., Coleman, J. N. & Strano, M. S. Electronics and optoelectronics of two-dimensional transition metal dichalcogenides. *Nature nanotechnology* **7**, 699–712 (2012). URL http://www.ncbi.nlm.nih.gov/pubmed/23132225.

[46] Jariwala, D., Sangwan, V. K., Lauhon, L. J., Marks, T. J. & Hersam, M. C. Emerging device applications for semiconducting two-dimensional transition metal dichalcogenides. *ACS Nano* **8**, 1102–1120 (2014). 1402.0047.

[47] Kappera, R. *et al.* Phase-engineered low-resistance contacts for ultrathin MoS2 transistors. *Nature materials* **13**, 1128–1134 (2014).

[48] Wang, L. *et al.* One-dimensional electrical contact to a two-dimensional material. *Science* **342**, 614–7 (2013). URL http://www.ncbi.nlm.nih.gov/pubmed/24179223.

[49] Wang, H., Yuan, H., Sae Hong, S., Li, Y. & Cui, Y. Physical and chemical tuning of two-dimensional transition metal dichalcogenides. *Chem. Soc. Rev.* (2015). URL http://xlink.rsc.org/?DOI=C4CS00287C.

[50] Xu, H., Fathipour, S., Kinder, E. W., Seabaugh, A. C. & Fullerton-Shirey, S. K. Reconfigurable Ion Gating of 2H-MoTe 2 Field-Effect Transistors Using Poly(ethylene oxide)-CsClO 4 Solid Polymer Electrolyte. *ACS Nano* 150424083314009 (2015). URL http://pubs.acs.org/doi/abs/10.1021/nn506521p.

[51] Ye, J. T. *et al.* Superconducting dome in a gate-tuned band insulator. *Science* **338**, 1193–6 (2012). URL http://www.ncbi.nlm.nih.gov/pubmed/23197529.

[52] Mak, K. F., McGill, K. L., Park, J. & McEuen, P. L. Valleytronics. The valley Hall effect in MoS2 transistors. *Science* **344**, 1489–92 (2014). URL http://www.ncbi.nlm.nih.gov/pubmed/24970080. 1403.5039.

[53] Mak, K. F., He, K., Shan, J. & Heinz, T. F. Control of valley polarization in monolayer MoS2 by optical helicity. *Nature nanotechnology* **7**, 494–8 (2012). URL http://www.ncbi.nlm.nih.gov/pubmed/22706698.

[54] Kozawa, D. *et al.* Photocarrier relaxation pathway in two-dimensional semiconducting transition metal dichalcogenides. *Nature communications* **5**, 4543 (2014). URL http://www.ncbi.nlm.nih.gov/pubmed/25072556.

[55] Coehoorn, R., Haas, C. & De Groot, R. A. Electronic structure of MoSe2, MoS2, and WSe2. II. The nature of the optical band gaps. *Physical Review B* **35**, 6203–6206 (1987).

[56] Finteis, T. *et al.* Occupied and unoccupied electronic band structure of WSe2. *Physical Review B* **55**, 10400–10411 (1997).

[57] Alidoust, N., Bian, G. & Xu, S. Observation of monolayer valence band spin-orbit effect and induced quantum well states in MoX2. *Nature Communications* **5** (2014). URL http://www.nature.com/ncomms/2014/140822/ncomms5673/full/ncomms5673.html. 1312.7631.

[58] Riley, J. M. *et al.* Direct observation of spin-polarized bulk in an semiconductor bulk inversion-symmetric. *Nature Physics* **10**, 835–839 (2014).

[59] Le, D. *et al.* Spin-orbit coupling in the band structure of monolayer WSe2. *Journal of Physics: Condensed Matter* **27**, 182201 (2015). URL http://stacks.iop.org/0953-8984/27/i=18/a=182201?key=crossref.9afef45ca37b4ce9230a36795c6330a3.

[60] Cheiwchanchamnangij, T. & Lambrecht, W. R. L. Quasiparticle band structure calculation of monolayer, bilayer, and bulk MoS 2. *Physical Review B* **85** (2012).

[61] Ochoa, H. & Roldán, R. Spin-Orbit mediated spin relaxation in monolayer MoS2. *Cond-mat* **87**, 245421 (2013). 1303.5860.

[62] Cao, T. *et al.* Valley-selective circular dichroism of monolayer molybdenum disulphide. *Nature communications* **3**, 887 (2012). URL http://www.ncbi.nlm.nih.gov/pubmed/22673914.

[63] Zeng, H., Dai, J., Yao, W., Xiao, D. & Cui, X. Valley polarization in MoS2 monolayers by optical pumping. *Nature nanotechnology* **7**, 490–3 (2012). URL http://www.ncbi.nlm.nih.gov/pubmed/22706701.

[64] Li, Y. *et al.* Valley Splitting and Polarization by the Zeeman Effect in Monolayer MoSe2. *Physical Review Letters* **113** (2014). URL http://link.aps.org/doi/10.1103/PhysRevLett.113.266804.

[65] Mai, C. *et al.* Many-body effects in valleytronics: Direct measurement of valley lifetimes in single-layer MoS2. *Nano Letters* **14**, 202–206 (2014).

[66] Wang, G. *et al.* Valley dynamics probed through charged and neutral exciton emission in monolayer WS2. *Physical Review B* **90**, 075413 (2014). URL http://link.aps.org/doi/10.1103/PhysRevB.90.075413http://arxiv.org/abs/1402.6009. 1402.6009.

[67] Wang, Q. *et al.* Valley carrier dynamics in monolayer molybdenum disulfide from helicity-resolved ultrafast pump-probe spectroscopy. *ACS Nano* **7**, 11087–11093 (2013).

[68] Mai, C. *et al.* Exciton valley relaxation in a single layer of WS2 measured by ultrafast spectroscopy. *Physical Review B* **90** (2014).

[69] Plechinger, G., Nagler, P., Schüller & Korn, T. Time-resolved Kerr rotation spectroscopy of valley dynamics in single-layer MoS2. *arxiv* 1–6 (2014). URL http://arxiv.org/abs/1404.7674. 1404.7674.

[70] Glazov, M. M. *et al.* Exciton fine structure and spin decoherence in monolayers of transition metal dichalcogenides. *Physical Review B* **89** (2014). 1403.0108.

[71] Yu, H., Liu, G.-B., Gong, P., Xu, X. & Yao, W. Dirac cones and Dirac saddle points of bright excitons in monolayer transition metal dichalcogenides. *Nature communications* **5**, 3876 (2014). URL http://www.ncbi.nlm.nih.gov/pubmed/24821438. 1401.0667.

[72] Yu, T. & Wu, M. W. Valley depolarization due to intervalley and intravalley electron-hole exchange interactions in monolayer MoS2. *Physical Review B* **89** (2014). arXiv:1401.0047v3.

[73] Novoselov, K. S. *et al.* Electric field effect in atomically thin carbon films. *Science* **306**, 666–9 (2004). URL http://www.sciencemag.org/content/306/5696/666.full.

[74] Chhowalla, M. *et al.* The chemistry of two-dimensional layered transition metal dichalcogenide nanosheets. *Nature chemistry* **5**, 263–75 (2013). URL http://www.ncbi.nlm.nih.gov/pubmed/23511414.

[75] Benameur, M. M. *et al.* Visibility of dichalcogenide nanolayers. *Nanotechnology* **22**, 125706 (2011). 1006.1048.

[76] Kumar, N. *et al.* Second harmonic microscopy of monolayer MoS2. *Physical Review B* **87**, 161403 (2013). URL http://link.aps.org/doi/10.1103/PhysRevB.87.161403. 1302.3935.

[77] Zeng, H. *et al.* Optical signature of symmetry variations and spin-valley coupling in atomically thin tungsten dichalcogenides. *Scientific reports* **3**, 1608 (2013). URL http://www.pubmedcentral.nih.gov/articlerender.fcgi?artid=3622914&tool=pmcentrez&rendertype=abstract.

[78] Malard, L. M., Alencar, T. V., Barboza, A. P. M., Mak, K. F. & de Paula, A. M. Observation of intense second harmonic generation from MoS2 atomic crystals. *Physical Review B* **87**, 201401 (2013). URL http://link.aps.org/doi/10.1103/PhysRevB.87.201401.

[79] Arora, A. *et al.* Excitonic resonances in thin films of WSe2: From monolayer to bulk material. *arxiv* (2015). 1503.01682.

[80] He, Y., Clark, G., Schaibley, J. & He, Y. Single Quantum Emitters in Monolayer Semiconductors. *Nature nanotechnology* in press (2015). URL http://arxiv.org/abs/1411.2449. 1411.2449.

[81] Zhao, W. *et al.* Evolution of electronic structure in atomically thin sheets of WS2 and WSe2. *ACS Nano* **7**, 791–797 (2013).

[82] Hanbicki, A. T., Currie, M., Kioseoglou, G., Friedman, A. L. & Jonker, B. T. Measurement of high exciton binding energy in the monolayer transition-metal dichalcogenides WS2 and WSe2. *Solid State Communications* **203**, 16–20 (2015). 1412.2156.

[83] Yankowitz, M., McKenzie, D. & LeRoy, B. J. Local Spectroscopic Characterization of Spin and Layer Polarization in WSe2. *arxiv* (2015). URL http://arxiv.org/abs/1505.00245. 1505.00245.

[84] Chow, P. K. *et al.* Defect-Induced Photoluminescence in Monolayer Semiconducting Transition Metal Dichalcogenides. *ACS Nano* **9**, 1520–1527 (2015).

[85] Ganchev, B., Drummond, N., Aleiner, I. & FalâĂŹko, V. Three-Particle Complexes in Two-Dimensional Semiconductors. *Physical Review Letters* **114** (2015). URL http://link.aps.org/doi/10.1103/PhysRevLett.114.107401.

[86] Xu, X., Yao, W., Xiao, D. & Heinz, T. F. Spin and pseudospins in layered transition metal dichalcogenides. *Nature Physics* **10**, 343–350 (2014). URL http://dx.doi.org/10.1038/nphys2942.

[87] Wang, G. *et al.* Polarization and time-resolved photoluminescence spectroscopy of excitons in MoSe2 monolayers. *Applied Physics Letters* **106**, 112101 (2015). URL http://scitation.aip.org/content/aip/journal/apl/106/11/10.1063/1.4916089.

[88] Tongay, S. *et al.* Defects activated photoluminescence in two-dimensional semiconductors: interplay between bound, charged, and free excitons. *Scientific reports* **3**, 2657 (2013). URL http://www.nature.com/srep/2013/130913/srep02657/full/srep02657.html.

[89] Wiesner, S. Conjugate coding (1983).

[90] Maialle, M. Z., De Andrada E Silva, E. A. & Sham, L. J. Exciton spin dynamics in quantum wells. *Physical Review B* **47**, 15776–15788 (1993).

[91] PIKUS, G. & BIR, G. EXCHANGE INTERACTION IN BOUND EXCITONS IN SEMICONDUCTORS. *SOVIET PHYSICS JETP-USSR* **35**, 174–& (1972). URL http://apps.webofknowledge.com/full_record.do?product=WOS&search_mode=GeneralSearch&qid=1&SID=1DlTA1UOXOq92ejnGEl&page=1&doc=3&cacheurlFromRightClick=no.

[92] Feng, J., Qian, X., Huang, C. & Li, J. Strain-engineered artificial atom as a broad-spectrum solar energy funnel. *Nature Photonics* **6**, 866–872 (2012). URL http://www.nature.com/nphoton/journal/v6/n12/abs/nphoton.2012.285.html.

[93] Qiu, D. Y., Da Jornada, F. H. & Louie, S. G. Optical spectrum of MoS2: Many-body effects and diversity of exciton states. *Physical Review Letters* **111**, 216805 (2013).

[94] Misewich, J. A. *et al.* Electrically induced optical emission from a carbon nanotube FET. *Science* **300**, 783–6 (2003). URL http://www.ncbi.nlm.nih.gov/pubmed/12730598.

[95] Lefebvre, J., Fraser, J., Finnie, P. & Homma, Y. Photoluminescence from an individual single-walled carbon nanotube. *Physical Review B* **69**, 075403 (2004). URL http://link.aps.org/doi/10.1103/PhysRevB.69.075403.

[96] Bayer, M. *et al.* Electron and Hole g Factors and Exchange Interaction from Studies of the Exciton Fine Structure in In0.60Ga0.40As Quantum Dots. *Physical Review Letters* **82**, 1748–1751 (1999). URL http://link.aps.org/doi/10.1103/PhysRevLett.82.1748.

[97] Delay, M. Practical Aspects of Mirror Usage in Optical Systems for Biology - Part 1. *Semrock Inc.* 17. URL http://www.semrock.com/data/sites/1/semrockpdfs/Practical_aspects_of_mirror_usage_in_optical_systems_for_biology_part1.pdf.

[98] Predrag Cvitanović. *Group Theory: Birdtracks, Lie's, and Exceptional Groups* (Princeton University Press, 2008).

[99] Jones, A. M. *et al.* Spin-layer locking effects in optical orientation of exciton spin in bilayer WSe2. *Nature Physics* **10**, 130–134 (2014). URL http://dx.doi.org/10.1038/nphys2848.

[100] Liu, G.-B. unpublished work.

[101] Wu, S. *et al.* Electrical tuning of valley magnetic moment through symmetry control in bilayer MoS2. *Nature Physics* (2013). URL http://www.nature.com/doifinder/10.1038/nphys2524.

[102] Schuegraf, K., Park, D. & Hu, C. Reliability of thin SiO 2 at direct-tunneling voltages. *Electron Devices Meeting, 1994* 609–612 (1994). URL http://ieeexplore.ieee.org/xpls/abs_all.jsp?arnumber=383336.

[103] Miller, D. *et al.* Band-Edge Electroabsorption in Quantum Well Structures: The Quantum-Confined Stark Effect. *Physical Review Letters* **53**, 2173–2176 (1984). URL http://link.aps.org/doi/10.1103/PhysRevLett.53.2173.

[104] Zhang, X., Liu, Q., Luo, J.-W., Freeman, A. J. & Zunger, A. Hidden spin polarization in inversion-symmetric bulk crystals. *Nature Physics* **10**, 387–393 (2014). URL http://dx.doi.org/10.1038/nphys2933. 1402.4446.

[105] Komsa, H. P. & Krasheninnikov, A. V. Effects of confinement and environment on the electronic structure and exciton binding energy of MoS2 from first principles. *Physical Review B* **86** (2012).

[106] Liang, Y., Huang, S., Soklaski, R. & Yang, L. Quasiparticle band-edge energy and band offsets of monolayer of molybdenum and tungsten chalcogenides. *Applied Physics Letters* **103** (2013). 1306.0620.

[107] Wang, G. *et al.* Giant Enhancement of the Optical Second-Harmonic Emission of WSe2 Monolayers by Laser Excitation at Exciton Resonances. *Physical Review Letters* **114** (2015). URL http://link.aps.org/doi/10.1103/PhysRevLett.114.097403.

[108] Tonndorf, P. *et al.* Photoluminescence emission and Raman response of monolayer MoS2, MoSe2, and WSe2. *Optics express* **21**, 4908–4916 (2013). arXiv:1208.5864.

[109] Zhao, W. *et al.* Lattice dynamics in mono- and few-layer sheets of WS2 and WSe2. *Nanoscale* **5**, 9677–83 (2013). URL http://www.ncbi.nlm.nih.gov/pubmed/23999910. 1304.0911.

[110] Lu, X. *et al.* Large-area synthesis of monolayer and few-layer MoSe2 films on SiO2 substrates. *Nano Letters* **14**, 2419–2425 (2014).

[111] Zhang, X. *et al.* Phonon and Raman scattering of two-dimensional transition metal dichalcogenides from monolayer, multilayer to bulk material. *Chem. Soc. Rev.* **44**, 2757–2785 (2015). URL http://xlink.rsc.org/?DOI=C4CS00282B.

[112] Mitioglu, A. A. *et al.* Optical manipulation of the exciton charge state in single-layer tungsten disulfide. *Physical Review B* **88** (2013).

[113] Peimyoo, N. *et al.* Chemically Driven Tunable Light Emission of Charged and Neutral Excitons in Monolayer WS 2. *ACS Nano* **8**, 11320–11329 (2014). URL http://pubs.acs.org/doi/abs/10.1021/nn504196n.

[114] Mouri, S., Miyauchi, Y. & Matsuda, K. Tunable photoluminescence of monolayer MoS2 via chemical doping. *Nano Letters* **13**, 5944–5948 (2013). 1308.3564.

[115] Plechinger, G. *et al.* A direct comparison of CVD-grown and exfoliated MoS2 using optical spectroscopy. *Phys. Rev. Lett* 1–7 (2013). URL http://arxiv.org/abs/1310.8470. 1310.8470.

[116] Sercombe, D. *et al.* Optical investigation of the natural electron doping in thin MoS2 films deposited on dielectric substrates. *Scientific reports* **3**, 3489 (2013). URL http://www.pubmedcentral.nih.gov/articlerender.fcgi?artid=3860010&tool=pmcentrez&rendertype=abstract. 1304.7221.

[117] Buscema, M., Steele, G. A., van der Zant, H. S. J. & Castellanos-Gomez, A. The effect of the substrate on the Raman and photoluminescence emission of single-layer MoS2 (2014). 1311.3869.

[118] Lopez-Sanchez, O. *et al.* Light generation and harvesting in a van der waals heterostructure. *ACS Nano* **8**, 3042–3048 (2014). 1403.2743.

[119] Soklaski, R., Liang, Y. & Yang, L. Temperature effect on optical spectra of monolayer molybdenum disulfide. *Applied Physics Letters* **104**, 193110 (2014).

[120] Scheuschner, N. *et al.* Photoluminescence of freestanding single- and few-layer MoS2. *Physical Review B* **89**, 125406 (2014). 1311.5824.

[121] Zhang, C., Wang, H., Chan, W., Manolatou, C. & Rana, F. Absorption of light by excitons and trions in monolayers of metal dichalcogenide Mo S2: Experiments and theory. *Physical Review B* **89** (2014). 1402.0263.

[122] Thilagam, A. Excitonic polarons in low-dimensional transition metal dichalcogenides. *Physica B: Condensed Matter* **464**, 44–50 (2015). URL http://linkinghub.elsevier.com/retrieve/pii/S092145261500099X.

[123] Wilson, T., Wilson, T., Tan, J. B. & Tan, J. B. Finite sized coherent and incoherent detectors in confocal microscopy. *Engineering* **182**, 61–66 (1996).

[124] Wilson, T., Török, P. & Higdon, P. D. The effect of detector size on the signal-to-noise ratio in confocal polarized light microscopy. *Journal of Microscopy* **189**, 12–14 (1998).

[125] Shribak, M., Inoue, S. & Oldenbourg, R. Polarization aberrations caused by differential transmission and phase shift in high-numerical-aperture lenses: theory, measurement, and rectification. *Optical Engineering* **41**, 943 (2002).

[126] Plentz, F., Ribeiro, H. B., Jorio, A., Strano, M. S. & Pimenta, M. A. Direct experimental evidence of exciton-phonon bound states in carbon nanotubes. *Physical Review Letters* **95** (2005).

[127] Chen, S.-Y., Zheng, C., Fuhrer, M. S. & Yan, J. Helicity resolved Raman scattering of MoS2, MoSe2, WS2 and WSe2 atomic layers. *Nano Letters* 150226172813004 (2015). URL http://pubs.acs.org/doi/abs/10.1021/acs.nanolett.5b00092.

[128] Rivera, P. *et al.* Observation of long-lived interlayer excitons in monolayer MoSe2-WSe2 heterostructures. *Nature Communications* **6**, 6242 (2015). URL http://www.nature.com/doifinder/10.1038/ncomms7242.

[129] Dean, C. R. *et al.* Boron nitride substrates for high-quality graphene electronics. *Nature nanotechnology* **5**, 722–726 (2010). 1005.4917.

[130] Eck, T. G., Foldy, L. L. & Wieder, H. Observation of "anticrossings" in optical resonance fluorescence. *Physical Review Letters* **10**, 239–242 (1963).

[131] Hanle, I. & Kleinpoppen, H. *Progress in Atomic Spectroscopy*, vol. Part A - D (Springer US, 1978).

[132] Pringsheim, P. Bemerkungen über den Unterschied von Lumineszenz- und Temperaturstrahlung. *Zeitschrift für Physik* **57**, 739–746 (1929).

[133] Epstein, R. I. *et al.* Observation of laser-induced fluorescent cooling of a solid. *Nature* **377**, 500–503 (1995).

[134] Seletskiy, D. V. *et al.* Laser cooling of solids to cryogenic temperatures. *Nature Photonics* **4**, 161–164 (2010).

[135] Seletskiy, D. V. *et al.* Local laser cooling of Yb:YLF to 110 K. *Optics express* **19**, 18229–36 (2011). URL http://www.ncbi.nlm.nih.gov/pubmed/23035009.

[136] Zhang, J., Li, D., Chen, R. & Xiong, Q. Laser cooling of a semiconductor by 40 kelvin. *Nature* **493**, 504–8 (2013). URL http://www.ncbi.nlm.nih.gov/pubmed/23344360.

[137] Eshlaghi, S., Worthoff, W., Wieck, A. D. & Suter, D. Luminescence upconversion in GaAs quantum wells. *Physical Review B* **77**, 245317 (2008).

[138] Shang, J. *et al.* Observation of Excitonic Fine Structure in a 2D Transition-Metal Dichalcogenide Semiconductor. *ACS Nano* **9**, 647–655 (2015). URL http://pubs.acs.org/doi/abs/10.1021/nn5059908.

[139] Brumme, T., Calandra, M. & Mauri, F. First-principles theory of field-effect doping in transition-metal dichalcogenides: Structural properties, electronic structure, Hall coefficient, and electrical conductivity. *Physical Review B* **91**, 155436 (2015).

[140] Zhao, W. *et al.* Origin of indirect optical transitions in few-layer MoS2, WS2, and WSe2. *Nano Letters* **13**, 5627–5634 (2013). 1309.0923.

[141] Allain, A. & Kis, A. Electron and hole mobilities in single-layer WSe2. *ACS Nano* **8**, 7180–7185 (2014).

[142] You, Y. *et al.* Observation of biexcitons in monolayer WSe2. *Nature Physics* (2015). URL http://www.nature.com/doifinder/10.1038/nphys3324.

[143] Combescot, M. & Betbeder-Matibet, O. Biexciton oscillator strength. *Physical Review B* **80** (2009). 0910.3051.

[144] Calcagnile, L. *et al.* Excitonic and biexcitonic recombination in undoped and modulation-doped Zn1-xCdxSe/ZnSe quantum-well structures. *Physical Review B* **55**, R13413–R13416 (1997).

[145] Zou, W., Visser, C., Maduro, J. A., Pshenichnikov, M. S. & Hummelen, J. C. Broadband dye-sensitized upconversion of near-infrared light. *Nature Photonics* **6**, 560–564 (2012).

[146] Feng, X. L., White, C. J., Hajimiri, A. & Roukes, M. L. A self-sustaining ultrahigh-frequency nanoelectromechanical oscillator. *Nature nanotechnology* **3**, 342–346 (2008).

[147] Chen, C. *et al.* Graphene mechanical oscillators with tunable frequency. *Nature nanotechnology* **8**, 923–7 (2013). URL http://www.ncbi.nlm.nih.gov/pubmed/24240431.

[148] Roukes, M. Plenty of room, indeed. *Scientific American* **285**, 48–51, 54–57 (2001).

[149] Sazonova, V. *et al.* A tunable carbon nanotube electromechanical oscillator. *Nature* **431**, 284–287 (2004). 0409407.

[150] Bunch, J. S. *et al.* Electromechanical resonators from graphene sheets. *Science* **315**, 490–493 (2007). 33846627756.

[151] Chiu, H. Y., Hung, P., Postma, H. W. C. & Bockrath, M. Atomic-scale mass sensing using carbon nanotube resonators. *Nano Letters* **8**, 4342–4346 (2008).

[152] Jensen, K., Kim, K. & Zettl, A. An atomic-resolution nanomechanical mass sensor. *Nature nanotechnology* **3**, 533–537 (2008). 0809.2126.

[153] He, R., Feng, X. L., Roukes, M. L. & Yang, P. Self-transducing silicon nanowire electromechanical systems at room temperature. *Nano Letters* **8**, 1756–1761 (2008).

[154] Lassagne, B., Tarakanov, Y., Kinaret, J., Garcia-Sanchez, D. & Bachtold, A. Coupling mechanics to charge transport in carbon nanotube mechanical resonators. *Science* **325**, 1107–1110 (2009).

[155] Hüttel, A. K. *et al.* Carbon nanotubes as ultrahigh quality factor mechanical resonators. *Nano Letters* **9**, 2547–2552 (2009). 0907.2823.

[156] Chen, C. *et al.* Performance of monolayer graphene nanomechanical resonators with electrical readout. *Nature nanotechnology* **4**, 861–867 (2009). 0907.3721.

[157] Eichler, A. *et al.* Nonlinear damping in mechanical resonators made from carbon nanotubes and graphene. *Nature nanotechnology* **6**, 339–342 (2011). 1103.1788.

[158] Knobel, R. G. & Cleland, A. N. Nanometre-scale displacement sensing using a single electron transistor. *Nature* **424**, 291–293 (2003).

[159] LaHaye, M. D., Buu, O., Camarota, B. & Schwab, K. C. Approaching the quantum limit of a nanomechanical resonator. *Science* **304**, 74–77 (2004).

[160] Lee, C., Wei, X., Kysar, J. W. & Hone, J. Measurement of the elastic properties and intrinsic strength of monolayer graphene. *Science* **321**, 385–388 (2008). 47749150628.

[161] Withers, F. *et al.* Light-emitting diodes by band-structure engineering in van der Waals heterostructures. *Nature Materials* **14**, 301–306 (2015). URL http://www.nature.com/doifinder/10.1038/nmat4205.

[162] Zandiatashbar, A. *et al.* Effect of defects on the intrinsic strength and stiffness of graphene. *Nature communications* **5**, 3186 (2014). URL http://www.ncbi.nlm.nih.gov/pubmed/24458268.

[163] Lien, D.-H. *et al.* Engineering Light Outcoupling in 2D Materials. *Nano Letters* **15**, 1356–1361 (2015). URL http://pubs.acs.org/doi/abs/10.1021/nl504632u.

[164] Castellanos-Gomez, A. *et al.* Single-layer MoS2 mechanical resonators. *Advanced Materials* **25**, 6719–6723 (2013). 1310.2134.

[165] Wah, T. Vibration of Circular Plates. *The Journal of the Acoustical Society of America* **34**, 275 (1962).

[166] Lojek, B. Reflectivity of the silicon semiconductor substrate and its dependence on the doping concentration and intensity of the irradiation. In *11th IEEE International Conference on Advanced Thermal Processing of Semiconductors. RTP 2003* (2003).

[167] Eda, G. *et al.* Photoluminescence from chemically exfoliated MoS 2. *Nano Letters* **11**, 5111–5116 (2011).

[168] Song, X. *et al.* Stamp transferred suspended graphene mechanical resonators for radio frequency electrical readout. *Nano Letters* **12**, 198–202 (2012). 1203.0764.

[169] Li, Y. *et al.* Measurement of the optical dielectric function of monolayer transition-metal dichalcogenides: MoS2, MoSe2, WS2, and WSe2. *Physical Review B* **90** (2014). URL http://link.aps.org/doi/10.1103/PhysRevB.90.205422.

Appendix A

COMPLETE SET OF MONOLAYER WSE_2 POLARIZATION-RESOLVED PHOTOLUMINESCENCE SPECTRA

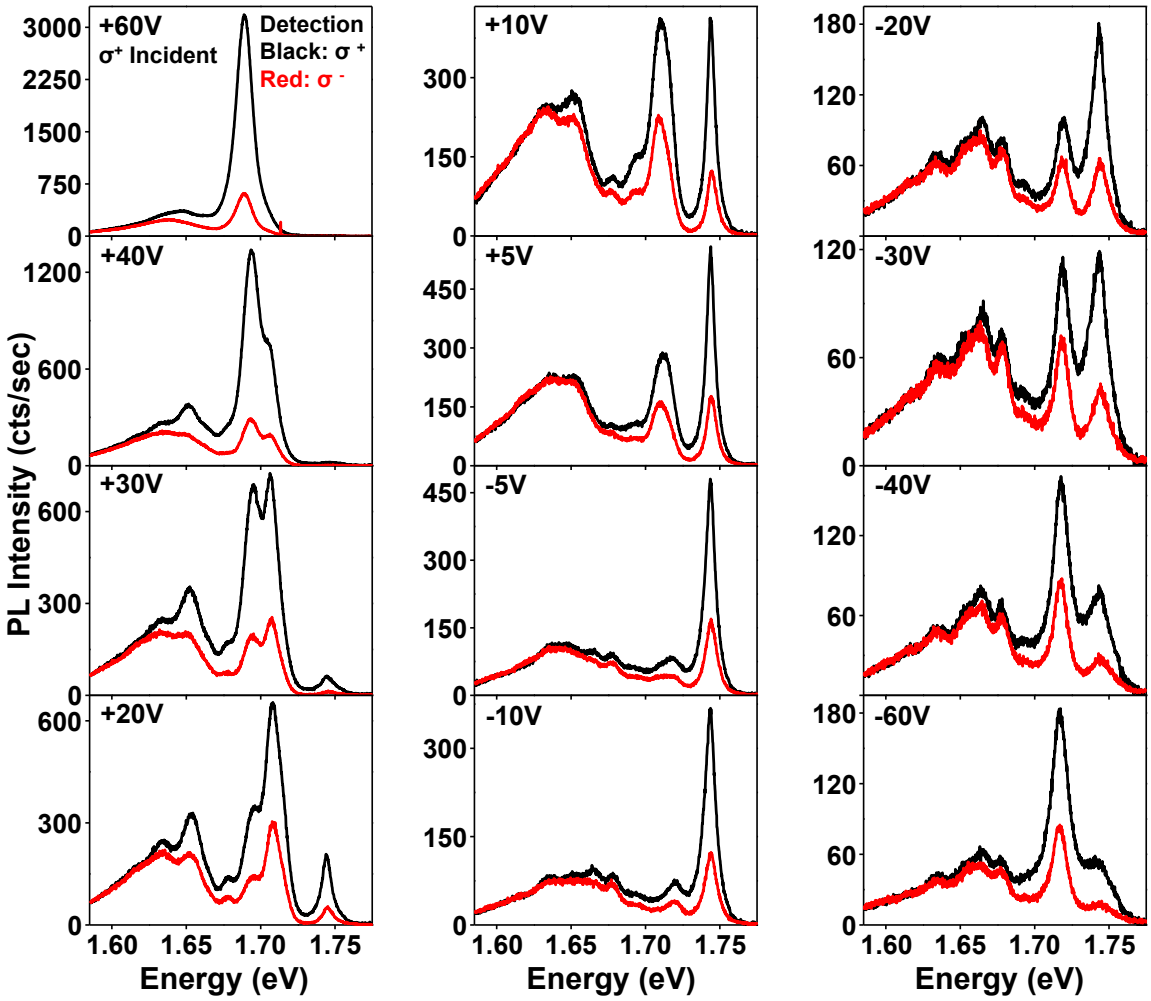

Figure A.1: Polarization-resolved PL spectra of monolayer WSe_2 at indicated gate voltages for σ^+excitation and σ^+(black) and σ^-(red) polarized detection.

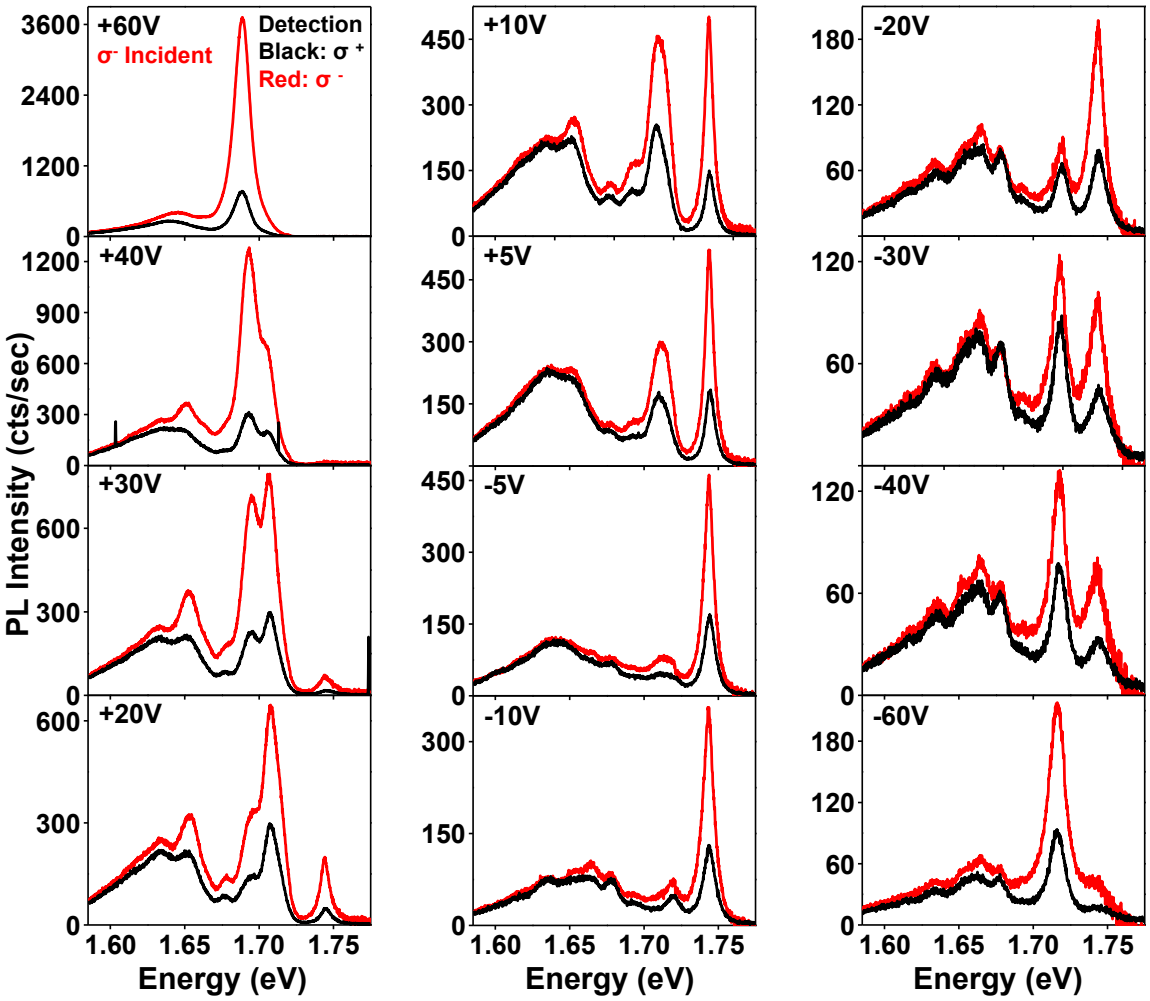

Figure A.2: Polarization-resolved PL spectra of monolayer WSe_2 at indicated gate voltages for σ^- excitation and σ^+(black) and σ^-(red) polarized detection.

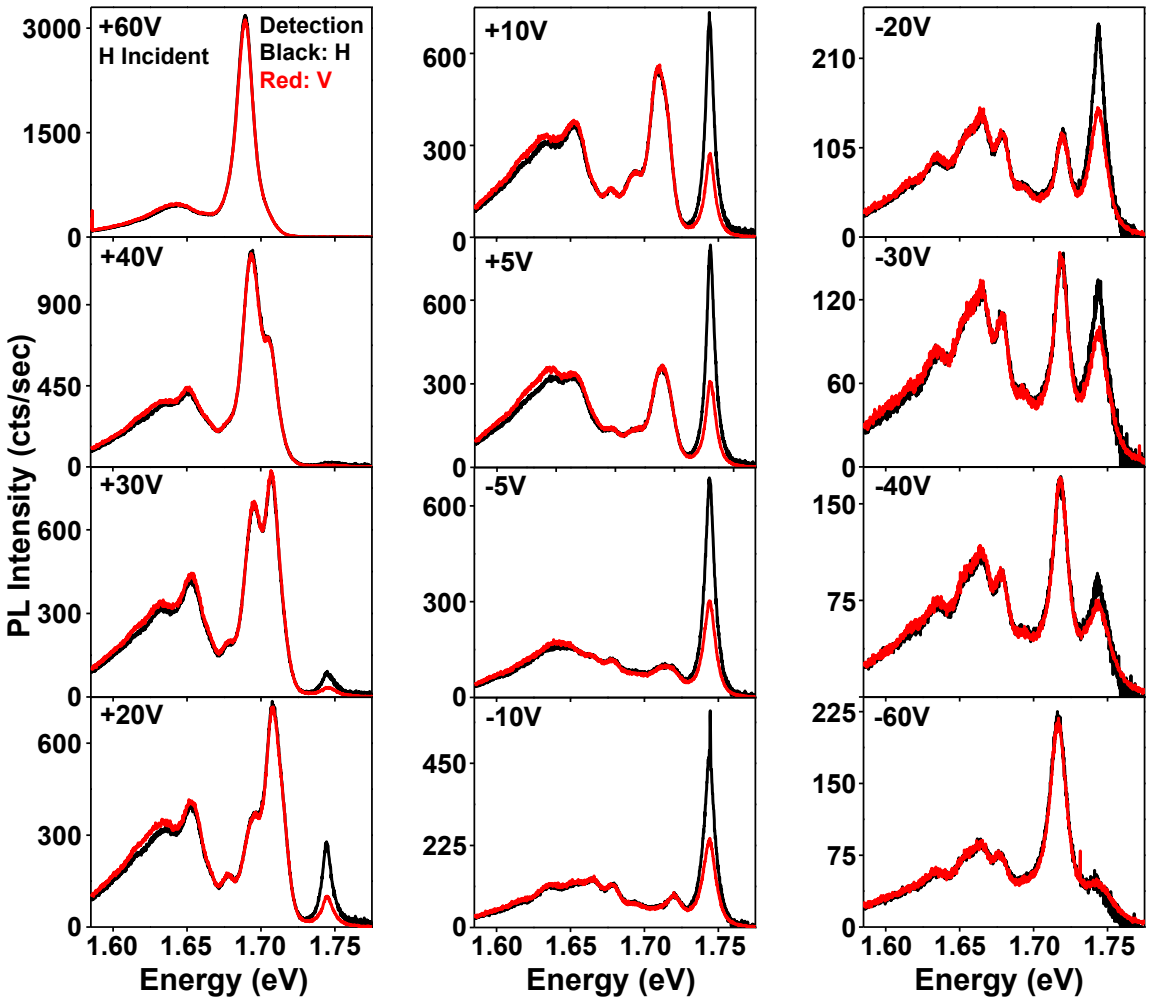

Figure A.3: Polarization-resolved PL spectra of monolayer WSe_2 at indicated gate voltages for horizontally polarized excitation and horizontally (black) and vertically (red) polarized detection.

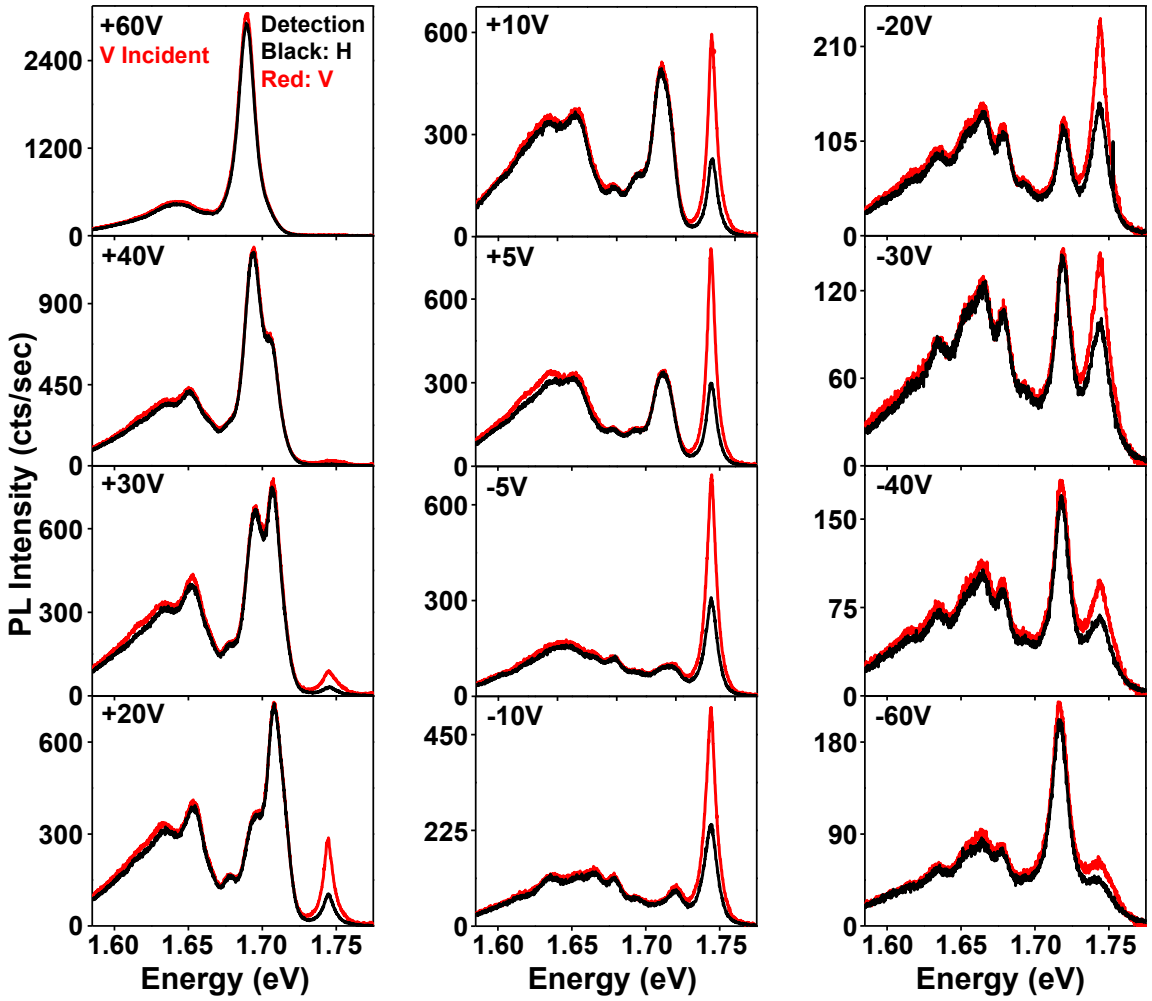

Figure A.4: Polarization-resolved PL spectra of monolayer WSe_2 at indicated gate voltages for vertically polarized excitation and horizontally (black) and vertically (red) polarized detection.

VITA

Aaron Mitchell Jones was born to Alan and Melanie Jones in Provo, Utah. He attended Brigham Young University there for his undergraduate education, where he was afforded the opportunity to build optical systems and investigate the physics of quantum dots within the lab of Dr. John Colton. He was also simultaneously involved in the neutron detector prototyping work of Dr. Lawrence Rees' lab, in collaboration with his grandfather Dr. J. Bart Czirr. Following his graduation with a Bachelor of Science in Physics with a Mathematics minor, he spent the summer in Livermore, CA as a Research Intern to Dr. Roger Minich at Lawrence Livermore National Laboratory. It was during this summer that he first spoke with Dr. Xiaodong Xu and gained interest in optical studies of low-dimensional materials. Fortunately, he decided to immediately join Dr. Xu's lab as a graduate student at the University of Washington, and hasn't looked back since.